LeMMINGs IV: The X-ray properties of a statistically-complete sample of the nuclei in active and inactive galaxies from the Palomar sample

D. R. A. Williams[1,2,3★], M. Pahari[4,3], R. D. Baldi[5,3], I. M. McHardy[3], S. Mathur[6,7,8], R. J. Beswick[1], A. Beri[9,3], P. Boorman[10], S. Aalto[11], A. Alberdi[12], M. K. Argo[13], B. T. Dullo[14], D. M. Fenech[15], D. A. Green[15], J. H. Knapen[16,17], I. Martí-Vidal[18,19], J. Moldon[12,1], C. G. Mundell[20], T. W. B. Muxlow[1], F. Panessa[21], M. Pérez-Torres[12], P. Saikia[22], F. Shankar[3], I. R. Stevens[23], P. Uttley[24]

[1] *Jodrell Bank Centre for Astrophysics, School of Physics and Astronomy, The University of Manchester, Manchester, M13 9PL, UK*
[2] *Department of Physics, University of Oxford, Denys Wilkinson Building, Keble Road, Oxford, OX1 3RH, UK*
[3] *School of Physics and Astronomy, University of Southampton, Southampton, SO17 1BJ, UK*
[4] *Department of Physics, Indian Institute of Technology, Hyderabad 502285, India*
[5] *INAF - Istituto di Radioastronomia, Via P. Gobetti 101, I-40129 Bologna, Italy*
[6] *Astronomy department, The Ohio State University, Columbus, OH, 43210, USA*
[7] *Center for Astronomy and Astro-particle Physics, The Ohio State University, Columbus, OH 43210, USA.*
[8] *Eureka Scientific, 2452 DELMER ST STE 100, Oakland, CA, 94602, USA*
[9] *DST-INSPIRE Faculty, Indian Institute of Science Education and Research (IISER), Mohali, Punjab, 140306, India*
[10] *Astronomical Institute, Academy of Sciences, Boční' II 1401, CZ-14131 Prague, Czech Republic*
[11] *Department of Space, Earth and Environment, Chalmers University of Technology, Onsala Observatory, SE-439 92 Onsala, Sweden*
[12] *Instituto de Astrofísica de Andalucía (IAA-CSIC), Glorieta de la Astronomía s/n, 18008 Granada, Spain*
[13] *Jeremiah Horrocks Institute, University of Central Lancashire, Preston PR1 2HE, UK*
[14] *Departamento de Física de la Tierra y Astrofísica, IPARCOS, Universidad Complutense de Madrid, E-28040 Madrid, Spain*
[15] *Astrophysics Group, Cavendish Laboratory, 19 J. J. Thomson Avenue, Cambridge CB3 0HE, UK*
[16] *Instituto de Astrofísica de Canarias, Vía Láctea S/N, E-38205 La Laguna, Spain*
[17] *Departamento de Astrofísica, Universidad de La Laguna, E-38206 La Laguna, Spain*
[18] *Observatori Astronómic, Universitat de València, Parc Científic, Paterna, València, Spain*
[19] *Departament d'Astronomia i Astrofísica, Universitat de València, Burjassot, València, Spain*
[20] *Department of Physics, University of Bath, Claverton Down, Bath, BA2 7AY, UK*
[21] *INAF - Istituto di Astrofisica e Planetologia Spaziali, via Fosso del Cavaliere 100, I-00133 Roma, Italy*
[22] *Center for Astro, Particle and Planetary Physics (CAP^3), New York University Abu Dhabi, PO Box 129188, Abu Dhabi, UAE*
[23] *School of Physics and Astronomy, University of Birmingham, Edgbaston, Birmingham B15 2TT, UK*
[24] *Anton Pannekoek Institute for Astronomy (API), University of Amsterdam, Science Park 904, 1098 XH Amsterdam, the Netherlands*

Accepted XXX. Received YYY; in original form ZZZ

ABSTRACT

All 280 of the statistically-complete Palomar sample of nearby (<120 Mpc) galaxies δ >20° have been observed at 1.5 GHz as part of the LeMMINGs *e*-MERLIN legacy survey. Here, we present *Chandra* X-ray observations of the nuclei of 213 of these galaxies, including a statistically-complete sub-set of 113 galaxies in the declination range 40° < δ < 65°. We observed galaxies of all optical spectral types, including 'active' galaxies (e.g., LINERs and Seyferts) and 'inactive' galaxies like H II galaxies and absorption line galaxies (ALG). The X-ray flux limit of our survey is $1.65{\times}10^{-14}$ erg s^{-1} cm^{-2} (0.3−10 keV). We detect X-ray emission coincident within 2-arcsec of the nucleus in 150/213 galaxies, including 13/14 Seyferts, 68/77 LINERs, 13/22 ALGs and 56/100 H II galaxies, but cannot completely rule out contamination from non-AGN processes in sources with nuclear luminosities $\lesssim 10^{39}$ erg s^{-1}. We construct an X-ray Luminosity function (XLF) and find that the local galaxy XLF, when including all AGN types, can be represented as a single power-law of slope -0.54 ± 0.06. The Eddington ratio of the Seyferts is usually 2−4 decades higher than that of the LINERs, ALGs and H II galaxies, which are mostly detected with Eddington ratios $\lesssim 10^{-3}$. Using [O III] line measurements and BH masses from the literature, we show that LINERs, H II galaxies and ALGs follow similar correlations to low luminosities, suggesting that some 'inactive' galaxies may harbour AGN.

Key words: X-rays: galaxies – galaxies: active

★ E-mail: david.williams-7@manchester.ac.uk

1 INTRODUCTION

In the nuclear regions of nearby galaxies, optical emission line ratio diagrams (called BPT diagrams) are commonly used to discriminate star formation (SF) from accretion onto super-massive black holes (SMBHs), known as active galactic nuclei (AGN, e.g., Baldwin et al. 1981; Kewley et al. 2006; Buttiglione et al. 2010). At the lowest luminosities, optical emission lines can be too weak to provide a reliable interpretation of the nuclear activity. This issue is most prevalent in low-luminosity AGN (LLAGN), defined by Hα luminosity, L_{H_α} < 10^{40} erg s^{-1} (Ho et al. 1997a) or by their X-ray luminosities $L_{\mathrm{X-ray}}$ < 10^{42} erg s^{-1} (Ptak 2001). These definitions commonly encompass nearby AGN such as Seyferts (Seyfert 1941) and Low-Ionisation Nuclear Emission Line regions (LINERs, first defined in Heckman 1980), which are likely powered by a central AGN engine. Other galaxies, such as the nuclei in star forming galaxies known as H ii galaxies and absorption line galaxies (ALGs) do not have strong enough emission lines to be unequivocally powered by an AGN, but may include a weak or dormant SMBH, in which case they may harbour a LLAGN.

The study of LLAGN is important for several reasons. They represent the most numerous type of AGN in the Universe (Ptak 2001; Nagao et al. 2002; Filho et al. 2006) and their low luminosities are thought to be caused by a combination of low accretion rates (Kauffmann & Heckman 2009) and low radiative efficiency of inefficient accretion processes (Ho 1999b; Maoz 2007; Panessa et al. 2007; Ho 2008). LLAGN are often associated with SMBHs of lower masses (< 10^7 $M_\odot$) and represent the most common accretion state in SMBHs (Ho 2008). Therefore, LLAGN provide the best opportunity to understand the bulk of the population of AGN, which is important for cosmological models of SMBH evolution, the physics and efficiency of accretion at the lowest luminosities, the triggering mechanisms of accretion and the local SMBH luminosity functions.

In order to detect the presence of a LLAGN in a nearby galaxy when optical emission lines are weak or not present, multi-wavelength data must be used instead. AGN are often detected at cm wavelengths because dust in the interstellar medium is transparent, allowing for unobscured views of the nuclei of nearby galaxies. However the radio luminosity from LLAGN is often very low (10^{-4} of the bolometric output; Condon 1992) and can be contaminated by SF. Thus to distinguish AGN we require both high sensitivity and high angular resolution. We have therefore observed all 280 galaxies above declination, δ > +20° from the Palomar bright spectroscopic sample of nearby galaxies (Filippenko & Sargent 1985; Ho et al. 1995, 1997a,b,c,d, 2003, 2009, hereafter referred to as the 'Palomar sample') with the *e*-MERLIN radio interferometer array as part of the **L**egacy **e**-**M**ERLIN **M**ulti-band **I**maging of **N**earby **G**alaxies **S**urvey (LeMMINGs; Beswick et al. 2014; Baldi et al. 2018, 2021a,b) programme. The Palomar sample is generally accepted to be the most statistically complete sample of nearby galaxies. LeMMINGs provides sub-mJy sensitivity with resolution of 0.15″ at 1.5 GHz (Baldi et al. 2018, 2021a,b) and 0.05″ at 5 GHz (analysis still is still ongoing and will be presented in future papers).

Radio observations on their own cannot always distinguish the AGN and additional observations in other wavebands are required. The X-ray waveband is particularly valuable: compact X-ray emission with a steep powerlaw spectrum (photon index, Γ=1.3−2.1, where $\mathrm{n(E)dE} \propto \mathrm{E}^{-\Gamma}$) is commonly interpreted as a 'smoking gun' for an AGN (Nandra & Pounds 1994; Piconcelli et al. 2005; Ishibashi & Courvoisier 2010). However, X-ray emission in the centres of galaxies can be contaminated by X-ray binaries (XRBs) and Ultra-luminous X-ray sources (ULXs) below X-ray luminosities of 10^{39} erg s^{-1}. Previous *ROSAT* X-ray observations have insufficient angular resolution to remove the contribution of these sources (Roberts & Warwick 2000), necessitating the sub-arcsecond resolution X-ray imaging only possible with the *Chandra* X-ray observatory (hereafter *Chandra*, Weisskopf et al. 2000). The combination of sub-arcsecond angular resolution and high sensitivity provided by *Chandra* allows for the detection of faint nuclei down to X-ray luminosities of 10^{39-42} erg s^{-1} (Fabbiano 2006).

X-ray studies of nearby LLAGN have focussed on the known 'active' galaxies like Seyferts and LINERs (Ho 1999a; Ho et al. 2001; Panessa et al. 2006; González-Martín et al. 2006; Akylas & Georgantopoulos 2009; Hernández-García et al. 2014; González-Martín et al. 2015), often returning detection fractions of X-ray nuclei $\gtrsim$ 60 per cent. However, these studies have often missed the H ii and ALG galaxies which may also harbour an AGN. Other studies have prioritised larger samples in which these 'inactive' sources may be selected, but the inhomogeneous nature of these samples makes statistical comparisons between different types of source difficult: Zhang et al. (2009) used *Chandra*, *XMM-Newton* and *ROSAT* to study 187 objects within a distance of 15 Mpc but employ their own multi-wavelength criteria; Liu (2011) analysed 383 objects from the entire *Chandra* archive which is biased to the well-known AGN and interesting off-nuclear sources such as ULXs; She et al. (2017) made a volume limited (d<50 Mpc) *Chandra* sample, finding a detection fraction of 44 per cent for all galaxies, including the 'inactive' sources, but the sample was limited by the number of observations in the *Chandra* archive. In an effort to overcome these issues and compile a statistically-complete sample of LLAGN, we have constructed a catalogue of nuclear X-ray emission in nearby galaxies selected from the Palomar survey covered by LeMMINGs data, compiling all available data in the *Chandra* archive. We obtained 48 new observations of nearby galaxies to complete the sample in a declination range. Our catalogue has sub-arcsecond imaging in the X-ray band and is unbiased towards 'inactive' galaxies due to the parent sample selection.

This paper is structured as follows: in Section 2, we describe the observations and data reduction, in Section 3 we show the Chandra X-ray data results and present the sources detected. In Section 4, we discuss the results and implications of X-ray emission in the nearby Universe. Finally, in Section 5 we summarise our results and present our conclusions.

2 SAMPLE SELECTION AND *CHANDRA* OBSERVATIONS

To build a statistically-complete sample of nearby LLAGN, we started with the Palomar sample (Filippenko & Sargent 1985; Ho et al. 1995, 1997a,b,c,d, 2003, 2009). The Palomar sample is statistically-complete to a brightness limit of B_T < 12.5mag. We selected sources with δ > 20°, to ensure that the synthesized beams in the radio observations were not highly elliptical, which is important for detecting small scale (sub-arcsecond, sub-kpc) jets. These 280 galaxies represent the LeMMINGs radio survey of nearby galaxies (Beswick et al. 2014; Baldi et al. 2018, 2021a,b). The goal of LeMMINGs is to probe accretion and star formation in nearby galaxies in the radio waveband at 1.5 and 5 GHz with resolutions of up to 150 mas and 50 mas respectively, in concert with ancillary multi-wavelength data. Thus far, all 280 of the LeMMINGs objects have been observed by *e*-MERLIN at 1.5 GHz (see Baldi et al. 2018, 2021a,b). Observations at 5 GHz have been completed and the data are being analysed (Williams et al., in prep.). To diagnose the central engine, all of the objects in the LeMMINGs survey were re-classified

Galaxy Name (1)	Right Asc. (2)	Dec. δ (3)	Gal. Lat. $\|b\|$ (4)	Dist (Mpc) (5)	Obs. ID. (6)	Exposure (secs) (7)	Sample Status (8)	Det. Sig. (9)	Mass log($M_\odot$) (10)	$O_{[III]}$ log(Lum.) (11)	AGN Class (12)	Hubble Type (13)
NGC7817	0.995	20.752	−40.76	31.5	-	-	-	Not obs.	6.21 ± 0.22	39.29	HII	Spi.
IC10	5.096	59.293	3.34	1.3	8458	43571	-	Undet	5.11 ± 0.82	37.13	HII	Irr.
NGC147	8.299	48.507	−14.25	0.7	-	-	-	Not obs.	4.28 ± 0.40	-	ALG	Ell.
NGC185	9.739	48.337	−14.48	0.7	-	-	-	Not obs.	4.10 ± 0.21	34.63	LINER	Ell.
NGC205	10.092	41.683	−21.14	0.7	4691	9870	C	Undet	3.83 ± 1.84	-	ALG	Ell.
NGC221	10.674	40.866	−21.98	0.7	5690	113027	C	Undet	6.39 ± 0.19	-	ALG	Ell.
NGC224	10.685	41.269	−21.57	0.7	14196	42848	C	146.78	7.84 ± 0.05	-	ALG	Spi.
NGC266	12.449	32.278	−30.59	62.4	16013	84950	-	204.06	8.37 ± 0.07	39.43	LINER	Spi.
NGC278	13.018	47.550	−15.32	11.8	2055	38259	-	11.87	5.62 ± 0.33	37.47	HII	Spi.
NGC315	14.454	30.352	−32.50	65.8	4156	55016	-	33.96	8.92 ± 0.31	39.44	LINER	Ell.

Table 1. First 10 rows of the table of basic properties of the X-ray sample presented in this paper. The full table can be found in the online supplementary material. We show (1) the galaxy name; (2) Right Ascension in decimal degrees; (3) Declination in decimal degrees; (4) the Galactic Latitude (δ); (5) the distance in Mpc, which is obtained from (Ho et al. 1997a, and references therein); (6) the *Chandra* observation ID used for this analysis; (7) the exposure length in seconds; (8) denoted 'C' if part of the 'Complete' sample described in Section 2, denoted 'Y' if this is a new *Chandra* observation obtained in observing cycle 17 (programme ID 19708646 and 18620515, PI:McHardy), or denoted 'C+Y' if part of the 'Complete' sample and a new *Chandra* observation; (9) the detection significance where a source is observed or detected, 'Undet.' if the source is not detected in the observations or 'Not obs.' if there is no data in the *Chandra* archive; (10) a black hole mass measurement taken from the literature where possible (e.g., van den Bosch 2016), but where no dynamical measurements exist, we use the $M-\sigma$ relationship of Tremaine et al. (2002), using the stellar velocity dispersions of (Ho et al. 1997a); (11) a measurement of the [O III] line luminosity from (Baldi et al. 2018) or Baldi et al. (2021a), taken from the literature or (Ho et al. 1997a) in erg s^{-1}; (12) the new AGN classification given to the source based on the AGN re-classifcation scheme described in Baldi et al. (2018) and Baldi et al. (2021a); (13) a simplified version of the Hubble types originally shown in Ho et al. (1997a).

using their optical spectra from the Palomar sample into the Seyfert, LINER, ALG or H II galaxy classifications according to updated diagnostic diagrams (Kewley et al. 2006; Buttiglione et al. 2010). The re-classification scheme can be found in Baldi et al. (2018, 2021a), but for convenience, we list these classifications in Table 8.

Of the 280 Palomar galaxies above $\delta = 20°$, 125/280 had been observed by *Chandra* observing programmes as of June 2015 and the data were publicly available[1]. An additional 48 objects were observed as part of *Chandra* observing cycle 17 (programme ID 19708646 and 18620515, PI: McHardy), to provide complete *Chandra* coverage of all Palomar galaxies, selected in the declination range 40−65° and Galactic latitude $|b| > 20°$. By selecting in this range, we ensured that the sample was not biased towards known 'active' galaxies (e.g., LINERs and Seyferts) and avoided significant extinction from the Milky Way. We observed any previously unobserved sources for 10 ks, sufficient for detecting a source at an X-ray luminosity of 10^{39} erg s^{-1} at the median distance of the LeMMINGs sample (~20 Mpc), with a Hydrogen absorbing column (N_H) of up to 10^{23} cm^{-2}. The additional 48 objects included some objects with existing short *Chandra* observations, to increase the combined exposure on each of these galaxies to 10 ks. Unfortunately, one object, NGC 2685, was missed from the original observing list, but other than this object, the LeMMINGs and Palomar surveys are now complete for the declination range 40−65° and galactic latitude cut.

Additional observations of the Palomar objects in our sample have been observed as part of other *Chandra* programmes, and these have also been included in our final sample. Therefore, we analyse all publicly available *Chandra* X-ray data up to June 2018, and now *Chandra* X-ray data exist for 213/280 objects (~76 per cent) in the LeMMINGs sample. For sources with multiple observations, we choose those with the longest exposure in order to improve the chance of source detection or for improved signal-to-noise for spectral modelling. In addition, we do not use any grating observations, choosing only ACIS-S and ACIS-I observations. A future manuscript (LeMMINGs VI, Pahari et al. in prep) will analyse all publicly available ACIS datasets for the purposes of finding all X-ray sources in the LeMMINGs fields and perform variability analyses. The 213 galaxies observed by *Chandra* constitute the 'X-ray LeMMINGs sample', which we hereafter refer to as the 'entire' sample. We plot this sample as a function of distance in the *top* panel of Figure 1. Furthermore, the 113 objects in the 40−65° declination range are referred to as the 'Complete' sample (*bottom* panel of Figure 1). We performed a Kolmogorov−Smirnov (KS) test on the distance distributions between the two samples and could not conclude that the two samples were statistically different. Future *Chandra* proposals will be submitted with the goal of observing all 280 galaxies with at least 10 ks exposure times, to complete the entire sample.

A large number of the observed LeMMINGs objects in the *Chandra* archive are known 'active' galaxies based on their optical diagnostic emission-line 'BPT' classifications (Baldwin et al. 1981; Kewley et al. 2006; Buttiglione et al. 2010). However, with the addition of the new observations in the 'Complete' sample, we are able to ameliorate the imbalance of observations by AGN type. Most of the objects in the newly obtained data have never been observed with *Chandra* before and over half are H II galaxies (29/48), which greatly helps the statistical completeness of the entire sample. Now, 100/141 HII galaxies (71 per cent), 22/28 ALGs (79 per cent), 14/18 Seyferts (78 per cent) and 77/93 LINERs (83 per cent), have been observed with *Chandra* for our sample, which is now more consistent with the parent sample split. Out of the 213 objects observed with *Chandra* by June 2018, the numbers are now more equitable: 100 H IIs, 22 ALGs, 14 Seyferts and 77 LINERs, comparing to the original ratio of 70 H II:22 ALG:14 Seyfert:59 LINER. When comparing to the overall fraction of AGN in the LEMMINGs radio sample (48 per cent H II galaxies, 33 per cent LINERs, 12 per cent ALGs, 7 per cent Seyferts), the entire X-ray sample corresponds to 47 per cent H II galaxies, 36 per cent LINERs, 10 per cent ALGs and 7 per cent Seyferts, which are very similar. Therefore, the entire X-ray sample currently represents one of the most complete and unbiased surveys of high-resolution X-ray emission from nearby galaxies.

[1] Data were obtained from the HEASarc website: https://heasarc.gsfc.nasa.gov/db-perl/W3Browse/w3browse.pl

Galaxy Name	Detection Signif.	log Flux 0.3−10 keV erg s^{-1} cm^{-2}	log Flux 0.3−2 keV erg s^{-1} cm^{-2}	log Flux 2−10 keV erg s^{-1} cm^{-2}	log Lum. 0.3−10 keV erg s^{-1}	log Lum. 0.3−2 keV erg s^{-1}	log Lum. 2−10 keV erg s^{-1}
(1)	(2)	(3)	(4)	(5)	(6)	(7)	(8)
IC10	<	−13.92	-	-	36.38	-	-
NGC205	<	−14.00	-	-	35.77	-	-
NGC221	<	−14.24	-	-	35.53	-	-
NGC224	146.78	−12.59 ± 0.05	−12.77 ± 0.10	−13.04 ± 0.10	37.18 ± 0.05	37.00 ± 0.10	36.73 ± 0.10
NGC266	204.06	−12.81 ± 0.06	−13.28 ± 0.10	−12.99 ± 0.10	40.86 ± 0.06	40.39 ± 0.10	40.68 ± 0.10
NGC278	11.87	−14.18 ± 0.10	−14.29 ± 0.11	−14.80 ± 0.20	38.05 ± 0.10	37.93 ± 0.11	37.42 ± 0.20
NGC315	33.96	−11.86 ± 0.03	−12.58 ± 0.04	−11.95 ± 0.04	41.86 ± 0.03	41.13 ± 0.04	41.77 ± 0.04
NGC404	89.63	−13.53 ± 0.07	−13.71 ± 0.16	−14.00 ± 0.16	37.31 ± 0.07	37.13 ± 0.16	36.84 ± 0.16
NGC410	26.74	−12.21 ± 0.06	−12.35 ± 0.03	−12.77 ± 0.28	41.57 ± 0.06	41.43 ± 0.03	41.00 ± 0.28
NGC507	58.35	−12.95 ± 0.02	−12.98 ± 0.02	−14.08 ± 0.02	40.76 ± 0.02	40.73 ± 0.02	39.63 ± 0.02

Table 2. First 10 rows of the table showing flux and luminosity measurements obtained from X-ray spectral fitting (see Section 3 for the sources that have been observed in the *Chandra* archive. The full table can be found in the online supplementary material. All fluxes in this table are calculated using the CFLUX command in XSpec. In the table we show (1) the galaxy name; (2) the detection significance if detected, else a "<" denotes a non detected source where the flux and luminosity measurements given in the 0.3−10 keV band are 3σ upper limits; (3) The logarithm of the flux in the 0.3−10.0 keV band, if detected. If undetected then the model-independent flux upper limit is given from the SRCFLUX tools (see text); (4) The logarithm of the flux in the 0.3−2.0 keV band; (5) The logarithm of the flux in the 2.0−10.0 keV band; (6) The logarithm of the X-ray luminosity in the 0.3−10.0 keV band, if detected. If undetected then the model-independent flux upper limit from the SRCFLUX tools is used to calculate a luminosity upper limit; (7) The logarithm of the X-ray luminosity in the 0.3−2.0 keV band; (8) The logarithm of the X-ray luminosity in the 2.0−10.0 keV band. All uncertainties are shown at the 1 σ level. All fluxes are measured in erg s^{-1} cm^{-2} and all luminosities are measured in erg s^{-1}.

3 *CHANDRA* DATA REDUCTION

We performed standard reduction procedures using the *Chandra* Interactive Analysis of Observations (CIAO 4.11)[2] software to reduce the ACIS data using the updated calibration database (CALDB 4.8.2) in CIAO. For the purpose of core detection significance, we used the `wavdetect` tool in CIAO, which is based on a wavelet transform algorithm and used frequently for point source detection with *Chandra* observations (e.g. Freeman et al. 2002; Liu 2011). This tool is able to resolve sources which are closely separated on the scale of the point spread function (PSF) and able to distinguish diffuse emission due to its advanced treatment of the background. The average background level was equivalent to 1.65×10^{-14} erg cm^{-2} s^{-1}. We extracted flux images and ran the `wavdetect` task on each on-axis chip with scales of 1, 2, 4, 8 and 16 arcsec in the 0.3−10 keV band. We also performed manual examination of each source reported by `wavdetect` for possible false detections.

For the sources detected by `wavdetect`, with the observed flux higher than 5× the background level, circular regions of radius 2 arcsec around the *Hubble* Space Telescope optical centre of the galaxy were used to extract the flux and spectra of the objects. *Hubble* data exist for 173/280 LeMMINGs objects and will be presented in an upcoming work (LeMMINGs V; Dullo et al., in prep). If *Hubble* data were not available, then the galaxy centroid positions were obtained from the literature or from the NASA/IPAC Extragalactic Database[3]. The background region was selected as an annular region with radii between 2 and 5 arcsec for most of the observations. However, for objects where an additional X-ray source was present within 4 arcsec of the core, we selected a 5 arcsec circular region close to the core but free of X-ray sources for the background. We checked and found that such a change in the background selection does not affect the background count rate significantly. Where pile-up is suspected in the spectra, we use an annulus to remove the highly affected inner region and only use the outer region that was unaffected by pile-up. We then use this data to fit a spectrum and report those values here.

[2] http://cxc.harvard.edu/ciao/
[3] https://ned.ipac.caltech.edu/

We checked the fits with a pile-up model in the spectra and do not find significant differences in the reported fluxes between the two methods. Source and background spectra were extracted using the source and background regions using the `specextract` tool in CIAO. Auxiliary Response Files (ARFs) and Redistribution Matrix Files (RMFs) were computed using observation specific aspect solution, mask and bad pixel files; dead area corrections were applied and ARFs were corrected to account for X-rays falling outside the finite size and the shape of the aperture.

For faint sources with an observed flux between 3−5 times the background flux level, a circular region of 10 arcsec was chosen to extract the source spectrum while an annulus region with radii of 10 and 20 arcsec, centered on the source was chosen to extract the background spectrum. Such a choice is made to ensure that both regions contain enough counts to extract observation specific ARFs for the source as well as the background. We checked to see if the difference in annulus size made a significant change in the extracted flux values, but it did not. However, we were careful to choose such regions so that they contain no additional X-ray sources with count rates more than 5 per cent of the typical background level. NGC 4826 and NGC 5907 were two such examples where bright X-ray sources are present within 10″ radius of the core position and they were avoided by choosing a suitable size of the extraction region.

For sources where there was no X-ray counterpart detected in the central region, the `srcflux` tool was used to provide a model-independent estimate of the net count rates and fluxes including uncertainties in 0.3−10 keV energy band. Due to very low X-ray count rates, 20 arcsec circular source and background regions free of off-nuclear emission were chosen for this estimation. The PSF fractions in the source and background regions are estimated from the model PSF using `arfcorr` tool in the 0.3−10 keV band.

We extracted and fitted the X-ray spectra of all the nuclear sources using version 12.11.1 of the XSPEC software (Arnaud 1996). For bright sources, the extracted background-subtracted spectra are binned so that the signal-to-noise in each spectral bin is 3 or higher. For faint sources, the spectral binning is performed so that each bin contains at least 10 counts. For a few sources which have a detection significance of 4 or less, a binning of 5 counts per spectral bin was used. For spectral fitting of faint sources in XSPEC, the Gehrels weighting method (Gehrels 1986) was used which is suitable for Poisson data. For spectral modelling of faint sources, we used W-statistics, which is C-statistics with the background spectrum provided in XSPEC, while the Anderson Darling statistic (Anderson & Darling 1954; Stephens 1974) was used as the test statistic. While fitting, if some parameters could not be constrained within the acceptable range, they were fixed to the typical values, e.g., the width of the narrow Gaussian Fe emission line was fixed to 0.01 keV in some cases, and if the power-law photon index was not constrained with the range of 0.5 and 6, it was fixed to 1.8 while fitting.

Due to the low count rates in many of the observations, we fit simple models to the data. The base model used was PHABS × ZTBABS× ZPOWERLAW. The Galactic absorption (PHABS) was obtained from Kalberla et al. (2005)[4] and was fixed. The host galaxy absorption (ZTBABS) was allowed to vary, as was the photon index (ZPOWERLAW). For most sources (102/150 detections, 68 per cent), the low count rates prevented more complex models than the simple absorbed power-law described above, and the parameters for these models are presented in Table. 10. However, in many bright sources, we required additional components to fit the more complicated spectra. These additional models included: ZGAUSS for the Iron K alpha fluorescence line at 6.4 keV (present in 8 objects); an additional absorber model, either ZPCFABS or ZXIPCF (required in the models of 30 objects); APEC, a collisionally ionised plasma model (a necessary additional model in 25 objects, note that NGC 4151 required a second APEC model; GABS a Gaussian absorption model (2 objects)). NGC 5194 is a well-studied bright Compton-thick AGN (see e.g., Brightman et al. 2017). Correspondingly, the high-quality *Chandra* spectrum is flat $\gtrsim 3$ keV, and displays a very strong and narrow neutral Fe Kα line: common features of reflection-dominated Compton-thick AGN. To account for these reflection features in the *Chandra* band, we fit a more complex model. In addition to an intrinsic powerlaw approximated with CUTOFFPL, we use PEXRAV to reproduce the reflection spectrum by freezing the RELREFL parameter to -1 (since spectra > 10 keV are needed to constrain this parameter well). We then included a fraction of the intrinsic powerlaw scattered through a lower column than the absorber (the 'warm mirror'; see e.g., Matt et al. 2000). Finally, we included a ZGAUSS component to reproduce the neutral Fe Kα line and APEC to parameterise the ionised gas component visible $\lesssim 3$ keV. Fluxes for all sources were then extracted from the best fit spectra in the 0.3–10.0, 0.3–2.0 and 2.0–10.0 keV bands.

The photon indices, Γ, typically range from ~1.0 to 3.5. Figure 3 shows a histogram of the distribution of photon indices in both the Complete and entire samples presented in this work. Note that we only plot sources where a photon index was constrained (see below) and not an upper limit. In both samples, the peak of this histogram is in the bin of sources between Γ=1.75–2.00. In some faint sources with fluxes between 3-5 σ detection limits in their images the photon index is highly unconstrained. We therefore fixed the photon index to Γ=1.8 for these faint sources and re-fitted the spectra in order to estimate the host galaxy absorption. These additional fits are provided in the Appendix in table 4. We describe the results of all our X-ray spectral fitting in Section 4.6.

[4] An online tool exists at: https://heasarc.gsfc.nasa.gov/cgi$-$bin/Tools/w3nh/w3nh.pl

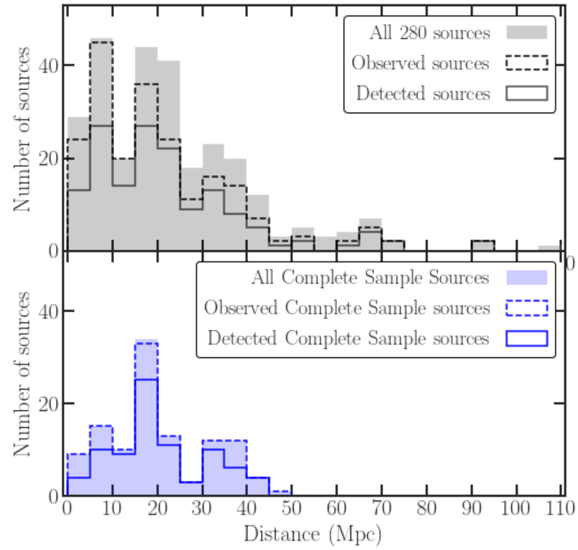

Figure 1. Histogram showing the full number of sources, observed sources and detected sources in the entire (*top* panel) and 'Complete' (*bottom* panel) Palomar X-ray data from *Chandra* as a function of distance. In the *top* panel, the light grey histogram shows all 280 sources, the black dashed line shows the observed (213) sources and the black dot dash line represents the detected sources (150). In the *bottom* panel, the light blue histogram shows all 113 sources in the 'Complete' sample, the blue dashed line shows the observed sources and the blue dot dash line represents the detected sources (82).

.

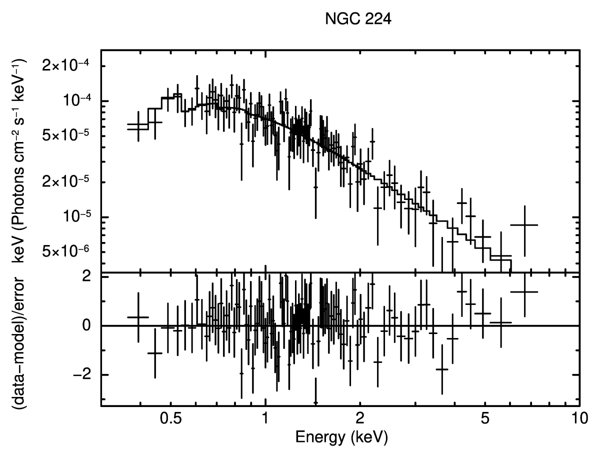

Figure 2. Example X-ray spectrum of one of the X-ray detected sources, NGC224. All other X-ray spectra are shown in the online materials. The *top panel* shows the number of photons cm^{-2} s^{-1} keV^{-1} plotted against the energy in keV across the whole 0.3−10.0 keV band. The *bottom panel* shows the model subtracted from the data, divided by the error. The fit parameters to make these plots are shown in Table 10.

4 RESULTS

Here, we describe the results of the X-ray spectral fitting, fluxes and luminosities, and compare them to the ancillary information, e.g., BH mass, as well as complementary optical data and the LeMMINGs radio data. We compute an X-ray Luminosity Function (XLF) and

Name	Det. Sig.	mod.	cstat/ χ^2	PHABS N_H	ZTBABS N_H	ZPOWERLW Phot.I.	ZPOWERLW norm.	APEC kT	APEC norm.
(1)	(2)	(3)	(4)	(5)	(6)	(7)	(8)	(9)	(10)
IC10	-	α	-	50.6	-	-	-	-	-
NGC205	-	α	-	5.83	-	-	-	-	-
NGC221	-	α	-	18.3	-	-	-	-	-
NGC224	146.78	β	0.87	16.9	<0.04	$2.82^{+0.14}_{-0.13}$	$9.96^{+0.95}_{-0.84}\times10^{-5}$	-	-
NGC266	204.06	β	0.69	5.68	$0.23^{+0.10}_{-0.06}$	$1.91^{+0.14}_{-0.14}$	$3.05^{+0.51}_{-0.17}\times10^{-5}$	-	-
NGC278	11.87	β	10.13/9[c]	12.9	<0.15	$2.25^{+1.22}_{-0.98}$	$2.30^{+1.34}_{-1.08}\times10^{-6}$	-	-
NGC315	33.96	ζ	1.06	5.90	$0.08^{+0.07}_{-0.06}$	$1.49^{+0.06}_{-0.08}$	$1.84^{+0.15}_{-0.32}\times10^{-4}$	$0.54^{+0.02}_{-0.04}$	$2.62^{+0.54}_{-0.61}\times10^{-4}$
NGC404	89.63	γ	15.57/20[c]	5.71	$0.44^{+0.24}_{-0.29}$	$1.88^{+0.25}_{-0.23}$	$4.89^{+1.29}_{-1.02}\times10^{-6}$	$0.24^{+0.07}_{-0.05}$	$5.17^{+16.96}_{-4.06}\times10^{-5}$
NGC410	26.74	γ	0.79	5.11	$0.06^{+0.07}_{-0.06}$	<2.18	$1.95^{+2.11}_{-1.01}\times10^{-5}$	$0.78^{+0.04}_{-0.05}$	$2.07^{+0.41}_{-0.39}\times10^{-4}$
NGC507	58.35	γ	1.02	5.25	$0.07^{+0.07}_{-0.06}$	>2.77	$<3.71\times10^{-6}$	$0.91^{+0.04}_{-0.05}$	$5.89^{+0.77}_{-0.64}\times10^{-5}$

Table 3. First ten rows and ten columns of the basic parameters from the *Chandra* X-ray spectral fits, including those where the source was undetected. In this table, we only report the most basic parameters, e.g., the photon index and some of the neutral absorbers, but the table is continued for the additional parameters in the supplementary material for all observed galaxies. In this table, we show the (1) Galaxy name; (2) detection significance if detected, else a dash is used; (3) the X-ray spectral fit model used (see below for list of spectral models); (4) the reduced χ squared value (number), or where the source is faint and Poissonian statistical treatment is required of the data, the C-statistic divided by the number of degrees of freedom e.g., the cstat parameter reported by XSpec, denoted with a superscript letter 'c' (5) the Galactic absorption e.g., the PHABS parameter, obtained from Kalberla et al. (2005) in unit of 10^{20} cm^{-2}; (6) the additional absorption column density in cm^{-2} found in the ztbabs component, if any, divided by 10^{22}; (7) and (8) the ZPOWERLW model photon index and normalisation respectively. (9) and (10) the APEC energy in kT and association normalisation, respectively. We note that not all spectral components are listed here, but the full list can be found on the online supplementary material. The spectral models used are defined as follows: α : undetected; β : PHABS × ZTBABS × ZPOWERLW; γ : PHABS × ZTBABS(APEC + ZPOWERLW); δ : PHABS × ZTBABS × ZXIPCF × ZPOWERLW; ζ : PHABS × ZXIPCF × ZTBABS(APEC + ZPOWERLW); ω : PHABS × ZXIPCF × ZXIPCF × ZTBABS(APEC + GABS × ZPOWERLW); κ : PHABS × ZTBABS(ZGAUSS + ZPOWERLW); ι : PHABS × ZXIPCF × ZTBABS(ZGAUSS + ZPOWERLW); ϵ : PHABS × ZTBABS × ZPCFABS × ZPOWERLW; η : PHABS × ZXIPCF × ZTBABS(APEC + ZGAUSS + ZPOWERLW); θ : PHABS × ZPCFABS × ZTBABS(ZGAUSS + ZPOWERLW); μ : PHABS × ZXIPCF × ZXIPCF × ZTBABS × ZPOWERLW; π : PHABS × ZPCFABS × ZTBABS(APEC + ZPOWERLW); τ : PHABS(ZTBABS × CABS × CUTOFFPL + PEXRAV + CONST × CUTOFFPL + APEC + ZGAUSS); ρ : PHABS × ZTBABS × ZXIPCF × ZXIPCF × GABS(ZGAUSS + APEC + APEC + ZPOWERLW);

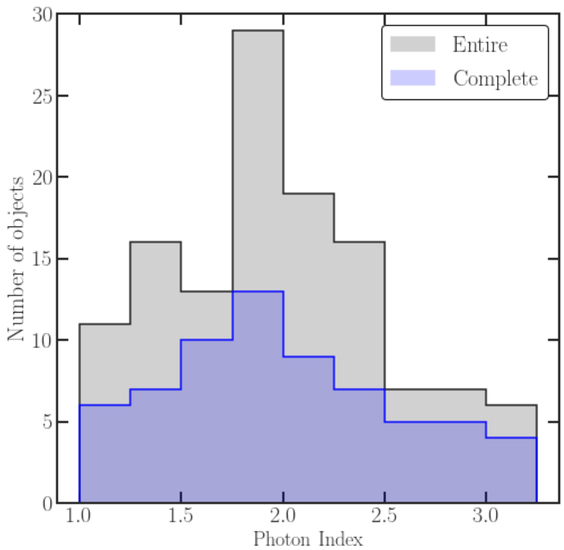

Figure 3. Histogram of the Photon Index from the best fit models of the detected sources in the entire (black) and Complete (blue) X-ray samples, presented here.

Name	ZTBABS N_H	log Lum. 0.3−10 keV
(1)	(2)	(3)
NGC2276	<0.10	39.49
NGC2500	<0.27	38.43
NGC2541	<1.41	38.24
NGC2832	<0.07	41.79
NGC2976	<0.20	36.49
NGC3610	<0.07	39.96
NGC3992	<1.42	38.45
NGC4096	<0.14	38.28
NGC4605	<0.10	36.85
NGC5308	<0.97	39.45
NGC5371	<0.02	40.08
NGC5473	$1.31^{+1.85}_{-1.02}$	39.63
NGC6643	<0.21	39.13

Table 4. Table for sources with 0.3−10 keV X-ray fluxes between 3−5× the image detection significance level, where the photon index was fixed to 1.8 in order to obtain a value for host galaxy absorption with ZTBABS. The errors shown in this table are all at the 1σ level.

compare the X-ray luminosity to the accretion rates in the X-ray LeMMINGs sample.

4.1 Properties of the X-ray sources

Out of the 213 galaxies that have been observed with *Chandra* for our sample, 150 show X-ray emission above a detection threshold of 3σ and are co-incident with the optical core of the galaxy. As the optical positions of these sources are correct to 0.3 arcsec, the FWHM of the Chandra point spread function is 0.5-arcsec and we extracted spectra from a 2-arcsec aperture, they are referred to as 'detected' sources. The other 63 sources are considered 'undetected' yielding a detection fraction of 150/213 (~70 per cent). We plot these detection fractions as a function of the distance of the sources in the *top* panel of Figure 1. For the 'Complete' sample, we arrive at similar detection fractions: 82 detected, 30 non detected, corresponding to a detection fraction ~73 per cent and plot them in the *bottom* panel of Figure 1. For the detected sources, the 0.3−10.0 keV X-ray fluxes range from 5.3×10^{-16} to 5.0×10^{-11} erg cm^{-2} s^{-1}, while the luminosities span from 1.8×10^{36} to 1.6×10^{43} erg s^{-1}. These flux and luminosity ranges are similar to previous studies of nearby galax-

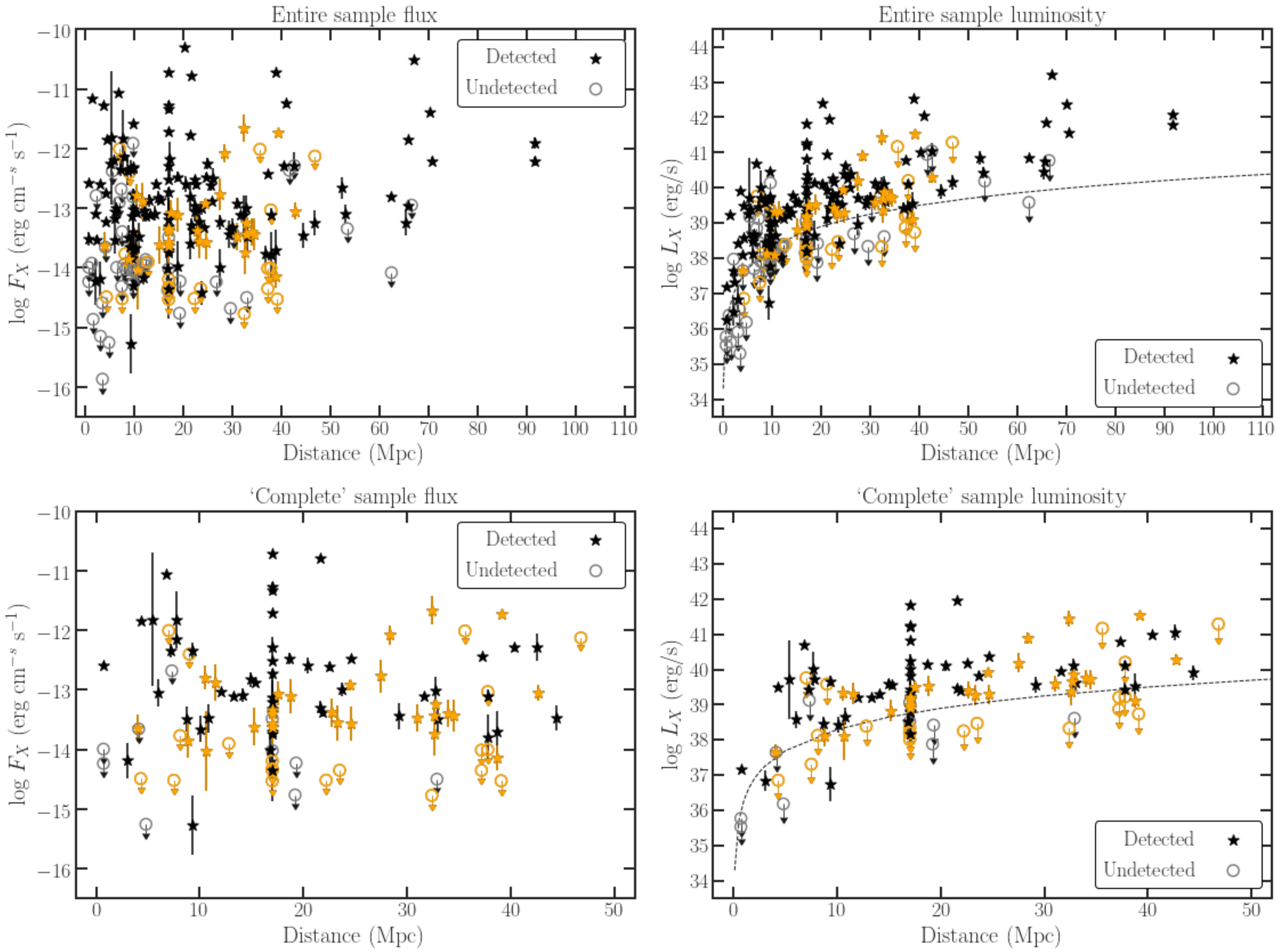

Figure 4. Unabsorbed X-ray flux density (*left* plots) in erg cm^{-2} s^{-1} and luminosity (*right* plots) in erg s^{-1} the 0.3–10 keV band, for the entire sample (*top* row) and 'Complete' sample (*bottom* row), as a function of distance (Mpc). The dashed line corresponds to the limiting flux density of the X-ray sample, corresponding to the average background flux flux level of 1.65×10^{-14} erg cm^{-2} s^{-1}. Some upper limits above this line may be due to short exposure times for some sources. The different symbols correspond to detected sources (stars) and upper limits for undetected sources (open circles). The orange data points represent the 48 new *Chandra* observations obtained in proposals 19708646 and 18620515.

ies made with X-ray observatories (Roberts & Warwick 2000; Liu 2011).

We note that sources with nuclear luminosities $\lesssim 10^{39}$ erg s^{-1} could be ULXs/XRBs near the optical nucleus and not necessarily X-ray emission related to the central supermassive black hole (Fabbiano 2006; Swartz et al. 2011; Kaaret et al. 2017). Of the detected sources in the entire sample, 38 fall below this limit, of which 24 are H II galaxies, 12 are LINERs and 2 are ALGs. In the Complete sample, the number of objects with $L_{X-ray} < 10^{39}$ erg s^{-1} are: 12 H II galaxies, 5 LINERs and 1 ALG. However, one of the benefits of our sample is the overlapping high-resolution radio data from LeMMINGs, which can help disentangle non-AGN sources from real AGN. As accreting SMBHs are more radio-loud than XRBs, the radio data can help distinguish non-AGN activity from true AGN. A future publication (Pahari et al. in prep), will include radio luminosity from LeMMINGs (Baldi et al. 2018, 2021a) as a discriminant for all detected sources in our *Chandra* data, including the nuclear sources. In addition, transient objects in the archive (such as the tidal disruption event, TDE, in NGC 3690) will have large changes in flux over year to decadal time scales. Large changes in X-ray flux over short time periods is unlikely to affect the majority of the sample and the X-ray emission should remain constant over long periods of time. For example, for Seyferts and LINERs, X-ray variability over the course of several years is observed (Hernández-García et al. 2014; Hernández-García et al. 2016). We removed any sources that are known to be transient nuclear events or non-AGN activity at the optical centre of the galaxy. Therefore, three objects - the TDE in NGC 3690 (Mattila et al. 2018), known nuclear ULXs in IC 342 (Liu 2011) and in NGC 3034 (M82) (Muxlow et al. 2010) - are removed from the discussions of the detected sources for the rest of this work.

In the *top* row of Figure 4, we plot the flux and luminosity values obtained for the entire sample as a function of distance, with the new observations for 48 galaxies plotted in orange for comparison. In the *bottom* row of Figure 4, we do the same for the 'Complete' sample. We witness no apparent distance dependence of the sources, with a wide range of fluxes and luminosities observed at all distances. However, there is an exposure length difference as a function of distance, as objects at distances greater than 40 Mpc have a mean exposure of 35 ks, whereas less distant objects have a 30 ks exposure on average. Exposure times will play a role in the likelihood of

Table 5. X-ray detected, undetected and unobserved sources by morphological classification breakdown in the entire X-ray Palomar sample. We note that three sources, NGC 3690, NGC 3034 and IC 342, all Hɪɪ galaxies and noted with the asterisk, are not related to AGN activity, as discussed in Section 4.1.

	optical class				
X-ray	LINER	ALG	Seyfert	Hɪɪ	Tot
detected	68	13	13	56*	150
undetected	9	9	1	44	63
unobserved	16	6	4	41	67
Tot	93	28	18	141	280

Table 6. X-ray detected, undetected and unobserved sources by morphological classification breakdown in the 'Complete' X-ray Palomar sample. We note that one source in the 'Complete' sample, NGC 3690, a Hɪɪ galaxy and noted with the asterisk, is not related to AGN activity, as discussed in Section 4.1.

	optical class				
X-ray	LINER	ALG	Seyfert	Hɪɪ	Tot
detected	34	8	5	35*	82
undetected	4	3	0	23	30
unobserved	1	0	0	0	1
Tot	39	11	5	58	113

detection. It is not possible to quantify the effect this has on the detection likelihood in the sample, however we note that most of the objects in the 'Complete' sample reside closer than 40 Mpc, so this exposure length disparity has less of an effect on the 'Complete' sample.

For the entire X-ray LeMMINGs sample, the median exposure time of detected sources is 20 ks, whereas the median exposure for undetected sources is 10 ks. However, for the 'Complete' sample, the detected sources have a median exposure of 13 ks, and the non-detected sources 10 ks. This again shows that the 'Complete' sample does not suffer much from this potential bias as the entire sample does.

4.2 X-ray luminosity versus optical properties

Table 5 and Table 6 show the number of detected and undetected sources divided by optical class, for the entire and 'Complete' samples, respectively. Seyferts are the most detected optical AGN type (Entire: 13/14, 93 per cent, Complete:5/5, 100 per cent), followed by LINERs (Entire: 68/77, 88 per cent, Complete: 34/38, 89 per cent), then ALGs (Entire: 13/22, 59 per cent, Complete: 8/11, 73 per cent) and with H ɪɪ galaxies being the least detected (Entire: 56/100, 56 per cent, Complete: 35/58, 60 per cent).

In general, Seyferts have been observed with longer exposures, with a mean exposure of 53 ks, compared to 29 ks for LINERs, 32 ks for H ɪɪ galaxies and 25 ks for ALGs. A similar exposure length disparity is observed in the 'Complete' sample. As a consequence, Seyferts have been observed for longer than other galaxies and are therefore more likely to be detected. However, the distribution of X-ray luminosity is similar between Seyferts and LINERs (see Figure 5), but the H ɪɪ galaxies and ALGs have different luminosity distibutions. It is possible that the difference in exposure length could have an affect on the completeness of our sample or the results, but cannot quantify this disparity further.

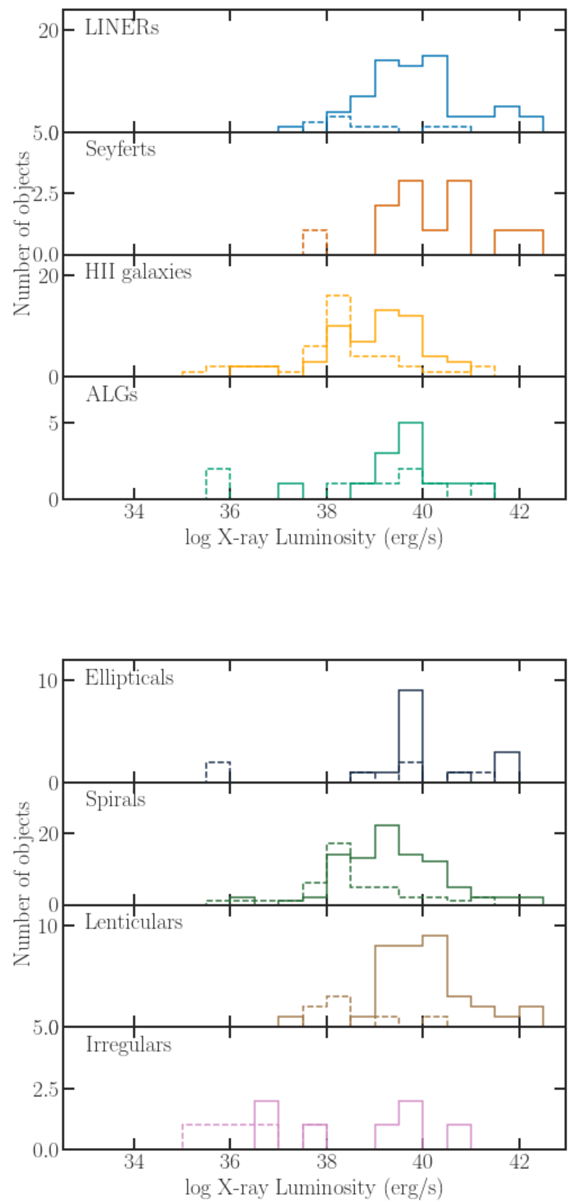

Figure 5. Histograms of the X-ray luminosity (erg s^{-1}) per optical class (top plot) and host morphological type (bottom plot). The solid-line histogram represents the X-ray core luminosity distribution of the detected sources and the dashed line corresponds to the upper limits obtained from the non-detected objects.

4.2.1 *X-ray luminosity distributions vs optical spectroscopic class*

The distribution of X-ray luminosity as a function of AGN optical class is presented in the upper panel of Figure 5. The detected LINERs are the most commonly observed AGN type with a median X-ray luminosity in the 0.3–10.0 keV band of 5.1$\times10^{39}$ erg s^{-1}. The Seyferts occupy a similar region in this plot to the LINERs and have a median luminosity of 4.8$\times10^{40}$ erg s^{-1}. The H ɪɪ galaxies have slightly lower X-ray luminosities, with a broad range between ~10^{36} and 10^{41} erg s^{-1}, with a median luminosity of 2.0$\times10^{39}$ erg s^{-1}. The ALGs have a median luminosity of 3.5$\times10^{39}$ erg s^{-1} but

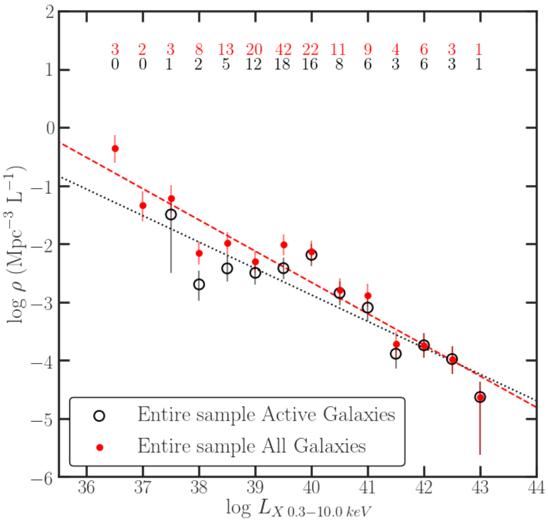

Figure 6. The X-ray luminosity function of the entire X-ray Palomar sample. The red circles show the X-ray detections in the entire sample. The black unfilled circles indicate the 'active' galaxies based on the BPT diagnostic plots in Baldi et al. (2018, 2021a), e.g., the LINERs and Seyferts in the entire sample. The dotted lines are fits to the data, which are in the same colour as the sub-sample used. For the entire sample, the power-law fit yields slope of −0.54±0.06, and for the 'active' galaxies the power-law slope is −0.45±0.05. See Section 4.3 for further details. In addition the number of objects in each bin is written above each bin in the same colour as the sample used. The uncertainties are drawn from a Poisson distribution.

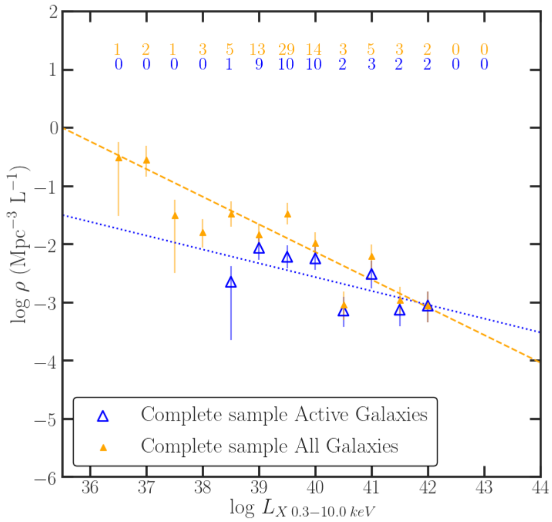

Figure 7. As in Figure 6, showing the X-ray luminosity function of the X-ray 'Complete' sample, a declination restricted sub-sample between 40° to 65°. The orange triangles show the X-ray detections in the 'Complete' sample. The blue unfilled triangles indicate the 'active' galaxies based on the BPT diagnostic plots in Baldi et al. (2018, 2021a), e.g., the LINERs and Seyferts in the 'Complete' sample. For all of the 'Complete' sample, the power-law fit yields slope of −0.48±0.12, and for the 'active' galaxies in the 'Complete' sample, the power-law slope is −0.24±0.11. See Section 4.3 for further details. In addition the number of objects in each bin is written above each bin in the same colour as the sample used. The uncertainties are drawn from a Poisson distribution.

show a similar distribution to H II galaxies at lower luminosities. As for the upper limits (dashed lines in Figure 5), H II galaxies, which have the lowest detection fraction, follow a broader distribution at a luminosities 1−2 decades below the detected sources.

4.2.2 X-ray luminosity distributions vs galaxy morphological class

The lower panel of Figure 5 shows the distribution of X-ray luminosity as a function of galaxy morphological type. We note that this figure shows no overall dependence of X-ray luminosity as a function of the galaxy morphological type, suggesting that nuclear X-ray emission can be found in all Hubble types. The median luminosity values for the sample are as follows: 5.1×10^{39} erg s^{-1} for ellipticals, 9.6×10^{39} erg s^{-1} for lenticulars, 3.3×10^{39} erg s^{-1} for irregulars and 2.5×10^{39} erg s^{-1} for spirals. Approximately two-thirds of the elliptical galaxies are detected (15/22, 68 per cent). They mostly cluster around $\sim10^{40}$ erg s^{-1} with a few more luminous exceptions. The spiral galaxies, which are the most common type in the LeMMINGs sample, have a similar detection rate (93/135, 69 per cent) and follow a broad distribution of X-ray luminosities. The lenticular galaxies show a distribution between $\sim10^{39}$ erg s^{-1} and $\sim10^{41}$ erg s^{-1} and are the most detected Hubble type (37/44, 84 per cent). The irregulars have the lowest detection fraction (7/12, 58 per cent) and are a mixed bag of X-ray luminosities, likely due to the inhomogeneous nature of these galaxies, but they do include a couple of very low luminosity ($\lesssim10^{38}$ erg s^{-1}) detected sources.

4.2.3 Combinations of optical spectroscopic class and galaxy morphological class

We investigated the connection between the different Hubble morphological types and the optical spectroscopic classes. For the detected LINERs, we find that 35/68 are spirals or irregulars, whereas 33/68 are lenticulars or ellipticals, suggesting LINERs can be found in all morphological types of galaxy. Detected Seyferts, by comparison, are detected only in spiral galaxies (9/15) or lenticulars (4/15). The detected H II galaxies are almost exclusively associated with spiral galaxies, 48/56, with 6/56 being irregular galaxies and 2/56 associated with lenticulars. Finally, the ALGs are associated with all galaxy morphological types: 7 lenticulars, 4 ellipticals, 1 spiral and 1 irregular.

Comparing the morphological types to the optical classifications shows that all of the detected ellipticals (15) have LINER (11/15) or ALG (4/11) nuclei. The detected lenticulars are mostly associated with LINERs (22/35) and ALGs (7/35), but also in a 4 Seyferts and 2 H II galaxies. Spiral galaxies are found to mostly to have H II nuclei (48/91) or LINERs (33/91), with 9 Seyferts and 1 ALG. Of the nine detected irregular galaxies, 6 are associated with H II nuclei, 2 with LINERs and 1 with an ALG.

4.3 X-ray luminosity function

We now compute the X-ray luminosity function (XLF), using the V/V_{max} method (Schmidt 1968). The XLF, $\Phi(\log L_X)$, i.e. the space

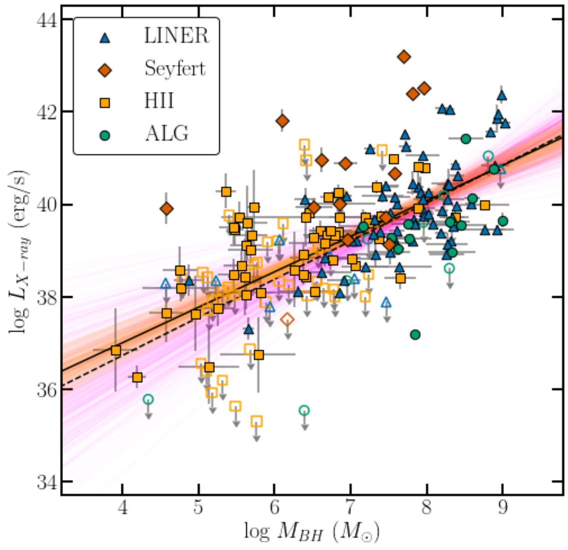

Figure 8. Scatter plot showing the unabsorbed X-ray luminosity (0.3−10.0 keV) as a function of the BH masses for the entire sample, divided per optical class (symbol and color coded as in the legend). The filled symbols refer to the detected X-ray sources, while the empty symbols refer to undetected X-ray sources. The solid line represents the linear correlation found for all galaxies, when taking into account the upper limits using the LINMIX package. The orange lines represent 400 draws from (see text) this fit for all of the galaxies. The dashed line is a fit to all of the sources with a mass $\gtrsim 10^7 M_\odot$ and the purple lines represent 400 draws from these sources.

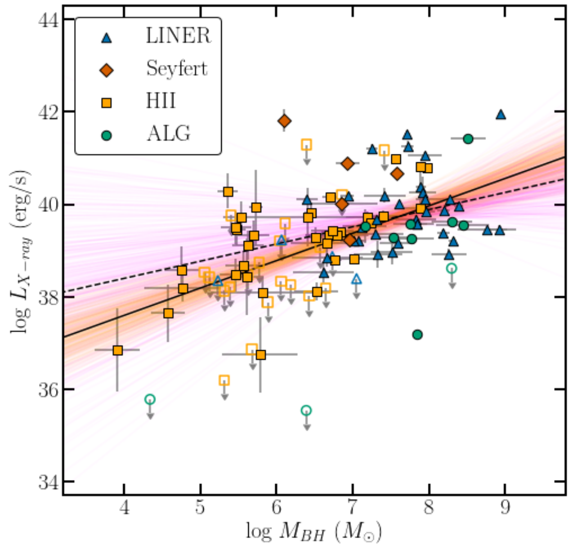

Figure 9. Scatter plot showing the unabsorbed X-ray luminosity (0.3−10.0 keV) as a function of the BH masses for the Complete sample, divided per optical class (symbol and color coded as in the legend). The filled symbols refer to the detected X-ray sources, while the empty symbols refer to undetected X-ray sources. The solid line represents the linear correlation found for all galaxies, when taking into account the upper limits using the LINMIX package. The orange lines represent 400 draws from (see text) this fit for all of the galaxies. The dashed line is a fit to all of the sources with a mass $\gtrsim 10^7 M_\odot$ and the purple lines represent 400 draws from these sources.

density of objects per unit logarithmic interval of luminosity is given by:

$$\Phi\,(\log L_X) = \frac{4\pi}{\sigma} \sum_{i=1}^{n(\log L_*)} \frac{1}{V_{max(i)}}, \tag{1}$$

where $\frac{4\pi}{\sigma}$ is the fraction of the sky surveyed, $n\,(\log L_*)$ is the number of objects in a given luminosity bin L_*, and $V_{max(i)}$ is the maximum volume in which the object would be observed to, given the limiting magnitudes/fluxes in both the optical parent Palomar sample and the X-ray sample. The smaller of the two volumes is used, to ensure that the object would be detected in both samples. We place detected sources in bins of equal X-ray power and use Poisson statistics to estimate uncertainties in each luminosity bin. As the LeMMINGs survey is for declinations >20°, the fraction of the sky is limited to 1.316π sr, but for the 'Complete' sample we are limited further to 0.68π sr. The optical Palomar survey is limited to 12.5 mag. We use a flux limit of the X-ray sample, i.e., $1.65{\times}10^{-14}$ erg cm^{-2} s^{-1}.

Figure 6 shows the XLF of the entire X-ray LeMMINGs sample in filled red circles and we fit a power law of slope $\alpha = -0.54 \pm 0.06$ (red dashed line). We also fit the 'active' galaxies, (open black circles), finding a power law of gradient -0.45 ± 0.05, shown by the black dotted line. These two fits differ by 1.2σ. The changes in the overall appearance of the luminosity function is more apparent in the 'active' sources, where the X-ray slope appears to flatten slightly below 10^{39} erg s^{-1}, which may indicate some contamination from non-AGN sources, but this is based off a smaller number of objects and the two fits agree with one another, within the uncertainties.

We also plot in Figure 7 the XLF for the 'Complete' sample in the declination range 40 to 65°, in orange for all galaxies, and blue for the 'active' galaxies. We recalculate the XLF for both the entire and 'active' galaxy samples and find power law fits of -0.48 ± 0.12 and -0.24 ± 0.11, respectively. These two fit values disagree at the 1.5σ level. However, comparing the fit for all galaxies between the entire sample and the Complete sample, yields a difference of 0.5σ, suggesting that the declination-limited Complete sample is not too dissimilar from the entire sample. Furthermore, the fits of the 'active' galaxies differ by 1.7σ between the entire sample and the 'Complete' sample.

Previous studies of the XLF have focussed on sources with X-ray luminosities in excess of $\sim10^{41}$ erg s^{-1} or higher, in order to remove potential contamination from XRBs and ULXs, due to lower resolution X-ray telescopes: *MAXI* (Ueda et al. 2011), *Swift BAT* (Tueller et al. 2008; Ajello et al. 2012), *INTEGRAL*: (Sazonov et al. 2008) and *XMM-Newton* (Fotopoulou et al. 2016). However, our data resolve the nuclear region to 0.5 arcsec with *Chandra*, so it is less likely that we are contaminated by XRBs and ULXs, allowing us to reach X-ray luminosities of 10^{36} erg s^{-1}. Previous XLFs (see Ajello et al. 2012; Ueda et al. 2014; Ballantyne 2014, for a comparison of some of the XLFs in the literature) are described by a broken power-law, which is flatter below $\sim10^{43}$ erg s^{-1}. The power-law slope below 10^{43} erg s^{-1} is found to be between −0.8 and −1.0, though our data show a shallower power-law. However, She et al. (2017) show that for local AGN using *Chandra* data, the power-law is more consistent with a slope of −0.38 for all types of AGN, with the 'active' sources like Seyferts and LINERs showing the flattest power-laws (−0.15 and −0.32, respectively), while H II galaxies and

Correlation	β	α	σ^2	$\hat{\rho}$
(1)	(2)	(3)	(4)	(5)
		log(X-ray):log($M_\odot$)		
Entire, all	$33.83^{+0.49}_{-0.50}$	$0.78^{+0.07}_{-0.07}$	$1.16^{+0.13}_{-0.11}$	$0.64^{+0.04}_{-0.05}$
Entire, $>10^7 M_\odot$	$33.40^{+1.51}_{-1.46}$	$0.83^{+0.18}_{-0.19}$	$0.99^{+0.16}_{-0.13}$	$0.41^{+0.08}_{-0.09}$
'Complete', all	$35.02^{+0.72}_{-0.74}$	$0.62^{+0.11}_{-0.10}$	$1.10^{+0.18}_{-0.15}$	$0.53^{+0.08}_{-0.09}$
'Complete', $>10^7 M_\odot$	$36.91^{+2.17}_{-2.16}$	$0.37^{+0.28}_{-0.28}$	$0.83^{+0.21}_{-0.15}$	$0.20^{+0.15}_{-0.15}$
Entire, Seyferts	$34.98^{+3.82}_{-3.98}$	$0.81^{+0.57}_{-0.55}$	$2.68^{+1.69}_{-0.92}$	$0.42^{+0.24}_{-0.28}$
Entire, LINERs	$33.33^{+0.91}_{-0.89}$	$0.84^{+0.12}_{-0.12}$	$0.69^{+0.13}_{-0.11}$	$0.67^{+0.06}_{-0.08}$
Entire, ALGs	$26.00^{+2.57}_{-2.74}$	$1.66^{+0.34}_{-0.32}$	$0.94^{+0.48}_{-0.28}$	$0.83^{+0.07}_{-0.11}$
Entire, H II gal.	$33.43^{+0.85}_{-0.84}$	$0.85^{+0.13}_{-0.14}$	$1.02^{+0.20}_{-0.16}$	$0.61^{+0.08}_{-0.09}$
		log(X-ray):log([O III])		
Entire, all	$-7.07^{+3.89}_{-4.05}$	$1.22^{+0.11}_{-0.10}$	$0.56^{+0.12}_{-0.11}$	$0.83^{+0.04}_{-0.05}$
'Complete', all	$-5.58^{+6.27}_{-6.74}$	$1.19^{+0.18}_{-0.17}$	$0.46^{+0.14}_{-0.12}$	$0.79^{+0.07}_{-0.08}$
Entire, Seyferts	$-13.72^{+12.05}_{-15.11}$	$1.37^{+0.30}_{-0.38}$	$0.43^{+0.63}_{-0.31}$	$0.93^{+0.05}_{-0.13}$
Entire, LINERs	$-2.55^{+4.90}_{-5.14}$	$1.11^{+0.13}_{-0.13}$	$0.27^{+0.12}_{-0.09}$	$0.88^{+0.04}_{-0.06}$
Entire, H II gal.	$-17.37^{+12.47}_{-14.92}$	$1.49^{-0.33}_{+0.40}$	$0.84^{+0.25}_{-0.23}$	$0.67^{+0.11}_{-0.13}$

Table 7. Table of LINMIX fit parameters, as described in the text, for the X-ray:$M_\odot$ correlations (*top*) and the X-ray:[O III] correlations (*bottom*). The columns are as follows: (1) correlation fit description; (2) y-intercept, α; (3) gradient, β; (4) intrinsic scatter squared, σ^2 - note that this is the direct output from LINMIX, but throughout the text we report the intrinsic scatter i.e. the square root of the value printed above; (5) correlation coefficient, $\hat{\rho}$. The uncertainty values are the 16th and 84th percentile level of the fit for each parameter.

ALGs show steeper power-laws (−0.68 and −0.82, respectively). The general trend of flatter power-laws for 'active' galaxies is also apparent in our sample, with the addition of the ALGs and H II galaxies showing a steepening of the overall power-law slope. Hence, our fits are qualitatively consistent with She et al. (2017).

4.4 X-ray properties vs black hole mass

We now investigate the X-ray luminosity as a function of BH mass (see Figure 8 and Figure 9 for the entire and 'Complete' samples respectively). The black hole masses used in this study are listed in Table 8. When possible, we use dynamical black hole measurements found in the literature (e.g., van den Bosch 2016, which accounts for fifty BH mass measurements in the full 280 objects of the LeMMINGs sample). When not available, the black hole masses are calculated using the relationship between black hole mass and stellar velocity dispersion, known as the $M-\sigma$ relation. The stellar velocity dispersions (σ) are listed in Ho et al. (1997a), while we use the $M-\sigma$ relation obtained in Tremaine et al. (2002). However, the estimation of black hole masses in irregular galaxies and star-forming galaxies like H II galaxies are more uncertain than those in bulge-dominated galaxies, i.e. ellipticals, and those where AGN are known, such as Seyferts and LINERs. The stellar velocity dispersions used to calculate the black hole masses give a standard deviation in $M_{\rm BH}$ fractional error of 0.25 for irregular and star-forming galaxies, whereas it is 0.17 for ellipticals and AGN. These errors are representative of the scatter found in the $M-\sigma$ relation (Tremaine et al. 2002). Furthermore, the M−σ relation used can affect the accuracy of the black hole mass estimate at lower masses and it is uncertain whether a single relation holds across the entire range of galaxy masses (Dullo et al. 2020, submitted). However, we compared the M−σ relations of Tremaine et al. (2002), Kormendy & Ho (2013) and Graham & Scott (2013) and found that for black hole masses above 10^7 $M_\odot$ the scatter was 0.5 dex, but below 10^6 $M_\odot$ the scatter increased to 1 dex (see Baldi et al. 2018). Shankar et al. (2016, 2019) also discuss potential biases in the normalisations of both the $M_{\rm BH}-\sigma$ and $M_{\rm BH}-M_{\rm gal}$ relations. However, these amount to at most a factor of ∼2−3 in the mean normalization of the $M_{\rm BH}-\sigma$ relation, and they would not alter the already very broad dispersion in the $L_{\rm X}-M_{\rm BH}$ correlation substantially.

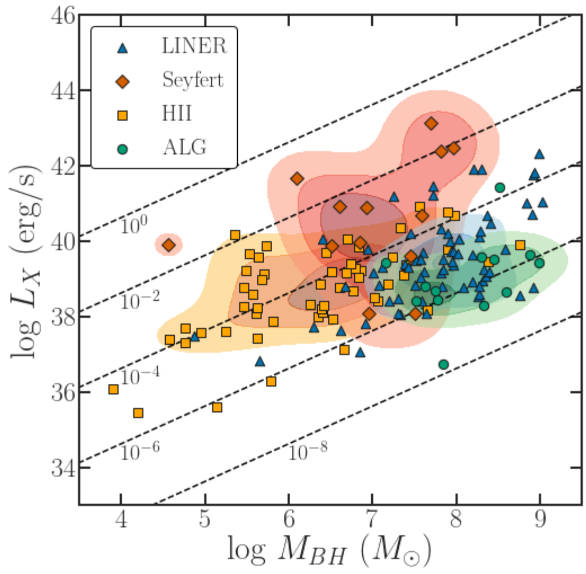

Figure 10. The unabsorbed X-ray 0.3−10.0 keV luminosities ($L_{\rm X-ray}$ in erg s^{-1}) as a function of the BH masses for the detected sources in the sample, divided per optical class. The dashed lines represent the Eddington ratios λ to compare to the X-ray luminosity and BH masses. Each Eddington ratio is labelled next to a dashed line. The uncertainties are not shown but can be seen in Figure 8. In addition we plot the 1, 2 and 3 σ levels of the distributions for each AGN type in their respective colours.

In general, the detection rate of X-ray sources increases with BH mass. The detection fraction for the entire sample objects with BH masses $\gtrsim 10^8 M_\odot$ is 88 per cent (36/41), but below $10^6 M_\odot$, the detection fraction falls to 50 per cent (26/52). Of the five undetected objects with $\gtrsim 10^8 M_\odot$, four of them are ALGs. A similar distribution exists for the 'Complete' sample: 12/13 (92 per cent) detection fraction for $\gtrsim 10^8 M_\odot$ and 16/29 (55 per cent) for $\lesssim 10^6 M_\odot$.

While the black hole masses range over ∼5 orders of magnitude (see Figure 8), there are clear distinctions in the different types of AGN nucleus. The detected Seyfert galaxies tend to have the highest X-ray luminosities for each mass bin, when compared to other AGN types. They generally cluster 1−2 decades above the other AGN types in X-ray luminosity (see also Figure 9 and Figure 10). There is a large distribution in the LINER X-ray luminosity of order 2–3 decades. The detected ALGs tend to lie in the same mass bins as the LINERs, but at slightly lower X-ray luminosities ($\sim 10^{39}$ erg s^{-1}). The low mass H II galaxies are not often detected, but they appear to follow the same overall trend as the rest of the detected X-ray population, but with a larger distribution towards the lowest BH masses.

We test the correlation between X-ray luminosity and BH mass, using LINMIX[5]: a Bayesian framework that folds in uncertainties in both axes as well as upper limits in the y axis (Kelly 2007). LINMIX can provide the gradient, y-intercept, the scatter and the correlation coefficient ($\hat{\rho}$) for a given fit. We note that two of the sources (NGC 1003 and NGC 4242) have upper limits on both black hole mass and X-ray luminosity. The LINMIX package is unable to handle upper limits in both axes simultaneously so we remove these two sources from the fits. In Figure 8 and Figure 9, we display 400 draws from the fitting process to give a visual guide to the scatter in the correlations. As an additional analysis, we computed the correlation for sources with black hole masses greater than 10^7 M$_\odot$, in order to find show any global difference in the slope at lower masses, in analogy to a break found in the radio LeMMINGs sample (Baldi et al. 2018, 2021b).

We find a correlation for the 'Complete' sample sources (solid black line in Figure 9) to be of the form $L_{\rm X-ray} \sim {\rm M}_\odot^{\ 0.62^{+0.11}_{-0.10}}$, with an intrinsic scatter of 1.05 dex (correlation coefficient, $\hat{\rho}$ = $0.53^{+0.08}_{-0.09}$). The uncertainty values are the 16th and 84th percentile level of the fit parameters and we show these in full in Table 7. The black dashed line shows the correlation for 'Complete' sample sources above 10^7M$_\odot$, which is $L_{\rm X-ray} \sim {\rm M}_\odot^{\ 0.37\pm0.28}$ and an intrinsic scatter of 0.91 dex ($\hat{\rho}$ = $0.20^{+0.15}_{-0.15}$). The correlation coefficients indicate a positive correlation, but the $>10^7$M$_\odot$ correlation is very weak. For the entire sample, we find slightly different fits, of $L_{\rm X-ray} \sim {\rm M}_\odot^{\ 0.78\pm0.07}$ (scatter = 1.08 dex, $\hat{\rho}$ = $0.64^{+0.04}_{-0.05}$) for the entire sample and for those above a black hole mass of 10^7M$_\odot$, we find a correlation of the form $L_{\rm X-ray} \sim {\rm M}_\odot^{\ 0.83^{+0.18}_{-0.19}}$ (scatter = 1.00 dex, $\hat{\rho}$ = $0.41^{+0.08}_{-0.09}$). We note that the entire sample includes more galaxies at higher X-ray luminosities which may provide a reason for the steeper gradients and stronger correlation coefficients, but, given the uncertainties in the fits, the entire and Complete sample values agree with one another within $\sim 1\sigma$. Therefore, we do not find a break X-ray-M$_\odot$ relation as in the LeMMINGs radio-M$_{BH}$ relation (Baldi et al. 2018, 2021b).

We also investigated the correlations in each type of AGN, using the entire sample due to the low numbers of objects in the 'Complete' sample for all AGN types. We further note that the entire sample does not appear to differ significantly from the statistically-complete sub-sample. For Seyferts, we find a correlation of $L_{\rm X-ray} \sim {\rm M}_\odot^{\ 0.81^{+0.57}_{-0.55}}$ (scatter = 1.64 dex and $\hat{\rho}$ = $0.42^{+0.24}_{-0.28}$). In the literature, correlations between X-ray luminosity and BH mass have led to mixed results (e.g., Koratkar & Gaskell 1991; Kaspi et al. 2000; Pellegrini 2005; Panessa et al. 2006). Given the low number of Seyferts in our sample, the large scatter in correlation and the poor correlation coefficient presented here, it is not possible to find any strong correlation between the X-ray luminosity and BH mass for Seyferts.

We performed the same analysis for the LINERs, ALGs and H II galaxies and found them to all be correlated between the X-ray luminosity and BH mass. The LINER correlation is $L_{\rm X-ray} \sim {\rm M}_{\rm BH}^{0.84\pm0.12}$ with a scatter of 0.83 dex. The H II galaxies follow a correlation of $L_{\rm X-ray} \sim {\rm M}_{\rm BH}^{0.85^{+0.13}_{-0.14}}$ with an intrinsic scatter of 1.01 dex. For the ALGs, the correlation is $L_{\rm X-ray} \sim {\rm M}_{\rm BH}^{1.66^{+0.34}_{-0.32}}$ with a scatter of 0.91 dex. Given the low detection fraction and the low number of objects, we do not claim a significant correlation for ALGs. For the LINERs and H II galaxies, they have remarkably similar fit parameters and intermediate correlation coefficients, suggesting that H II galaxies may be similar to LINERs, although we note there is up to 1 dex of scatter in both relations. This finding may represent a continuation of the LINERs down to lower X-ray luminosities, but the uncertainties on sources at lower black hole masses ($<10^6$M$_{\rm BH}$) is larger, so these correlations are driven by the higher mass objects. Indeed, removing sources below 10^6M$_{\rm BH}$ results in the same fits, but fitting only sources $<10^6$M$_{\rm BH}$ leads to unconstrained or very poorly constrained fits in all cases.

4.5 Eddington Ratio

In addition to the fits presented above, we compared the 2−10 keV X-ray luminosity and BH mass plot to the Eddington ratio,

$$\lambda = \frac{\rm L_{bolometric}}{\rm L_{Eddington}} \tag{2}$$

for the detected sources in the sample in Figure 10. In order to compare these quantities, we assume that the bolometric luminosity = 30×X-ray luminosity in the 2.0−10.0 keV band following (Panessa et al. 2006). This assumption is very simplistic, as the bolometric luminosity relies on the shape of the spectral energy distribution for the AGN, which could differ amongst LLAGN types. Furthermore, the value of 30 is valid for more powerful AGN, but observationally, this value ranges from 3 to 16 (Ho 1999b), approximately consistent with the theoretical calculations of optically-thick and geometrically thin accretion disks (Netzer 2019). Hence, as discussed in Panessa et al. (2006), for a lower scaling value of $L_{\rm bol}$ to $L_{\rm X-ray}$, for example 10, the lines on Figure 10 would drop by a factor of 3. However, even with these approximations, the 1, 2 and 3σ shaded distributions[6] in Figure 10 show that the Seyferts are associated with the higher a mixture of Eddington ratios, from values $\gtrsim 10^{-3}$, but with a number below this dividing line region with Eddington ratios of $\lesssim 10^{-3}$. Furthermore, the contour plots show the similarity of the LINERs and ALGs, suggesting that the ALG population are similar to low X-ray luminosity LINERs. We performed a two-dimensional, two-sample KS test on these regions for ALGs and LINERs, and found a p-value of 0.06. This p-value suggests evidence for the null hypothesis, indicating that these two samples are not statistically different from one another. For all other combinations, the p-values returned were $\ll 0.05$ and so we can reject the null hypothesis, i.e., the distributions are not drawn from the same sample. For the H II galaxies, they are found in a similar X-ray luminosity region to the LINERs (and ALGs), but at lower masses.

As a final analysis, Figure 11 shows histograms of the ratio between the X-ray luminosity and black hole mass, which can be used as a tracer of the accretion rate, split once more by AGN and Hubble types. For the different AGN-types, including the 'inactive' galaxies, H II galaxies have the largest ratios of X-ray luminosity to black hole mass, assuming the emission is from AGN-activity. The next largest ratio are found in Seyferts, suggesting that they are higher accretion

[5] A PYTHON module can be obtained from `https://linmix.readthedocs.io/en/latest/index.html`

[6] The contour plots are made with `corner` (Foreman-Mackey 2016).

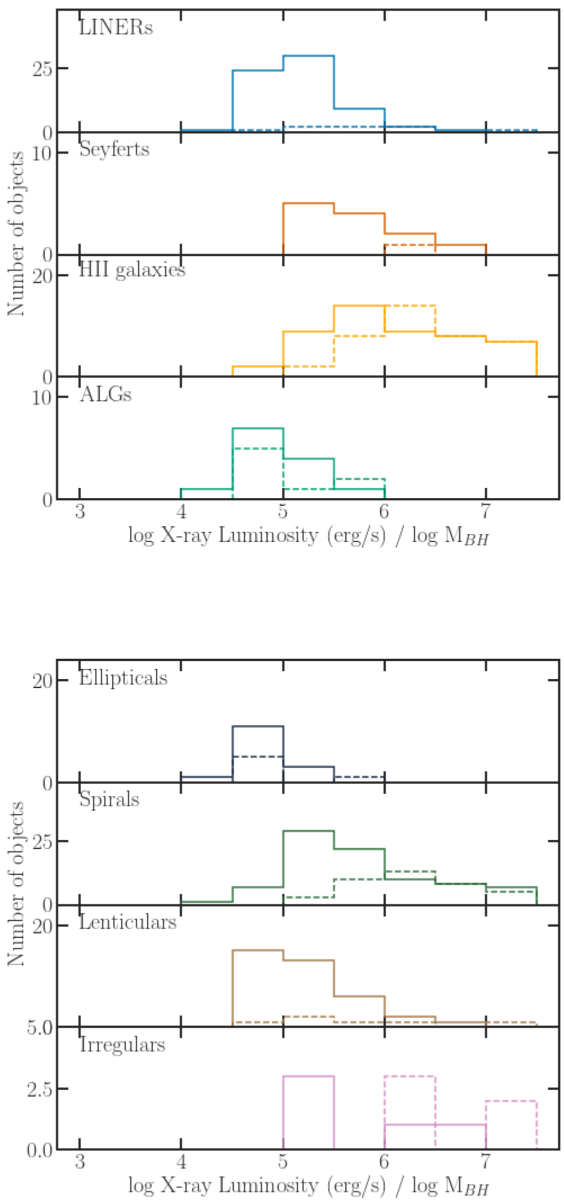

Figure 11. Histograms of the X-ray luminosity divided by the black hole mass - a tracer of the accretion rate - per optical class (top plot) and host morphological type (bottom plot). The solid-line histogram represents the X-ray core luminosity distribution of the detected sources and the dashed line corresponds to the upper limits obtained from the non-detected objects.

rate objects. LINERs and ALGs have lower ratios of X-ray luminosity to black hole mass, consistent with the lower accretion rates in Figure 10. However, it should be noted that H ii galaxies generally fall in the lower mass bins in Figure 11 and have larger error bars. To test whether the black hole masses may be driving this correlation, we removed all sources with mass errors in log space >0.1, so as to only include those with robust mass measurements. This cut leaves seventy sources and also has the effect of removing sources with black hole masses $<10^6$M$_{\rm BH}$. In-so-doing, the H ii galaxies appear to have more similar accretion rates to those of Seyferts and LINERs, with all H ii galaxies with ratios of X-ray luminosity to black hole mass larger than six being removed. In terms of the Hubble types, spirals and irregular galaxies show higher X-ray to black hole mass ratios, which may be correlated with the prevalence of H ii galaxies having larger ratios. Ellipticals and lenticulars are more prevalent in the lower X-ray luminosity to black hole mass bins, suggesting lower accretion rates.

4.6 Spectral Properties of the X-ray sources

We now look to the best fit *Chandra* spectra described in Section 3. The spectra and best fit flux values are reported in the Appendix for each galaxy in Table 10. Here, we analyse the spectra in more detail, comparing them to the AGN type and galaxy morphological types.

4.6.1 Absorption

In Section 3 we fitted all spectra with an absorbed power-law and additional simple models where an absorbed power-law was insufficient. For objects detected with a significance of $>5\,\sigma$, we summed all the neutral absorbers and report a total absorption from these additional models. For sources detected between 3−5 × the detection significance in their image, we fixed the photon index to 1.8 to find the total absorbing column. From this analysis, we are able to report the total absorbing column, which we show in Figure 12, binned by AGN type. In this figure, we also show the Galactic line-of-sight $N_{\rm H}$ contribution for the undetected sources in the upper histogram. For a large number of the detected sources (80/150, 53 per cent), only upper limits to the host galaxy absorbing columns were found. Excluding sources with upper limits on their host galaxy absorption, we have 70 remaining galaxies, from which we could ascertain a value of $N_{\rm H}$. Of these sources, 49 (70 per cent) have total absorbing columns of $<10^{22}$ cm^{-2}. These sources therefore are not heavily obscured as they have an Hydrogen column densities less than the average Galactic value, in contrast with studies of other AGN (Burlon et al. 2011; Ricci et al. 2015; Boorman et al. 2018). A source with an absorbing column $>1.5\times10^{24}$ cm^{-2} is called "Compton-thick", which denotes that it is significantly obscured (Comastri 2004; Boorman et al. 2018). In our sample, we find no sources which can be considered Compton-thick, although four sources (NGC 1161, NGC 3729, NGC 4111 and NGC 7640) have an absorbing column of $>1.0\times10^{23}$ cm^{-2}. We therefore confirm that the nuclei of our sample are typically unobscured, with a large fraction (129/150, 86 per cent) have host galaxy absorbing columns of less than that of the Galaxy, e.g., $<10^{22}$ cm^{-2}.

Obtaining a reliable estimate of the obscuring column density from X-ray spectra requires a reliable estimate of photoelectric absorption as well as reprocessing (collectively Compton scattering and fluorescence) of the intrinsic AGN emission. For heavily obscured and Compton-thick AGN, this reprocessing can dominate the observed spectral emission, manifesting as a flat spectrum at $E \lesssim 10$ keV, a strong neutral Fe Kα fluorescence line at rest energy 6.4 keV and a broad Compton hump peaking at $E \sim 30$ keV (e.g., Lightman & White 1988; Reynolds et al. 1999; Matt et al. 2000; Murphy & Yaqoob 2009). However, the Fe Kα fluorescence line is not always found to be strong in Compton-thick AGN (e.g., Gandhi et al. 2017; Boorman et al. 2018) and our spectral coverage provided by *Chandra* does not cover the Compton hump > 8 keV. It is thus difficult to constrain high columns with our phenomenological modelling presented here. In fact, a number of our sources have been classified as Compton-thick by previous works using spectra above 10 keV: NGC 2273 (Brightman et al. 2017); NGC 3079 (Brightman et al. 2017; Marchesi et al.

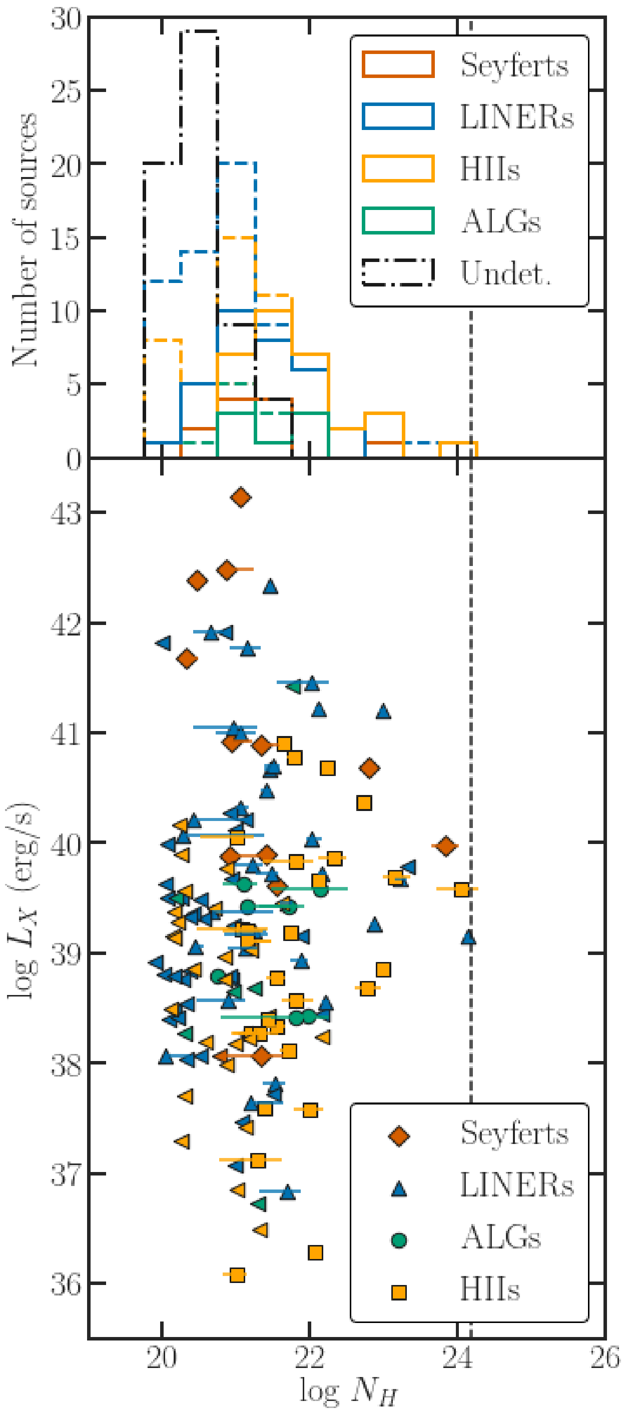

Figure 12. The X-ray luminosity of the entire X-ray sample as a function of absorbing column (N_H). For sources with detection significances between 3−5σ in the image, we fixed the photon index to 1.8 and obtained a host galactic absorption (see Section 3). For the objects with luminosities >5× the detection significance in their image, we used the best fit values, summing together all neutral absorbers and report in this plot the total absorption from the fits. We also show in the *top panel* the Galactic absorption along the line-of-sight to the galaxy for the undetected sources. We show histograms of the N_H distribution for detected sources where we could contrain the absorbing column by AGN type (solid lines) and all sources including upper limits by AGN type (dashed lines). In the *bottom panel*, we split the sources by AGN Type. In all cases, left pointing triangles denote upper limits. In both panels we draw a black dashed line which denotes our "Compton-thick" definition, of which no sources are to the right of this line, although some other sources do have values which are close to or their uncertainties pass over this line.

2018); NGC 3982 (Kammoun et al. 2020); NGC 4102 (Ricci et al. 2015; Marchesi et al. 2018) and NGC 5194 (Brightman et al. 2017).

Interestingly, NGC 3079 and NGC 4102 are found to display non-Seyfert BPT line ratios in our sample (LINER and ALG, respectively), yet are intrinsically-luminous heavily obscured Seyferts. In addition, some of the LINERs in our sample (NGC 2639, NGC 4589, NGC 5005, NGC 5866 and NGC 7331) may also be Compton Thick as shown from a sample of X-ray spectra of LINERs (González-Martín et al. 2015). This hints to a population of obscured Seyferts amongst the optically-classified ALGs, HIIs and LINERs, that hard X-ray spectra could elucidate. However, due to a significant lack of *NuSTAR* coverage in our sample (41/280 ~ 15 per cent), a statistically-complete spectral analysis combining *Chandra* and *NuSTAR* is currently not possible. Future observations with *NuSTAR* will enable broadband spectral fits with *Chandra* using physically-motivated obscurer models which are capable of constraining high columns, even into the Compton-thick regime (e.g., Masini et al. 2019; Kammoun et al. 2019; LaMassa et al. 2019). Such observations will shed light on the true proportion of Seyferts in our sample, as well as the Compton-thick fraction in the local Universe.

4.6.2 *Photon index*

Figure 13 shows the photon index from the spectral fits (see Section 3) of the entire sample, broken down into AGN types and Hubble types. In both cases we separate all the data (solid line histograms) from those that had luminosities $>10^{39}$ erg s^{-1} (filled histograms). While most of these classifications have a peak number of sources within the photon index range 1.75−2.00 or in adjacent bins, there is no clear distinction in the distributions between any AGN type or Hubble type. LINER and Seyfert galaxies, spirals and lenticulars show a peak in the 1.75−2.0 bin. The distributions for the photon indices in all classification types span the range of fit values found in Section 3 (see Figure 3). Furthermore, removing sources with luminosities $<10^{39}$ erg s^{-1} does not reduce the breadth of these histograms. We therefore find no evidence that spectral index is significantly affected by optical spectral or morphological type. This finding hints at the variety of different X-ray emitting nuclei in the local Universe and that if interpreted as AGN, that these nuclei can be found across a wide range of galaxy types and AGN classifications.

4.6.3 *Eddington Ratio*

The accretion rate can be approximated using the ratio between the X-ray luminosity and the Eddington luminosity, as described in the previous Section. We now plot the photon index as a function of this ratio in Figure 14, similar to that performed by Connolly et al. (2016) for a sample of 24 Palomar galaxies (their Figure 8). We only plot sources with luminosities $>10^{39}$ erg s^{-1} and have a reliable photon index fit value i.e., no upper limits. This cut limits our sample to 63 sources. To compare directly to Connolly et al. (2016), we use the harder 2−10 keV band fluxes for this figure. We also include the fits for higher Eddington rate radio-quiet AGN (Shemmer et al. 2006) and for LLAGN (Constantin et al. 2009), as shown in Connolly et al. (2016). Our data generally probe the lower ($<10^{-3}$ L_X/L_{Edd}) regime, although a handful of objects (notably NGC 4051, NGC 4395 and NGC 5548), are above this threshold. The overall trend follows that of Constantin et al. (2009) for the lower accretion rate objects ($<10^{-3}$ L_X/L_{Edd}). We do not have enough objects which have accretion rates $>10^{-3}$ L_X/L_{Edd} to compare with the results of Shemmer et al. (2006), but we do note that most of the objects

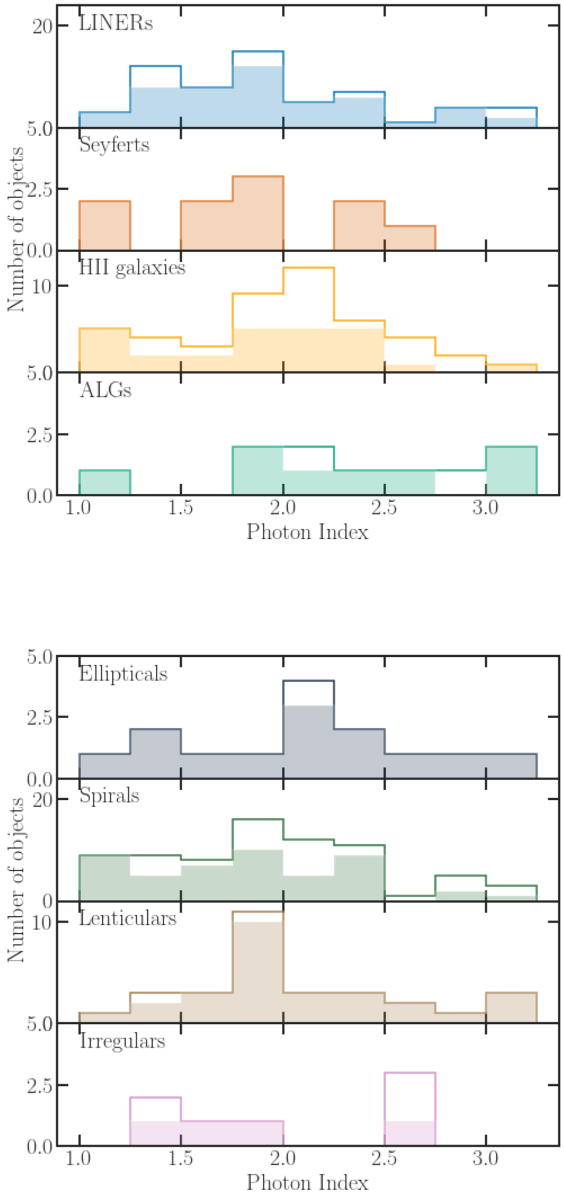

Figure 13. Histograms of the Photon Index from the best fit models of the detected sources in the entire sample, separated by AGN Type (top panel) and Hubble type (bottom panel). The solid lines in all cases represent the best spectral fits, whereas the filled histograms represent the sources with luminosities greater than 10^{39} erg s^{-1}.

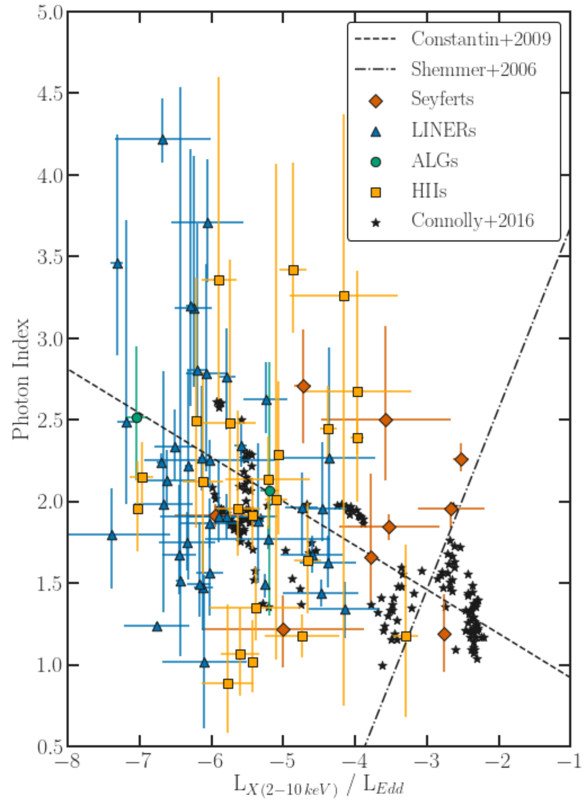

Figure 14. Photon index of the entire sample where reliable photon indices were extracted from the spectra and the source luminosity is $>10^{39}$ erg s^{-1} plotted against the tracer of the accretion rate, defined by the ratio between $L_{\rm X-ray\,(2--10\,keV)}$ and $L_{\rm Edd}$, split by different AGN types. We also plot the results from the study by Connolly et al. (2016), which includes a sample of 24 Palomar galaxies, but we include averaged values of the data points included in that study. The lines correspond to the fits from Shemmer et al. (2006) for higher Eddington rate radio-quiet AGN and Constantin et al. (2009) for LLAGN.

that fall near this line are Seyferts and broadly follow the correlation. However, given the large errors and scatter in the range of photon indices for this sample, it is difficult to draw significant conclusions on these data. Longer exposure observations are required to further constrain the photon indices in these objects to further probe these relations.

4.7 X-ray compared to [O III] line luminosity

When X-ray observations are not available, the forbidden [O III] line luminosity, which is easier to measure from ground based instruments, is used as a proxy for the X-ray luminosity (e.g., Panessa et al. 2006; Hardcastle et al. 2009; González-Martín et al. 2009; Saikia et al. 2015, 2018a). The above relationships have generally been obtained at relatively high luminosities. Given the usefulness of this relationship it is important to take advantage of our present *Chandra* data to derive the relationship with to lower X-ray luminosities. Future observations can provide [O III] luminosities of similarly improved spatial resolution as the Palomar line data used here from Ho et al. (1997a) is not of particularly high spatial resolution and may be contaminated by some level of SF.

The *top* panel of Figure 15 shows the [O III] line luminosity obtained from the Palomar survey of all the detected and undetected X-ray sources plotted against the X-ray luminosity in the 0.3−10 keV band. This correlation for the 'Complete' sample is shown in *bot-*

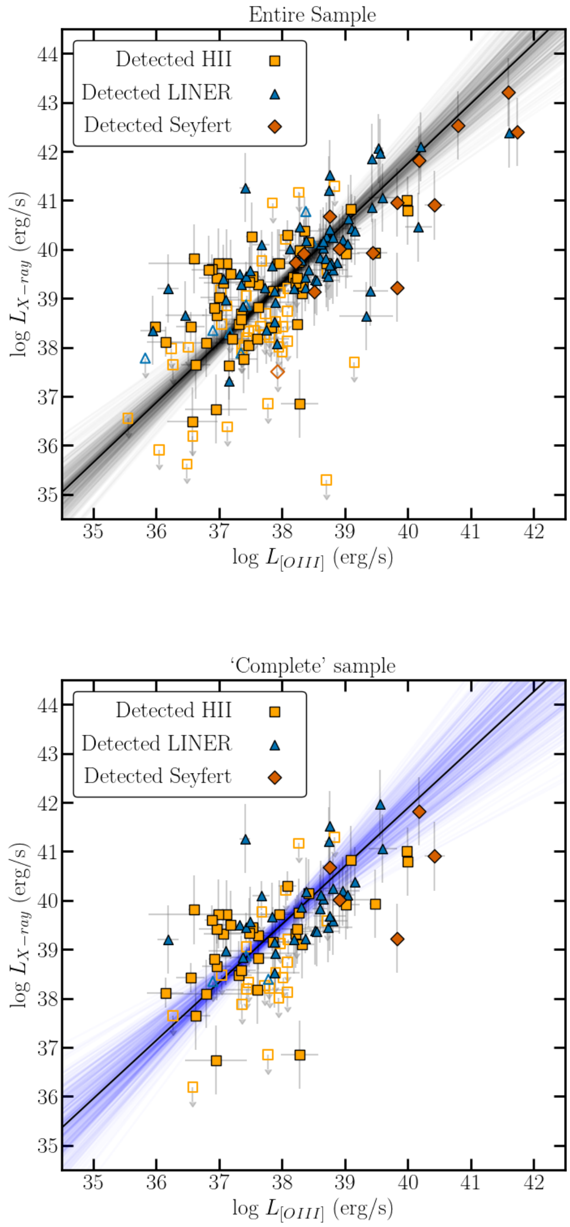

Figure 15. The [O III] luminosity vs unabsorbed 0.3–10.0 keV luminosities for the entire (*top* panel) and 'Complete' (*bottom* panel) X-ray sample. The different optical classes are coded (symbol and colour) in the plot according to the legend. The filled symbols refer to the detected X-ray sources, while the empty symbols refer to undetected X-ray sources. The black line represents the correlation discussed in Section 4.7 and the black/blue (entire/Complete) region shows 400 draws from the fit, to give an idea of the fit uncertainty. The correlation information is given in the text.

tom panel of Figure 15. Once more, we use the LINMIX package to include upper limits in the X-ray luminosity and show all of our correlation results in Table 7. The correlation is of the form $\mathrm{L_{X-ray}} \sim \mathrm{L}_{[\mathrm{O\,III}]}^{1.22^{+0.11}_{-0.10}}$ with a scatter of 0.75 dex for the entire sample ($\hat{\rho}$ = $0.83^{+0.04}_{-0.05}$) and $\mathrm{L_{X-ray}} \sim \mathrm{L}_{[\mathrm{O\,III}]}^{1.19^{+0.18}_{-0.17}}$ with a scatter of 0.83 dex for the 'Complete' sample ($\hat{\rho}$ = $0.79^{+0.07}_{-0.08}$).

The scatter in the correlation is larger at lower X-ray and [O III] line luminosities. The LINERs and Seyferts have the highest [O III] and X-ray luminosities of the sample, whereas the H II galaxies are at the lowest X-ray and [O III] luminosities. However, there is a lot of mixing between all the classes, so no clear region for each optical AGN class emerges. Fitting each of the three optical AGN types separately for the entire sample, we arrive at fits of $\mathrm{L_{X-ray}} \sim \mathrm{L}_{[\mathrm{O\,III}]}^{1.37^{+0.38}_{-0.30}}$ with a scatter of 0.66 dex for Seyferts ($\hat{\rho}$ = $0.93^{+0.05}_{-0.13}$), $\mathrm{L_{X-ray}} \sim \mathrm{L}_{[\mathrm{O\,III}]}^{1.11^{+0.13}_{-0.13}}$ with a scatter of 0.52 dex for LINERs ($\hat{\rho}$ = $0.88^{+0.04}_{-0.06}$) and $\mathrm{L_{X-ray}} \sim \mathrm{L}_{[\mathrm{O\,III}]}^{1.49^{+0.40}_{-0.33}}$ with a scatter of 0.92 dex for H II galaxies ($\hat{\rho}$ = $0.67^{+0.11}_{-0.13}$). These fits are all consistent with one another, within the uncertainties and show a strong positive correlation. Furthermore, the low scatter in the LINERs and Seyferts shows a tight correlation between the [O III] line luminosity and X-ray luminosity in these objects, whereas the larger scatter in the H II galaxies add scatter to the overall relation, especially at the lowest luminosities.

Previous work has shown that the X-ray-[O III] correlations tend to show a ∼1:1 ratio, similar to that found here for the Seyferts (Panessa et al. 2006; Hardcastle et al. 2009). The X-ray LeMMINGs data corroborates these findings, indicating that the X-ray and [O III] ionising radiation are coupled down to very low luminosities, albeit with some additional scatter. A similar correlation is found for LINERs (e.g., González-Martín et al. 2009) and it is interesting that the H II galaxies follow a similar correlation to the Seyferts and LINERs. However, we note that the X-ray emission from the LINERs may be coming from the jet rather than accretion flow (e.g., see Balmaverde & Capetti 2006).

5 DISCUSSION

We have presented X-ray observations of 213/280 objects in the Palomar survey above δ = 20°, that as of June 2018 have been observed with *Chandra*. Altogether, 150/213 (70 per cent) objects were detected, which is higher than previous studies of a subset of the Palomar sample using poorer resolution/quality data from *ROSAT* (54 per cent, Roberts & Warwick 2000) and *Chandra* (62 per cent, Ho & Ulvestad 2001). For matching resolution X-ray observations with *Chandra* presented by She et al. (2017), we find similar detection fractions for all types of AGN. We find that almost all Seyferts, ALGs and LINERs have a nuclear X-ray core, co-incident with the optical nucleus of the galaxy. In addition, around half of the H II galaxies in the sample are detected in the X-rays at the optical nucleus. As to the nature of these X-ray sources, the LINERs and Seyferts appear to be associated with luminosities $\gtrsim 10^{39}$ erg s^{-1} in most cases, but the H II galaxies and ALGs represent a less-luminous population of nuclear X-ray emission that may be due to LLAGN, or potentially other X-ray sources in the galaxy such as ULXs or XRBs. To ascertain the nature of the nuclear emission, we used the other multi-wavelength data available, which we discuss below in the case of each of the AGN types.

5.1 Seyferts

There are 14 Seyferts in the entire X-ray LeMMINGs sample, of which 13 are detected (93 per cent), but this detection fraction is 100 per cent in the Complete sample (5/5 objects). The only Seyfert that is not detected is NGC 3486, which has only a ∼2 ks observation and is a type II Seyfert which may be obscured by large absorption along the line of sight. The Seyferts have the highest X-ray luminosities ($>10^{39}$ erg s^{-1}), occupying regions of higher X-ray luminosity per black hole mass bin and [O III] emission line luminosity. We do not report a correlation between the X-ray luminosity and the black hole mass for Seyferts. The lack of correlation is likely caused by the large scatter in any relation due to the wide range of Eddington values in this class (see Figure 10), with some Seyferts showing Eddington ratios as low as 10^{-6}. The low number of Seyferts in this sample prevents us from making firmer conclusions on this correlation. The higher Eddington ratio ($\lambda \sim 10^{-2}$) Seyferts obtained from the X-ray data indicate that in general, Seyferts accrete efficiently, likely in the form of an optically-thick, geometrically thin accretion disk (Shakura & Sunyaev 1973). They are likely scaled down versions of the more powerful AGN in quasars, accreting at lower Eddington ratios (Panessa et al. 2006). However, for the Seyferts that have lower Eddington ratios ($\lesssim 10^{-3}$ Merloni et al. 2003), they could possibly be powered by some form of radiatively inefficient accretion flow (see Section 5.2).

5.2 LINERs

Of the 77 LINERs in the entire X-ray sample, 69 of them are detected (90 per cent), which is similar to the detection rate in the 'Complete' sample (35/38, 92 per cent). They are mostly detected with luminosities $\gtrsim 10^{39}$ erg s^{-1} and are associated with the highest BH masses. They follow a similar X-ray/[O III] gradient to the Seyferts. LINERs are often described by some form of radiatively inefficient accretion flow (RIAF e.g., Narayan et al. 1997, 1998). Our X-ray observations support this interpretation as the inferred Eddington ratios in Figure 10 indicate that most LINERs have $\lambda \lesssim 10^{-4}$ and much weaker X-ray luminosities than those of Seyferts. X-ray emission from shocks or post-AGB stars would not be able to explain such high nuclear X-ray luminosities (Allen et al. 2008; Sarzi et al. 2010; Capetti & Baldi 2011; Singh et al. 2013). We also note that some of the X-ray emission in the LINERs may come from the jet rather than the accretion flow (see Balmaverde & Capetti 2006; Balmaverde et al. 2008). We therefore suggest that most of the LINERs in our sample may be powered by a form of RIAF, but further follow-up observations are required of this sample to unequivocally determine the accretion mechanism in LINERs.

5.3 Absorption Line Galaxies

Absorption Line galaxies (ALGs) have often been missed in previous X-ray surveys, as they are not considered 'active', like the Seyferts and LINERs. However, they have a reasonable detection fraction 13/22 (59 per cent) in the entire sample and 8/11 (73 per cent) in the 'Complete' sample. They are associated with X-ray luminosities similar to the LINERs, around 10^{39} erg s^{-1}. ALGs tend to be better detected in the higher mass bins but appear in similar regions to LINERs in terms of Eddington ratio (Figure 10), it is possible that they may have a common central engine (Baldi & Capetti 2010; Baldi et al. 2018, 2021b). Nonetheless, the ALGs are mostly associated with elliptical galaxies and the lack of a detection of the [O III] line limits the interpretation of the central engine. Furthermore, the low implied X-ray luminosities in some of the ALGs (see upper limits in Figure 5), indicates that they may not be identical to LINERs. An alternative explanation for the central engines of ALGs is the nuclear recurrence scenario due to an intermittent accretion phenomenon (Reynolds 1997; Czerny et al. 2009). Further dedicated studies at higher sensitivities of ALGs should be undertaken to ascertain the true cause of their X-ray and multi-wavelength emission.

5.4 H II galaxies

Of the 100 H II galaxies observed by *Chandra* in our sample, 57 were detected in the X-ray (57 per cent). In the 'Complete' sample, the H II galaxies have a similar detection fraction: 35/58 (60 per cent). Of the detected objects, 32/57 (56 per cent) are of X-ray luminosities $\gtrsim 10^{39}$ erg s^{-1}, similar to that of LINERs and Seyferts. The H II galaxies span a range of accretion rates and BH masses, but follow similar correlations to the Seyferts and LINERs, specifically the X-ray/M_{BH} and X-ray/[O III] relations, and especially at the higher black hole masses. Therefore the H II galaxies with a detected X-ray core, and X-ray luminosity $\gtrsim 10^{39}$ erg s^{-1} and a BH mass $\gtrsim 10^{7} M_{\odot}$, are likely powered by an AGN. But, there could still be some contribution from SF processes to both the [O III] and X-ray luminosities. It is not clear whether the majority of these objects are powered by ineffcient flows, similar to LINERs, or a more efficient accretion mode, similar to Seyferts. However, (Baldi et al. 2018, 2021a) found some 'jetted' H II galaxies which could be more consistent with LINER-like activity. For the 25 H II galaxies that do not fulfil these requirements, e.g., detected H II galaxies at lower masses and X-ray luminosities, their central engines are more uncertain, and further investigation is required to classify them as genuine LLAGN or imposters in the form of XRBs and ULXs (see next Section). Furthermore, it should be noted that the central object of 43 per cent of the H II galaxies are undetected, so deeper X-ray observations are needed in order to fully understand the central engines in these objects.

5.5 Is there any contamination from XRBs and ULXs?

Given the 0.5 arcsec on-axis resolution of *Chandra*, we considered X-ray sources which lie within 2 arcsec of the optically defined nucleus as likely being powered by a central SMBH. However, some of these sources may not be an AGN, but may be a ULX/XRB, as is observed in NGC 3034 (Muxlow et al. 2010). In addition, nuclear star formation from O/B star associations can be as luminous as 10^{35} erg s^{-1} (Oskinova 2005) and could cause further contamination. We computed XLFs for the sample, and showed that it is unlikely we are heavily biased to non-AGN sources contaminating the nucleus, as our XLFs are shallower than those expected of ULXs and XRBs (see She et al. 2017, and references there-in). However, the XLFs are steeper when the 'inactive' galaxies are included in both the entire and 'Complete' samples, so some small contamination may be possible in those galaxies. If a discriminating X-ray luminosity of 10^{39} erg s^{-1} is used as a criterion to remove non-AGN sources, then 13/13 detected Seyferts, 56/68 LINERs, 11/13 ALGs and 32/56 H II galaxies would be considered AGNs for the entire sample. By Hubble types, 14/15 ellipticals, 59/91 spirals, 33/35 lenticulars and 6/9 irregulars would be considered AGNs. This definition shows that of all types, H II galaxies, spirals and irregulars are the most likely to be contaminated with ULX/XRBs. Unsurprisingly, this link has been observed previously between star formation and prevalence of ULXs in a galaxy (King 2004; Gilfanov et al. 2004; Swartz et al. 2009). But, it is also possible for a $<10^{39}$ erg s^{-1} LLAGN to co-exist with ULX/XRBs in a galactic nucleus. Therefore, additional information is needed to categorically remove spurious non-AGN sources from the sample. However, SMBHs are more radio loud than stellar mass sized black holes and in a future publication (Pahari et al. in prep), we will include radio luminosity in our decision as to whether nuclear sources are SMBHs or a contaminating source.

6 CONCLUSIONS

We have presented archival and new *Chandra* X-ray observatory data for 213/280 (76 per cent) objects in the declination limited ($\delta > 20°$) Palomar sample, and 112/113 of the Palomar galaxies in the sub-sample between $40° < \delta < 65°$, which we refer to as the 'Complete' sample. Although most galaxies have a considerably longer exposure time, we achieve a minimum observation time of 10 ks on all observed targets. Using these data, we achieve a background flux level of $\sim 1.65 \times 10^{-14}$ erg cm^{-2} s^{-1}. The entire X-ray LeMMINGs sample has detected X-ray emission co-incident with the optical centre of 150/213 (70 per cent) of the observed galaxies across all optical AGN types and galaxy morphologies. The 150 X-ray detected galactic nuclei were fit with simple spectral models in XSPEC and their fluxes computed in the 0.3−2.0, 2.0−10.0 and 0.3−10.0 keV bands. The detection rate of our *Chandra* data of nuclear X-ray emission compares favourably to previous X-ray studies of the Palomar sample: 70 per cent detections compared to 54 per cent in Roberts & Warwick (2000) and 62 per cent in Ho & Ulvestad (2001). Comparing to a previous work based on *Chandra* data by She et al. (2017), we find broadly similar results: X-ray emission associated with the AGN is observed ~80 per cent of the time in Seyferts, LINERs and ALGs, but also in H ii galaxies in 50 per cent of objects.

We determined an X-ray luminosity function (XLF) from the data in our sample and fit a simple power-law of -0.54±0.06 for the entire sample and -0.45±0.05 for the 'Complete' sample, for all galaxies. Our data probes lower X-ray luminosities than most previous studies (e.g. Ajello et al. 2012), extending the X-ray luminosity function down to 10^{36} erg s^{-1}, two orders of magnitude lower than the previous *Chandra* observations (She et al. 2017). We further split the entire and 'Complete' samples into 'active' sources such as LINERs and Seyferts and all sources, in order to show the differences in XLFs when 'inactive' galaxies such as HII and absorption line galaxies are included. We found an XLF power-law of -0.48 ± 0.12 and -0.24 ± 0.11 using all galaxies, for the entire and 'Complete' samples samples, respectively. In both the entire and 'Complete' samples samples, the inclusion of the 'inactive' galaxies increased the gradient of the XLF, which may suggest contamination from non-AGN objects, though we note that the power-law fit values are consistent with those found for all galaxies. Furthermore, our single power-law fits are consistent with previous *Chandra* studies of local galaxies She et al. 2017.

In terms of the empirical correlations between the X-ray luminosity and other diagnostics of SMBH activity, e.g., BH mass and [O iii] line luminosity, correlations were obtained for different optical AGN classes. We fitted the data including upper limits to the X-ray luminosity and black hole masses obtained from the $M - \sigma$ relation or dynamical mass measurements, finding an overall relationship for the entire sample to be $L_{\rm X-ray} \propto {\rm M}_{BH}^{0.78\pm0.07}$ with a scatter of 1.08 dex, and for the 'Complete' sample of $L_{\rm X-ray} \propto {\rm M}_{BH}^{0.62^{+0.11}_{-0.10}}$, with an scatter of 1.05 dex. No strong correlation was observed for Seyferts between the X-ray luminosity and BH mass, which may be due to the low number of Seyferts in this sample. The H ii galaxies, ALGs and LINERs follow similar correlations in the X-ray−BH mass plane. We also note that the detection fraction is much higher amongst higher mass objects (88 per cent for $M_{\rm BH} > 10^8 {\rm M}_{\odot}$) than in lower mass objects (50 per cent for $M_{\rm BH} < 10^6 {\rm M}_{\odot}$). By comparing the black hole masses to the Eddington luminosity, and assuming a bolometric correction factor of $30 \times {\rm L}_X$, we showed that the LINERs and ALGs all have very low Eddington ratios ($\lambda < 10^{-3}$). The Seyfert galaxies tend to have higher Eddington ratios but there are some notable exceptions at lower accretion rates. H ii galaxies can have a mixture of accretion rates, which may be due to their prevalence with lower mass nuclei, skewing their numbers to higher accretion rates artificially.

We also fitted the spectra of all the detected sources, using simple absorbed power-law models in most cases. We found that the best fit spectra indicated a preference for a photon index in the range 1.75−2.0, consistent with previous studies of brighter AGN. We therefore fixed the photon index to 1.8 for the faintest sources and re-fitted the spectra to ascertain the host galaxy absorption across the sample. We found that for 53 per cent of sources only upper limits to the host galaxy absorption were possible, and for those where reliable fits to the photon index were found, 70 per cent have absorbing column densities of less than the value through our Galaxy. As a final analysis with the spectra, we plotted the photon index as a function of the accretion rate. We found that the vast majority of sources in our sample with X-ray luminosities above 10^{39} erg s^{-1} followed the relationship for LLAGN proposed by Constantin et al. (2009), but we note that further observations are required for refinement of this analysis and to better probe the radio-quiet AGN relationship defined by Shemmer et al. (2006). This behaviour shows harder when brighter X-ray spectra for the low-luminosity AGNs we present here, with some notable exceptions of powerful AGNs, such as NGC 4051, NGC 4385 and NGC 5548.

A correlation is observed for all sources between the X-ray and [O iii] line luminosities, down to 10^{36} erg s^{-1}, lower than that probed in previous studies (Panessa et al. 2006; Hardcastle et al. 2009). When including upper limits, we find $L_{\rm X-ray} \propto {\rm L}_{\rm [O\,III]}^{1.22^{+0.11}_{-0.10}}$ for the entire sample and ${\rm L}_{\rm X-ray} \propto {\rm L}_{\rm [O\,III]}^{1.19^{+0.18}_{-0.17}}$ for the 'Complete' sample, but with significant scatter about the best fit lines. This correlation compares favourably with the correlations ~1:1 ratio between the X-rays and [O iii] line found in previous studies. However, we note that different AGN types follow slightly different tracks in the X-ray:[O iii] plane, with the LINERs showing the smallest scatter of all classes, suggesting a strong coupling between the two variables.

In conclusion, our sample provides the most statistically-complete and unbiased surveys of accretion in the nearby Universe performed to date, for both 'active' and 'inactive' galaxies. Further work is ongoing to characterise the off-nuclear X-ray sources, including their timing, spectral and multi-wavelength properties (Pahari et al. in prep) and future work will include establishing the fundamental plane of black hole activity with this data (Saikia et al. 2018b) with the wider LeMMINGs sample (Baldi et al. 2018) at sub-arcsecond resolution and the forthcoming 5 GHz equivalent LeMMINGs *e*-MERLIN study (Williams et al. in prep.).

DATA AVAILABILITY

All of the *Chandra* X-ray data presented here can be downloaded from the public heasarc archives, noted in the manuscript in Section 2. The values from the fitting procedures, fluxes, luminosities and spectra can be obtained from the online supplementary material.

ACKNOWLEDGEMENTS

We would like to acknowledge the support of the LeMMINGs project, upon which this study is based. We acknowledge funding from the Mayflower Scholarship from the University of Southampton afforded to David Williams to complete this work. This work was also supported by the Oxford Centre for Astrophysical Surveys, which is funded through generous support from the Hintze Family Charitable Foundation. MP acknowledges Royal Society-SERB Newton International Fellowship support funded jointly by the Royal Society, UK and the Science and Engineering Board of India (SERB) through Newton-Bhabha Fund. IMcH thanks the Royal Society for the award of a Royal Society Leverhulme Trust Senior Research Fellowship. RDB and IMcH also acknowledge the support of STFC under grant [ST/M001326/1]. SM gratefully acknowledges the support from the Chandra grant GO7-18080X issued by the Chandra X-ray Center, which is operated by the Smithsonian Astrophysical Observatory for and on behalf of the National Aeronautics Space Administration under contract NAS8-03060. A.B is grateful to the Royal Society and SERB (Science and Engineering Research Board, India). A.B. is supported by an INSPIRE Faculty grant (DST/INSPIRE/04/2018/001265) by the Department of Science and Technology, Govt. of India. P. G. B. acknowledges financial support from the STFC and the Czech Science Foundation project No. 19- 05599Y. S. A. gratefully acknowledges support from an ERC Adva. nced Grant 789410 J.H.K. acknowledges financial support from the European Union's Horizon 2020 research and innovation programme under Marie Skłodowska-Curie grant agreement No 721463 to the SUNDIAL ITN network, from the State Research Agency (AEI-MCINN) of the Spanish Ministry of Science and Innovation under the grant "The structure and evolution of galaxies and their central regions" with reference PID2019-105602GB-I00/10.13039/501100011033, and from IAC project P/300724, financed by the Ministry of Science and Innovation, through the State Budget and by the Canary Islands Department of Economy, Knowledge and Employment, through the Regional Budget of the Autonomous Community. B.T.D acknowledges support from a Spanish postdoctoral fellowship 'Ayudas 1265 para la atracción del talento investigador. Modalidad 2: jóvenes investigadores.' funded by Comunidad de Madrid under grant number 2016-T2/TIC-2039 and support from grant 'Ayudas para la realización de proyectos de I+D para jóvenes doctores 2019.' funded by Comunidad de Madrid and Universidad Complutense de Madrid under grant number PR65/19-22417. AA and MAPT acknowledge support from the Spanish MCIU through grant PGC2018-098915-B-C21. JM acknowledges support from the grant RTI2018-096228-B-C31 (MICIU/FEDER, EU). AA, MAPT and JM acknowledge financial support from the State Agency for Research of the Spanish MCIU through the "Center of Excellence Severo Ochoa" award to the Instituto de Astrofísica de Andalucía (SEV-2017-0709). CGM acknowledges support from Mrs Hiroko and Mr Jim Sherwin. FS acknowledges partial support from a Leverhulme Trust Research Fellowship. We also acknowledge Jodrell Bank Centre for Astrophysics, which is funded by the STFC. *e*-MERLIN and formerly, MERLIN, is a National Facility operated by the University of Manchester at Jodrell Bank Observatory on behalf of STFC. The scientific results reported in this article are based to a significant degree on observations made by the Chandra X-ray Observatory and on data obtained from the Chandra Data Archive. This research has made use of software provided by the Chandra X-ray Center (CXC) in the application package CIAO. DW would also like to thank Sam Connolly, Dimitrios Emmanoulopoulos and Sara Motta for useful discussions.

REFERENCES

Ajello M., Alexander D. M., Greiner J., Madejski G. M., Gehrels N., Burlon D., 2012, ApJ, 749, 21
Akylas A., Georgantopoulos I., 2009, A&A, 500, 999
Allen M. G., Groves B. A., Dopita M. A., Sutherland R. S., Kewley L. J., 2008, ApJS, 178, 20
Anderson T. W., Darling D. A., 1954, Journal of the American Statistical Association, 49, 765
Arnaud K. A., 1996, in Jacoby G. H., Barnes J., eds, Astronomical Society of the Pacific Conference Series Vol. 101, Astronomical Data Analysis Software and Systems V. p. 17
Baldi R. D., Capetti A., 2010, A&A, 519, A48
Baldi R. D., et al., 2018, MNRAS, 476, 3478
Baldi R. D., et al., 2021a, MNRAS, 500, 4749
Baldi R. D., et al., 2021b, MNRAS, 508, 2019
Baldwin J. A., Phillips M. M., Terlevich R., 1981, PASP, 93, 5
Ballantyne D. R., 2014, MNRAS, 437, 2845
Balmaverde B., Capetti A., 2006, A&A, 447, 97
Balmaverde B., Baldi R. D., Capetti A., 2008, A&A, 486, 119
Beswick R., Argo M. K., Evans R., McHardy I., Williams D. R. A., Westcott J., 2014, in Proceedings of the 12th European VLBI Network Symposium and Users Meeting (EVN 2014). 7-10 October 2014. Cagliari, Italy.. p. 10
Boorman P. G., Gandhi P., Baloković M., Brightman M., Harrison F., Ricci C., Stern D., 2018, MNRAS, 477, 3775
Brightman M., et al., 2017, doi:10.3847/1538-4357/aa75c9, 844, 10
Burlon D., Ajello M., Greiner J., Comastri A., Merloni A., Gehrels N., 2011, ApJ, 728, 58
Buttiglione S., Capetti A., Celotti A., Axon D. J., Chiaberge M., Macchetto F. D., Sparks W. B., 2010, A&A, 509, A6
Capetti A., Baldi R. D., 2011, A&A, 529, A126
Comastri A., 2004, Compton-Thick AGN: The Dark Side of the X-Ray Background. p. 245
Condon J. J., 1992, ARA&A, 30, 575
Connolly S. D., McHardy I. M., Skipper C. J., Emmanoulopoulos D., 2016, MNRAS, 459, 3963
Constantin A., Green P., Aldcroft T., Kim D.-W., Haggard D., Barkhouse W., Anderson S. F., 2009, ApJ, 705, 1336
Czerny B., Siemiginowska A., Janiuk A., Nikiel-Wroczyński B., Stawarz Ł., 2009, ApJ, 698, 840
Fabbiano G., 2006, ARA&A, 44, 323
Filho M. E., Barthel P. D., Ho L. C., 2006, A&A, 451, 71
Filippenko A. V., Sargent W. L. W., 1985, ApJS, 57, 503
Foreman-Mackey D., 2016, The Journal of Open Source Software, 24
Fotopoulou S., et al., 2016, A&A, 587, A142
Freeman P. E., Kashyap V., Rosner R., Lamb D. Q., 2002, ApJS, 138, 185
Gandhi P., et al., 2017, MNRAS, 467, 4606
Gehrels N., 1986, ApJ, 303, 336
Gilfanov M., Grimm H.-J., Sunyaev R., 2004, Nuclear Physics B Proceedings Supplements, 132, 369
González-Martín O., Masegosa J., Márquez I., Guerrero M. A., Dultzin-Hacyan D., 2006, A&A, 460, 45
González-Martín O., Masegosa J., Márquez I., Guainazzi M., Jiménez-Bailón E., 2009, A&A, 506, 1107
González-Martín O., et al., 2015, A&A, 578, A74
Graham A. W., Scott N., 2013, ApJ, 764, 151
Hardcastle M. J., Evans D. A., Croston J. H., 2009, MNRAS, 396, 1929
Heckman T. M., 1980, A&A, 87, 152
Hernández-García L., González-Martín O., Masegosa J., Márquez I., 2014, A&A, 569, A26
Hernández-García L., Masegosa J., González-Martín O., Márquez I., Perea J., 2016, ApJ, 824, 7
Ho L. C., 1999a, Advances in Space Research, 23, 813
Ho L. C., 1999b, ApJ, 516, 672
Ho L. C., 2008, ARA&A, 46, 475
Ho L. C., Ulvestad J. S., 2001, ApJS, 133, 77
Ho L. C., Filippenko A. V., Sargent W. L., 1995, ApJS, 98, 477
Ho L. C., Filippenko A. V., Sargent W. L. W., 1997a, ApJS, 112, 315
Ho L. C., Filippenko A. V., Sargent W. L. W., Peng C. Y., 1997b, ApJS, 112, 391
Ho L. C., Filippenko A. V., Sargent W. L. W., 1997c, ApJ, 487, 568
Ho L. C., Filippenko A. V., Sargent W. L. W., 1997d, ApJ, 487, 591
Ho L. C., et al., 2001, ApJ, 549, L51

Ho L. C., Filippenko A. V., Sargent W. L. W., 2003, ApJ, 583, 159
Ho L. C., Greene J. E., Filippenko A. V., Sargent W. L. W., 2009, ApJS, 183, 1
Ishibashi W., Courvoisier T. J.-L., 2010, A&A, 512, A58
Kaaret P., Feng H., Roberts T. P., 2017, ARA&A, 55, 303
Kalberla P. M. W., Burton W. B., Hartmann D., Arnal E. M., Bajaja E., Morras R., Pöppel W. G. L., 2005, A&A, 440, 775
Kammoun E. S., et al., 2019, ApJ, 877, 102
Kammoun E. S., et al., 2020, ApJ, 901, 161
Kaspi S., Smith P. S., Netzer H., Maoz D., Jannuzi B. T., Giveon U., 2000, ApJ, 533, 631
Kauffmann G., Heckman T. M., 2009, MNRAS, 397, 135
Kelly B. C., 2007, ApJ, 665, 1489
Kewley L. J., Groves B., Kauffmann G., Heckman T., 2006, MNRAS, 372, 961
King A. R., 2004, MNRAS, 347, L18
Koratkar A. P., Gaskell C. M., 1991, ApJ, 370, L61
Kormendy J., Ho L. C., 2013, ARA&A, 51, 511
LaMassa S. M., Yaqoob T., Boorman P. G., Tzanavaris P., Levenson N. A., Gandhi P., Ptak A. F., Heckman T. M., 2019, ApJ, 887, 173
Lightman A. P., White T. R., 1988, ApJ, 335, 57
Liu J., 2011, ApJS, 192, 10
Maoz D., 2007, MNRAS, 377, 1696
Marchesi S., Ajello M., Marcotulli L., Comastri A., Lanzuisi G., Vignali C., 2018, ApJ, 854, 49
Masini A., Comastri A., Hickox R. C., Koss M., Civano F., Brigthman M., Brusa M., Lanzuisi G., 2019, ApJ, 882, 83
Matt G., Fabian A. C., Guainazzi M., Iwasawa K., Bassani L., Malaguti G., 2000, MNRAS, 318, 173
Mattila S., et al., 2018, Science, 361, 482
Merloni A., Heinz S., di Matteo T., 2003, MNRAS, 345, 1057
Murphy K. D., Yaqoob T., 2009, MNRAS, 397, 1549
Muxlow T. W. B., et al., 2010, MNRAS, 404, L109
Nagao T., Murayama T., Shioya Y., Taniguchi Y., 2002, ApJ, 567, 73
Nandra K., Pounds K. A., 1994, MNRAS, 268, 405
Narayan R., Kato S., Honma F., 1997, ApJ, 476, 49
Narayan R., Mahadevan R., Quataert E., 1998, in Abramowicz M. A., Björnsson G., Pringle J. E., eds, Theory of Black Hole Accretion Disks. p. 148 (arXiv:astro-ph/9803141)
Netzer H., 2019, MNRAS, 488, 5185
Oskinova L. M., 2005, MNRAS, 361, 679
Panessa F., Bassani L., Cappi M., Dadina M., Barcons X., Carrera F. J., Ho L. C., Iwasawa K., 2006, A&A, 455, 173
Panessa F., Barcons X., Bassani L., Cappi M., Carrera F. J., Ho L. C., Pellegrini S., 2007, A&A, 467, 519
Pellegrini S., 2005, ApJ, 624, 155
Piconcelli E., Jimenez-Bailón E., Guainazzi M., Schartel N., Rodríguez-Pascual P. M., Santos-Lleó M., 2005, A&A, 432, 15
Ptak A., 2001, X-ray Astronomy: Stellar Endpoints, AGN, and the Diffuse X-ray Background, 599, 326
Reynolds C. S., 1997, MNRAS, 286, 513
Reynolds C. S., Young A. J., Begelman M. C., Fabian A. C., 1999, ApJ, 514, 164
Ricci C., Ueda Y., Koss M. J., Trakhtenbrot B., Bauer F. E., Gandhi P., 2015, ApJ, 815, L13
Roberts T. P., Warwick R. S., 2000, MNRAS, 315, 98
Saikia P., Körding E., Falcke H., 2015, MNRAS, 450, 2317
Saikia P., Körding E., Dibi S., 2018a, MNRAS, 477, 2119
Saikia P., Körding E., Coppejans D. L., Falcke H., Williams D., Baldi R. D., Mchardy I., Beswick R., 2018b, A&A, 616, A152
Sarzi M., et al., 2010, MNRAS, 402, 2187
Sazonov S., Krivonos R., Revnivtsev M., Churazov E., Sunyaev R., 2008, A&A, 482, 517
Schmidt M., 1968, ApJ, 151, 393
Seyfert C. K., 1941, PASP, 53, 231
Shakura N. I., Sunyaev R. A., 1973, A&A, 24, 337
Shankar F., et al., 2016, MNRAS, 460, 3119
Shankar F., et al., 2019, MNRAS, 485, 1278
She R., Ho L. C., Feng H., 2017, ApJ, 835, 223
Shemmer O., Brandt W. N., Netzer H., Maiolino R., Kaspi S., 2006, ApJ, 646, L29
Singh R., et al., 2013, A&A, 558, A43
Stephens M. A., 1974, Journal of the American Statistical Association, 69, 730
Swartz D. A., Tennant A. F., Soria R., 2009, ApJ, 703, 159
Swartz D. A., Soria R., Tennant A. F., Yukita M., 2011, ApJ, 741, 49
Tremaine S., et al., 2002, ApJ, 574, 740
Tueller J., Mushotzky R. F., Barthelmy S., Cannizzo J. K., Gehrels N., Markwardt C. B., Skinner G. K., Winter L. M., 2008, ApJ, 681, 113
Ueda Y., et al., 2011, PASJ, 63, S937
Ueda Y., Akiyama M., Hasinger G., Miyaji T., Watson M. G., 2014, ApJ, 786, 104
Weisskopf M. C., Tananbaum H. D., Van Speybroeck L. P., O'Dell S. L., 2000, in Truemper J. E., Aschenbach B., eds, Society of Photo-Optical Instrumentation Engineers (SPIE) Conference Series Vol. 4012, X-Ray Optics, Instruments, and Missions III. pp 2–16 (arXiv:astro-ph/0004127), doi:10.1117/12.391545
Zhang W. M., Soria R., Zhang S. N., Swartz D. A., Liu J. F., 2009, ApJ, 699, 281
van den Bosch R. C. E., 2016, ApJ, 831, 134

7 ONLINE SUPPLEMENTARY MATERIAL

Table 8: Basic properties of the X-ray sample presented in this paper. We show (1) the galaxy name; (2) Right Ascension in decimal degrees; (3) Declination in decimal degrees; (4) the Galactic Latitude (δ); (5) the distance in Mpc, which is obtained from (Ho et al. 1997a, and references therein); (6) the *Chandra* observation ID used for this analysis; (7) the exposure length in seconds; (8) denoted 'C' if part of the 'Complete' sample described in Section 2, denoted 'Y' if this is a new *Chandra* observation obtained in observing cycle 17 (programme ID 19708646 and 18620515, PI:McHardy), or denoted 'C+Y' if part of the 'Complete' sample and a new *Chandra* observation; (9) the detection significance where a source is observed or detected, 'Undet.' if the source is not detected in the observations or 'Not obs.' if there is no data in the *Chandra* archive; (10) a black hole mass measurement taken from the literature where possible (e.g., van den Bosch 2016), but where no dynamical measurements exist, we use the $M-\sigma$ relationship of Tremaine et al. (2002), using the stellar velocity dispersions of (Ho et al. 1997a); (11) a measurement of the [O III] line luminosity from (Baldi et al. 2018) or Baldi et al. (2021a), taken from the literature or (Ho et al. 1997a) in erg s^{-1}; (12) the new AGN classification given to the source based on the AGN re-classifcation scheme described in Baldi et al. (2018) and Baldi et al. (2021a); (13) a simplified version of the Hubble types originally shown in Ho et al. (1997a).

Galaxy Name (1)	Right Asc. (2)	Dec. δ (3)	Gal. Lat. $\lvert b\rvert$ (4)	Dist (Mpc) (5)	Obs. ID. (6)	Exposure (secs) (7)	Sample Status (8)	Det. Sig. (9)	Mass log($M_\odot$) (10)	$O_{[III]}$ log(Lum.) (11)	AGN Class (12)	Hubble Type (13)
NGC7817	0.995	20.75	−40.76	31.5	-	-	-	Not obs.	6.21 ± 0.22	39.29	HII	Spi.
IC10	5.096	59.29	3.34	1.3	8458	43571	-	Undet	5.11 ± 0.82	37.13	HII	Irr.
NGC147	8.299	48.51	−14.25	0.7	-	-	-	Not obs.	4.28 ± 0.40	-	ALG	Ell.
NGC185	9.739	48.34	−14.48	0.7	-	-	-	Not obs.	4.10 ± 0.21	34.63	LINER	Ell.
NGC205	10.092	41.69	−21.14	0.7	4691	9870	C	Undet	3.83 ± 1.84	-	ALG	Ell.
NGC221	10.674	40.87	−21.98	0.7	5690	113027	C	Undet	6.39 ± 0.19	-	ALG	Ell.
NGC224	10.685	41.27	−21.57	0.7	14196	42848	C	146.78	7.84 ± 0.05	-	ALG	Spi.
NGC266	12.449	32.28	−30.59	62.4	16013	84950	-	204.06	8.37 ± 0.07	39.43	LINER	Spi.
NGC278	13.018	47.55	−15.32	11.8	2055	38259	-	11.87	5.62 ± 0.33	37.47	HII	Spi.
NGC315	14.454	30.35	−32.50	65.8	4156	55016	-	33.96	8.92 ± 0.31	39.44	LINER	Ell.
NGC404	17.363	35.72	−27.01	2.4	12239	98257	-	89.63	5.65 ± 0.25	37.16	LINER	Len.
NGC410	17.746	33.15	−29.54	70.6	5897	2557	-	26.74	8.84 ± 0.04	<39.32	LINER	Ell.
NGC507	20.917	33.26	−29.13	65.7	16354	49426	-	58.35	8.88 ± 0.05	-	ALG	Len.
NGC598	23.463	30.66	−31.33	0.7	7728	44380	-	280.24	4.20 ± 0.25	<34.62	HII	Spi.
IC1727	26.875	27.33	33.90	8.2	1634	1725	-	Undet	7.47 ± 0.12	37.35	LINER	Spi.
NGC672	26.975	27.43	−33.78	7.5	10118	9859	-	Undet	<6.15	37.66	HII	Spi.
NGC697	27.823	22.36	−38.44	41.6	7090	2157	-	Undet	6.42 ± 0.21	37.85	HII	Spi.
NGC777	30.063	31.43	−29.19	66.5	7101	1930	-	Undet	8.97 ± 0.06	38.38	LINER	Ell.
NGC783	30.278	31.88	−28.70	68.1	-	-	-	Not obs.	6.94 ± 0.16	38.81	HII	Spi.
NGC784	30.321	28.84	−31.59	4.7	-	-	-	Not obs.	5.11 ± 0.82	37.68	HII	Spi.
NGC812	31.715	44.57	−16.26	108.8	-	-	-	Not obs.	7.25 ± 0.13	38.68	HII	Len.
NGC818	32.185	38.78	−21.66	59.4	-	-	-	Not obs.	7.64 ± 0.09	38.46	HII	Spi.
NGC841	32.822	37.50	−22.71	59.5	-	-	-	Not obs.	7.73 ± 0.09	38.74	LINER	Spi.
NGC890	35.504	33.27	−25.89	53.4	7124	3542	-	Undet	8.22 ± 0.07	-	ALG	Len.
NGC891	35.637	42.35	−17.42	9.6	5001	10038	-	14.23	6.37 ± 0.24	<36.29	HII	Spi.
NGC925	36.820	33.58	−25.17	9.4	19325	34602	-	6.76	<6.34	37.21	HII	Spi.
NGC959	38.101	35.49	−23.00	10.1	4613	118879	-	Undet	5.47 ± 0.82	37.40	HII	Spi.
NGC972	38.556	29.31	−28.43	21.4	-	-	-	Not obs.	6.97 ± 0.16	38.64	HII	Spi.
IC239	39.116	38.97	19.50	16.8	7131	4538	-	Undet	6.78 ± 0.20	<36.93	HII	Spi.
NGC1003	39.818	40.87	−17.55	10.7	7116	2672	-	Undet	-	37.23	HII	Spi.
NGC1023	40.100	39.06	−19.09	10.5	8198	49730	-	97.11	7.62 ± 0.05	-	ALG	Len.
NGC1058	40.876	37.34	−20.37	9.1	9579	19452	-	15.16	4.88 ± 0.34	35.95	LINER	Spi.
NGC1156	44.928	25.24	−29.19	6.4	7088	1930	-	Undet	5.13 ± 0.82	39.15	HII	Irr.
NGC1161	45.309	44.90	−12.13	25.9	12958	7446	-	14.7	8.58 ± 0.06	38.13	LINER	Len.
NGC1167	45.426	35.21	−20.49	65.3	19313	12880	-	25.17	8.27 ± 0.07	40.17	LINER	Len.
NGC1169	45.895	46.39	−10.63	33.7	-	-	-	Not obs.	7.96 ± 0.07	38.58	LINER	Spi.
NGC1186	46.379	42.84	−13.54	35.4	-	-	-	Not obs.	7.24 ± 0.14	38.95	HII	Spi.

Continued on next page

Table 8 – *Continued from previous page*

Galaxy Name (1)	Right Asc. (2)	Dec. δ (3)	Gal. Lat. $\|b\|$ (4)	Dist (Mpc) (5)	Obs. ID. (6)	Exposure (secs) (7)	Sample Status (8)	Det. Sig. (9)	Mass $\log(M_{\odot})$ (10)	$O_{[III]}$ log(Lum.) (11)	AGN Class (12)	Hubble Type (13)
NGC1275	49.951	41.51	−13.26	70.1	4952	164246	-	205.26	8.98 ± 0.20	41.61	LINER	Irr.
IC342	56.705	68.10	10.58	3.0	7069	57808	-	132.95	6.40 ± 0.27	35.99	HII	Spi.
IC356	61.944	69.81	13.11	18.1	-	-	-	Not obs.	7.70 ± 0.09	37.57	HII	Spi.
NGC1569	67.705	64.85	11.24	1.6	782	96795	-	Undet	5.49 ± 0.82	36.49	HII	Irr.
NGC1560	68.205	71.88	16.02	3.0	-	-	-	Not obs.	5.03 ± 0.82	37.38	HII	Spi.
NGC1961	85.523	69.38	19.47	53.1	10531	32835	-	32.74	8.29 ± 0.34	39.11	LINER	Spi.
NGC2146	94.657	78.36	24.90	17.2	3135	10019	-	8.84	7.33 ± 0.14	38.36	HII	Spi.
NGC2273	102.536	60.85	23.31	28.4	19377	9942	C+Y	84.06	6.93 ± 0.04	40.43	Seyfert	Spi.
NGC2342	107.326	20.64	13.04	69.5	-	-	-	Not obs.	7.60 ± 0.13	39.71	HII	Spi.
UGC3714	108.136	71.75	27.30	40.9	-	-	-	Not obs.	6.99 ± 0.16	38.49	HII	Spi.
NGC2268	108.579	84.38	27.55	34.4	-	-	-	Not obs.	7.55 ± 0.10	39.26	HII	Spi.
UGC3828	111.150	57.97	27.04	46.8	7104	2246	C+Y	Undet	6.39 ± 0.22	38.83	HII	Spi.
NGC2336	111.767	80.18	28.22	33.9	-	-	-	Not obs.	7.18 ± 0.10	38.20	LINER	Spi.
NGC2276	111.823	85.75	27.71	36.8	4968	45573	-	3.67	6.61 ± 0.20	38.17	HII	Spi.
NGC2366	112.216	69.21	28.53	2.9	-	-	-	Not obs.	-	-	HII	Irr.
IC467	112.577	79.87	28.38	27.4	-	-	-	Not obs.	6.15 ± 0.24	37.15	HII	Spi.
NGC2300	113.091	85.71	27.81	31.0	4968	45573	-	39.02	8.60 ± 0.04	-	ALG	Len.
NGC2403	114.211	65.60	29.19	4.2	4630	49936	-	151.93	6.26 ± 0.82	<35.91	HII	Spi.
UGC4028	117.708	74.36	30.04	52.7	-	-	-	Not obs.	6.54 ± 0.20	38.89	HII	Spi.
NGC2500	120.472	50.74	31.57	10.1	7112	2573	C	3.15	5.61 ± 0.82	36.55	HII	Spi.
NGC2543	123.241	36.25	31.31	32.9	-	-	-	Not obs.	7.12 ± 0.14	38.55	HII	Spi.
NGC2537	123.311	45.99	32.96	9.0	19359	9945	C+Y	Undet	6.11 ± 0.25	38.72	HII	Spi.
NGC2541	123.668	49.06	33.48	10.6	19354	7964	C+Y	3.21	5.81 ± 0.33	36.80	HII	Spi.
NGC2549	124.743	57.80	34.24	18.8	19339	9942	C+Y	15.18	7.16 ± 0.37	-	ALG	Irr.
NGC2639	130.909	50.21	38.19	42.6	5682	5021	C	40.84	7.94 ± 0.08	39.60	LINER	Spi.
NGC2634	132.106	73.97	33.94	30.2	13005	4909	-	Undet	7.96 ± 0.05	-	ALG	Ell.
NGC2683	133.174	33.42	38.76	5.7	11311	38530	-	58.89	7.38 ± 0.09	37.06	LINER	Spi.
NGC2681	133.386	51.31	39.68	13.3	2060	80898	C	160.3	7.07 ± 0.11	38.37	LINER	Len.
IC520	133.426	73.49	34.46	47.0	-	-	-	Not obs.	7.48 ± 0.09	39.04	LINER	Spi.
NGC2685	133.895	58.73	38.90	16.2	-	-	C	Not obs.	6.81 ± 0.09	38.41	LINER	Len.
NGC2655	133.907	78.22	32.69	24.4	-	-	-	Not obs.	7.74 ± 0.09	39.44	LINER	Len.
NGC2750	136.450	25.44	39.83	38.4	-	-	-	Not obs.	5.79 ± 0.32	39.20	HII	Spi.
NGC2742	136.890	60.48	39.96	22.2	19353	9780	C+Y	Undet	6.18 ± 0.77	37.73	HII	Spi.
NGC2715	137.026	78.09	33.32	20.4	-	-	-	Not obs.	6.63 ± 0.19	37.79	HII	Spi.
NGC2770	137.391	33.12	42.20	29.6	9104	17901	-	Undet	6.55 ± 0.19	37.56	HII	Spi.
NGC2768	137.906	60.04	40.56	23.7	9528	64607	C	85.01	7.96 ± 0.03	38.61	LINER	Ell.
NGC2776	138.061	44.95	43.25	38.7	19384	9939	C+Y	7.42	5.63 ± 0.31	38.32	HII	Spi.
NGC2748	138.430	76.48	34.36	23.8	11776	29670	-	8.58	7.65 ± 0.24	37.83	HII	Spi.
NGC2782	138.521	40.11	43.68	37.3	3014	29584	C	112.45	7.98 ± 0.09	39.99	HII	Spi.
NGC2787	139.827	69.20	38.05	13.0	4689	30848	-	147.73	7.61 ± 0.09	38.37	LINER	Len.
NGC2832	139.945	33.75	44.39	91.6	5904	3011	-	3.21	9.03 ± 0.04	<39.05	LINER	Ell.
NGC2841	140.508	50.98	44.15	12.0	6096	28217	C	54.21	8.31 ± 0.03	38.19	LINER	Spi.
NGC2859	141.077	34.51	45.40	25.4	-	-	-	Not obs.	8.02 ± 0.07	38.57	LINER	Len.
NGC2903	143.042	21.50	44.54	6.3	11260	93551	-	76.23	6.72 ± 0.08	37.35	HII	Spi.
NGC2950	145.647	58.85	44.66	23.3	19338	9939	C+Y	6.71	7.77 ± 0.08	-	ALG	Len.
NGC2964	145.726	31.85	49.02	21.9	-	-	-	Not obs.	7.08 ± 0.16	38.71	HII	Spi.
NGC2977	145.945	74.86	36.79	40.9	-	-	-	Not obs.	7.00 ± 0.16	38.20	HII	Spi.

Continued on next page

Table 8 – *Continued from previous page*

Galaxy Name (1)	Right Asc. (2)	Dec. δ (3)	Gal. Lat. $\|b\|$ (4)	Dist (Mpc) (5)	Obs. ID. (6)	Exposure (secs) (7)	Sample Status (8)	Det. Sig. (9)	Mass $\log(M_\odot)$ (10)	$O_{[III]}$ log(Lum.) (11)	AGN Class (12)	Hubble Type (13)
NGC2976	146.814	67.92	40.90	2.1	9542	9824	-	3.05	5.14 ± 0.81	36.58	HII	Spi.
NGC3003	147.150	33.42	50.34	24.4	-	-	-	Not obs.	5.49 ± 0.81	38.90	HII	Spi.
NGC2985	147.593	72.28	38.68	22.4	11669	13776	-	90.18	7.52 ± 0.06	38.69	LINER	Spi.
NGC3031	148.888	69.07	40.90	1.4	12301	78050	-	622.22	7.81 ± 0.13	37.72	LINER	Spi.
NGC3027	148.920	72.20	39.05	19.5	-	-	-	Not obs.	4.54 ± 0.62	37.69	HII	Spi.
NGC3034	148.967	69.68	40.57	5.2	10542	118614	-	110.07	7.37 ± 0.37	38.33	HII	Irr.
NGC3043	149.060	59.31	46.05	39.1	19365	9939	C+Y	Undet	5.77 ± 0.30	38.08	HII	Spi.
NGC3073	150.218	55.62	48.25	19.3	2038	26579	C	Undet	5.12 ± 0.43	38.02	HII	Len.
NGC3079	150.494	55.68	48.36	20.4	2038	26579	C	28.31	6.40 ± 0.05	37.67	LINER	Spi.
NGC3077	150.829	68.73	41.66	2.1	2076	53437	-	68.78	4.95 ± 0.82	37.15	HII	Irr.
NGC3162	153.382	22.74	54.08	22.2	-	-	-	Not obs.	6.72 ± 0.04	38.04	HII	Spi.
NGC3147	154.223	73.40	39.46	40.9	1615	2203	-	338.43	8.29 ± 0.07	39.53	LINER	Spi.
NGC3185	154.411	21.69	54.70	21.3	2760	19814	-	11.51	6.51 ± 0.20	39.44	Seyfert	Len.
NGC3190	154.524	21.83	54.85	22.4	2760	19814	-	68.72	8.02 ± 0.08	38.71	LINER	Spi.
NGC3184	154.571	41.42	55.64	8.7	804	42124	C	34.93	5.46 ± 0.36	37.31	HII	Spi.
NGC3193	154.604	21.89	54.93	23.2	11360	7149	-	8.66	8.08 ± 0.05	38.42	LINER	Ell.
NGC3198	154.978	45.55	54.83	10.8	9551	61625	C	30.81	5.57 ± 0.33	36.97	HII	Spi.
NGC3245	156.827	28.51	58.22	22.2	2926	9635	-	31.02	8.38 ± 0.11	38.70	HII	Len.
IC2574	157.090	68.41	43.61	3.4	792	10038	-	Undet	5.03 ± 0.82	35.55	HII	Spi.
NGC3254	157.333	29.49	58.75	23.6	-	-	-	Not obs.	7.21 ± 0.06	38.60	Seyfert	Spi.
NGC3294	159.068	37.32	59.84	26.7	-	-	-	Not obs.	5.92 ± 0.27	38.33	HII	Spi.
NGC3301	159.233	21.88	59.05	23.3	-	-	-	Not obs.	7.41 ± 0.10	<38.30	LINER	Len.
NGC3310	159.691	53.50	54.06	18.7	2939	47158	C	159.06	6.62 ± 0.02	38.43	HII	Spi.
NGC3319	159.790	41.69	59.34	11.5	19350	9939	C+Y	30.77	6.68 ± 0.18	37.07	HII	Spi.
NGC3344	160.880	24.92	61.25	6.1	15387	47442	-	42.61	6.38 ± 0.22	38.24	HII	Spi.
NGC3359	161.654	63.22	48.59	19.2	16347	49302	C	Undet	5.89 ± 0.28	37.36	HII	Spi.
NGC3348	161.792	72.84	41.35	37.8	-	-	-	Not obs.	8.42 ± 0.08	-	ALG	Ell.
NGC3395	162.459	32.98	63.14	27.4	2042	13478	-	13.8	6.86 ± 0.26	37.93	HII	Spi.
NGC3414	162.818	27.97	63.42	24.9	6779	13706	-	195.7	8.40 ± 0.07	39.06	LINER	Len.
NGC3430	163.048	32.95	63.64	26.7	16821	9926	-	Undet	5.72 ± 0.31	37.74	HII	Spi.
NGC3432	163.130	36.62	63.16	7.8	7091	1930	-	Undet	5.18 ± 0.82	38.00	HII	Spi.
NGC3448	163.662	54.31	55.45	24.5	19360	9973	C+Y	28.32	5.73 ± 0.82	39.48	HII	Irr.
NGC3486	165.100	28.97	65.49	7.4	393	1757	-	Undet	6.17 ± 0.08	37.93	Seyfert	Spi.
NGC3504	165.797	27.97	66.04	26.5	-	-	-	Not obs.	7.23 ± 0.15	39.88	HII	Spi.
NGC3516	166.698	72.57	42.40	38.9	2080	73062	-	1353.47	7.96 ± 0.05	40.80	Seyfert	Len.
NGC3556	167.880	55.68	56.25	14.1	2025	59366	C	83.27	6.52 ± 0.21	37.62	HII	Spi.
NGC3583	168.546	48.32	61.63	34.0	19381	9939	C+Y	6.34	7.40 ± 0.13	38.26	HII	Spi.
NGC3600	168.967	41.59	65.68	10.5	19356	6978	C+Y	36.78	5.70 ± 0.32	38.21	HII	Spi.
NGC3610	169.606	58.79	54.46	29.2	7141	4926	C	4.07	7.75 ± 0.05	-	ALG	Ell.
NGC3613	169.652	58.00	55.10	32.9	19320	9970	C	Undet	8.30 ± 0.07	-	ALG	Ell.
NGC3631	170.262	53.17	59.04	21.6	3951	89068	C	75.83	5.48 ± 0.34	37.53	HII	Spi.
NGC3646	170.430	20.17	68.35	56.8	-	-	-	Not obs.	7.66 ± 0.08	39.15	LINER	Irr.
NGC3642	170.574	59.07	54.53	27.5	19379	9780	C+Y	38.06	6.63 ± 0.16	38.96	LINER	Spi.
NGC3652	170.663	37.77	68.54	33.5	-	-	-	Not obs.	5.92 ± 0.26	38.51	HII	Spi.
NGC3665	171.182	38.76	68.49	32.4	3222	17958	-	20.66	8.76 ± 0.09	38.28	HII	Len.
NGC3675	171.533	43.59	66.19	12.8	19368	7967	C+Y	Undet	7.05 ± 0.06	37.78	LINER	Spi.
NGC3690	172.138	58.57	55.41	40.4	15077	51888	C	97.24	7.56 ± 0.14	39.98	HII	Irr.

Continued on next page

Table 8 – *Continued from previous page*

Galaxy Name (1)	Right Asc. (2)	Dec. δ (3)	Gal. Lat. $\|b\|$ (4)	Dist (Mpc) (5)	Obs. ID. (6)	Exposure (secs) (7)	Sample Status (8)	Det. Sig. (9)	Mass $\log(M_\odot)$ (10)	$O_{[III]}$ log(Lum.) (11)	AGN Class (12)	Hubble Type (13)
UGC6484	172.300	57.13	56.64	32.4	7111	2179	C+Y	Undet	6.06 ± 0.26	37.47	HII	Spi.
NGC3718	173.146	53.07	60.22	17.0	3993	4912	C	405.72	7.72 ± 0.11	37.41	LINER	Spi.
NGC3726	173.338	47.03	64.88	17.0	19346	9781	C+Y	Undet	5.38 ± 0.39	37.80	HII	Spi.
NGC3729	173.456	53.13	60.28	17.0	10356	7853	C	8.88	6.45 ± 0.21	36.60	HII	Spi.
NGC3738	173.952	54.52	59.32	4.3	19357	9343	C+Y	Undet	5.68 ± 0.32	37.77	HII	Irr.
NGC3735	173.989	70.54	45.28	41.0	-	-	-	Not obs.	7.51 ± 0.10	39.88	Seyfert	Spi.
NGC3756	174.200	54.29	59.59	23.5	19355	9936	C+Y	Undet	5.62 ± 0.31	37.04	HII	Spi.
NGC3780	174.844	56.27	58.12	37.2	19373	9936	C+Y	Undet	6.73 ± 0.18	37.43	LINER	Spi.
NGC3813	175.328	36.55	72.42	26.4	-	-	-	Not obs.	6.35 ± 0.22	37.59	HII	Spi.
NGC3838	176.057	57.95	56.99	24.6	19342	9936	C+Y	7.83	7.52 ± 0.09	-	ALG	Len.
NGC3877	176.533	47.49	65.96	17.0	1972	28723	C	11.58	6.66 ± 0.19	37.86	HII	Spi.
NGC3884	176.551	20.39	73.64	91.6	12999	4899	-	186.12	8.20 ± 0.07	40.20	LINER	Len.
NGC3893	177.160	48.71	65.23	17.0	21091	9945	C+Y	Undet	6.64 ± 0.18	37.44	HII	Spi.
NGC3900	177.290	27.02	76.14	29.4	-	-	-	Not obs.	7.50 ± 0.09	<38.35	ALG	Len.
NGC3898	177.314	56.08	58.96	21.9	4740	57443	C	52.8	8.19 ± 0.06	38.52	LINER	Spi.
NGC3917	177.690	51.82	62.79	17.0	19380	9780	C+Y	Undet	5.23 ± 0.39	36.90	LINER	Spi.
NGC3938	178.206	44.12	69.32	17.0	18456	45529	C	11.6	4.76 ± 0.29	37.61	HII	Spi.
NGC3941	178.231	36.99	74.19	18.9	-	-	-	Not obs.	7.42 ± 0.09	38.52	Seyfert	Len.
NGC3945	178.307	60.68	55.03	22.5	6780	13760	C	162.23	8.05 ± 0.07	38.38	LINER	Len.
NGC3949	178.425	47.86	66.41	17.0	16990	3391	C	Undet	6.57 ± 0.04	37.44	HII	Spi.
NGC3953	178.454	52.33	62.59	17.0	19367	10735	C+Y	7.27	7.33 ± 0.29	37.90	LINER	Spi.
NGC3963	178.746	58.49	57.12	42.7	19362	8869	C+Y	19.01	5.36 ± 0.37	38.09	HII	Spi.
NGC3982	179.118	55.12	60.27	17.0	4845	9204	C	27.6	6.37 ± 0.10	39.83	Seyfert	Spi.
NGC3992	179.400	53.38	61.92	17.0	19366	9939	C+Y	3.41	7.51 ± 0.28	37.10	LINER	Spi.
NGC3998	179.485	55.45	60.06	21.6	6781	13607	C	1817.56	8.93 ± 0.05	39.56	LINER	Len.
NGC4013	179.631	43.95	70.09	17.0	4739	79100	C	84.77	6.67 ± 0.17	37.37	LINER	Spi.
NGC4026	179.855	50.96	64.20	17.0	6782	13772	C	10.82	8.26 ± 0.12	-	LINER	Len.
NGC4036	180.361	61.90	54.25	24.6	6783	13723	C	54.81	7.89 ± 0.36	39.16	LINER	Len.
NGC4041	180.551	62.14	54.05	22.7	19383	9939	C+Y	5.86	6.83 ± 0.09	38.24	HII	Spi.
NGC4051	180.790	44.53	70.09	17.0	859	79769	C	1158.28	6.10 ± 0.25	40.18	Seyfert	Spi.
NGC4062	181.016	31.90	78.65	9.7	7106	2186	-	Undet	6.80 ± 0.14	36.51	HII	Spi.
NGC4088	181.390	50.54	65.01	17.0	14442	19806	C	12.55	6.46 ± 0.05	37.48	HII	Spi.
NGC4096	181.505	47.48	67.79	8.8	19345	7964	C+Y	3.55	6.52 ± 0.19	36.15	HII	Spi.
NGC4100	181.536	49.58	65.92	17.0	19347	9936	C+Y	Undet	6.43 ± 0.22	37.95	HII	Spi.
NGC4102	181.596	52.71	63.07	17.0	17117	28995	C	264.99	7.89 ± 0.10	39.10	HII	Spi.
NGC4111	181.763	43.07	71.70	17.0	1578	9340	C	62.38	7.60 ± 0.05	38.65	LINER	Len.
NGC4125	182.026	65.17	51.34	24.2	2071	64234	-	39.39	8.35 ± 0.06	38.71	LINER	Ell.
NGC4136	182.324	29.93	80.33	9.7	2921	19709	-	5.9	5.25 ± 0.40	37.39	HII	Spi.
NGC4138	182.374	43.69	71.40	17.0	17118	27779	C	416.37	7.25 ± 0.10	38.75	LINER	Len.
NGC4143	182.400	42.53	72.40	17.0	1617	2515	C	71.08	7.92 ± 0.36	38.81	LINER	Len.
NGC4144	182.494	46.46	69.01	4.1	16991	1051	C	Undet	<6.15	36.27	HII	Spi.
NGC4145	182.506	39.88	74.62	20.7	-	-	-	Not obs.	5.33 ± 0.46	36.80	HII	Spi.
NGC4151	182.636	39.41	75.06	20.3	9217	117122	-	2440.54	7.81 ± 0.08	41.74	Seyfert	Spi.
NGC4150	182.640	30.40	80.47	9.7	1638	1738	-	Undet	6.68 ± 0.06	35.83	LINER	Len.
NGC4157	182.767	50.48	65.41	17.0	11310	59256	C	22.85	6.74 ± 0.09	36.96	HII	Spi.
NGC4162	182.969	24.12	80.59	38.5	-	-	-	Not obs.	6.44 ± 0.20	38.44	HII	Spi.
NGC4169	183.078	29.18	81.14	50.4	-	-	-	Not obs.	7.97 ± 0.08	38.99	Seyfert	Len.

Continued on next page

Table 8 – *Continued from previous page*

Galaxy Name (1)	Right Asc. (2)	Dec. δ (3)	Gal. Lat. $\|b\|$ (4)	Dist (Mpc) (5)	Obs. ID. (6)	Exposure (secs) (7)	Sample Status (8)	Det. Sig. (9)	Mass $\log(M_\odot)$ (10)	$O_{[III]}$ log(Lum.) (11)	AGN Class (12)	Hubble Type (13)
NGC4183	183.320	43.70	71.73	17.0	16992	4111	C	Undet	5.06 ± 0.82	37.90	HII	Spi.
NGC4203	183.771	33.20	80.08	9.7	10535	41633	-	985.94	7.82 ± 0.26	38.28	LINER	Len.
NGC4214	183.913	36.33	78.07	3.5	4743	27209	-	Undet	5.76 ± 0.82	38.71	HII	Irr.
NGC4217	183.962	47.09	68.85	17.0	4738	72729	C	23.74	6.76 ± 0.08	36.93	HII	Spi.
NGC4220	184.049	47.88	68.13	17.0	19378	9663	C+Y	7.48	7.01 ± 0.12	36.19	LINER	Len.
NGC4236	184.174	69.47	47.36	2.2	9543	11014	-	Undet	<6.11	36.24	HII	Spi.
NGC4244	184.374	37.81	77.16	3.1	942	49215	-	Undet	5.17 ± 0.44	36.05	HII	Spi.
NGC4242	184.376	45.62	70.32	7.5	19351	9939	C+Y	Undet	-	<36.30	HII	Spi.
NGC4245	184.403	29.61	82.16	9.7	7107	2186	-	Undet	6.59 ± 0.18	37.36	HII	Len.
NGC4251	184.535	28.18	82.55	9.7	4695	10047	-	Undet	7.23 ± 0.07	-	ALG	Len.
NGC4258	184.740	47.30	68.84	6.8	1618	20944	C	405.77	7.58 ± 0.03	38.76	Seyfert	Spi.
NGC4274	184.961	29.61	82.62	9.7	7108	1907	-	Undet	6.86 ± 0.12	38.49	LINER	Spi.
NGC4278	185.028	29.28	82.77	9.7	7081	110726	-	575.27	7.96 ± 0.27	38.88	LINER	Ell.
NGC4291	185.074	75.37	41.60	29.4	11778	29782	-	16.24	8.99 ± 0.16	-	ALG	Ell.
NGC4314	185.633	29.90	83.08	9.7	2062	16073	-	6.5	7.19 ± 0.05	37.75	LINER	Spi.
NGC4346	185.867	46.99	69.39	17.0	19374	9942	C+Y	5.47	7.59 ± 0.08	37.88	LINER	Len.
NGC4369	186.151	39.38	76.53	21.6	-	-	-	Not obs.	6.34 ± 0.22	38.83	HII	Spi.
NGC4395	186.454	33.55	81.53	3.6	5302	28226	-	653.73	4.57 ± 0.34	38.35	Seyfert	Spi.
NGC4414	186.613	31.22	83.18	9.7	14796	9938	-	10.63	7.19 ± 0.06	36.46	LINER	Spi.
NGC4449	187.046	44.09	72.40	3.0	10875	59389	C	22.96	3.91 ± 0.89	38.28	HII	Irr.
NGC4448	187.064	28.62	84.67	9.7	7110	1990	-	Undet	7.24 ± 0.13	37.34	HII	Spi.
NGC4460	187.190	44.86	71.69	8.1	19363	10084	C+Y	Undet	5.31 ± 0.39	38.09	HII	Len.
NGC4485	187.630	41.70	74.81	9.3	4726	39632	C	377.8	5.78 ± 0.82	36.95	HII	Irr.
NGC4490	187.653	41.64	74.87	7.8	4726	39632	C	319.79	5.53 ± 0.35	37.12	HII	Spi.
NGC4494	187.850	25.77	85.32	9.7	2079	24841	-	123.47	7.57 ± 0.04	37.35	LINER	Ell.
NGC4559	188.991	27.96	86.47	9.7	2026	9376	-	21.08	5.68 ± 0.30	37.00	HII	Spi.
NGC4565	189.088	25.99	86.44	9.7	3950	59203	-	402.44	7.46 ± 0.08	38.22	Seyfert	Spi.
NGC4589	189.354	74.19	42.90	30.0	6785	13773	-	21.29	8.33 ± 0.04	38.78	LINER	Ell.
NGC4605	189.997	61.61	55.47	4.0	19344	9675	C+Y	3.05	4.57 ± 0.62	36.63	HII	Spi.
NGC4618	190.387	41.15	75.83	7.3	7147	9312	C	Undet	<5.86	37.97	HII	Spi.
NGC4648	190.435	74.42	42.69	27.5	11362	10906	-	7.65	8.33 ± 0.07	-	ALG	Ell.
NGC4631	190.532	32.54	84.22	6.9	797	59215	-	Undet	<6.34	37.12	HII	Spi.
NGC4656	190.990	32.17	84.70	7.2	-	-	-	Not obs.	6.31 ± 0.82	37.94	HII	Spi.
NGC4750	192.530	72.87	44.25	26.1	4020	4934	-	59.93	7.46 ± 0.09	38.76	LINER	Spi.
NGC4725	192.611	25.50	88.36	12.4	2976	24646	-	62.2	7.51 ± 0.04	38.52	Seyfert	Spi.
NGC4736	192.719	41.12	76.01	4.3	808	47369	C	241.51	7.12 ± 0.05	37.33	LINER	Spi.
NGC4800	193.657	46.53	70.59	15.2	19385	9939	C+Y	8.3	7.10 ± 0.06	37.62	HII	Spi.
NGC4793	193.670	28.94	88.05	38.9	-	-	-	Not obs.	4.61 ± 0.56	<38.84	HII	Spi.
NGC4826	194.183	21.68	84.42	4.1	9545	25958	-	34.25	6.85 ± 0.05	37.92	LINER	Spi.
NGC4914	195.179	37.32	79.63	62.4	18037	6268	-	Undet	8.33 ± 0.07	-	ALG	Ell.
NGC5005	197.734	37.06	79.25	21.3	19364	9942	-	74.58	8.27 ± 0.23	39.41	LINER	Spi.
NGC5012	197.904	22.92	83.78	40.4	-	-	-	Not obs.	7.52 ± 0.11	38.59	LINER	Spi.
NGC5033	198.365	36.59	79.45	18.7	19343	10140	-	1143.3	7.64 ± 0.05	39.34	LINER	Spi.
NGC5055	198.955	42.03	74.29	7.2	4021	4902	C	58	8.92 ± 0.10	37.43	LINER	Spi.
NGC5112	200.485	38.73	76.76	20.5	-	-	-	Not obs.	5.67 ± 0.32	37.42	HII	Spi.
NGC5204	202.402	58.42	58.01	4.8	13814	189851	C	Undet	5.32 ± 0.82	36.58	HII	Spi.
NGC5194	202.468	47.19	68.56	7.7	2197	27996	C	165.74	6.85 ± 0.16	38.91	Seyfert	Spi.

Continued on next page

Table 8 – *Continued from previous page*

Galaxy Name (1)	Right Asc. (2)	Dec. δ (3)	Gal. Lat. $\|b\|$ (4)	Dist (Mpc) (5)	Obs. ID. (6)	Exposure (secs) (7)	Sample Status (8)	Det. Sig. (9)	Mass $\log(M_\odot)$ (10)	$O_{[III]}$ log(Lum.) (11)	AGN Class (12)	Hubble Type (13)
NGC5195	202.497	47.27	68.49	9.3	2882	43632	C	45.28	7.31 ± 0.11	37.84	LINER	Irr.
NGC5273	205.535	35.65	76.25	21.3	13814	189851	-	46.83	6.61 ± 0.27	39.83	Seyfert	Len.
NGC5297	206.599	43.87	69.93	37.8	3933	46230	C+Y	Undet	6.07 ± 0.26	38.23	LINER	Spi.
NGC5308	206.752	60.97	54.88	32.4	415	1734	C+Y	4.97	8.51 ± 0.07	-	ALG	Len.
NGC5322	207.313	60.19	55.49	31.6	19370	9945	C	21.35	8.39 ± 0.03	38.20	LINER	Ell.
NGC5354	208.361	40.30	71.62	32.8	6787	13767	C	20.07	8.28 ± 0.05	38.61	LINER	Len.
NGC5353	208.361	40.28	71.63	37.8	19341	9939	C	20.07	8.76 ± 0.03	38.74	LINER	Len.
NGC5371	208.917	40.46	71.20	37.8	14903	40269	C	3.95	7.94 ± 0.08	39.04	LINER	Spi.
NGC5377	209.069	47.24	66.21	31.0	14903	40269	C+Y	6.22	7.84 ± 0.09	38.81	LINER	Spi.
NGC5383	209.271	41.85	70.08	37.8	13006	5392	C+Y	Undet	6.86 ± 0.16	38.06	HII	Spi.
NGC5395	209.658	37.42	72.50	46.7	19372	9939	-	29.73	7.57 ± 0.10	38.66	LINER	Spi.
NGC5448	210.709	49.17	64.01	32.6	13007	4902	C+Y	13.2	7.30 ± 0.11	38.55	LINER	Spi.
NGC5457	210.802	54.35	59.77	5.4	10395	15654	C	97.3	4.40 ± 0.64	36.99	HII	Spi.
NGC5473	211.180	54.89	59.20	33.0	19322	9821	C	3.37	8.30 ± 0.07	-	ALG	Len.
NGC5474	211.256	53.66	60.19	6.0	19371	9936	C	88.09	4.76 ± 0.52	37.35	HII	Spi.
NGC5485	211.797	55.00	58.91	32.8	4736	77353	C+Y	7.28	8.19 ± 0.07	38.31	LINER	Len.
NGC5523	213.718	25.32	71.22	21.5	-	-	-	Not obs.	4.82 ± 0.50	37.24	HII	Spi.
NGC5548	214.498	25.14	70.50	67.0	9546	29788	-	1886	7.70 ± 0.13	41.60	Seyfert	Len.
NGC5557	214.607	36.49	69.35	42.6	19375	9939	-	Undet	8.81 ± 0.06	-	ALG	Ell.
NGC5585	214.951	56.73	56.47	7.0	3046	151411	C+Y	Undet	5.41 ± 0.17	37.68	HII	Spi.
NGC5631	216.639	56.58	56.01	32.7	19324	8838	C+Y	8.37	7.83 ± 0.09	38.76	LINER	Len.
NGC5660	217.457	49.62	60.64	37.2	7150	5318	C+Y	Undet	6.05 ± 0.27	38.10	HII	Spi.
NGC5656	217.606	35.32	67.38	42.6	-	-	-	Not obs.	7.19 ± 0.13	37.99	LINER	Spi.
NGC5678	218.023	57.92	54.50	35.6	19361	9942	C+Y	Undet	7.42 ± 0.13	38.27	HII	Spi.
NGC5676	218.197	49.46	60.39	34.5	19376	9939	C+Y	7.55	7.19 ± 0.13	37.95	HII	Spi.
NGC5866	226.623	55.76	52.49	15.3	19352	9939	C	9.67	7.84 ± 0.08	37.50	LINER	Len.
NGC5879	227.445	57.00	51.40	16.8	4022	4733	C	28.58	6.39 ± 0.21	37.89	LINER	Spi.
NGC5905	228.847	55.52	51.59	44.4	2879	33737	C	20.45	7.89 ± 0.09	39.02	HII	Spi.
NGC5907	228.974	56.33	51.09	14.9	2241	88988	C	9.74	7.24 ± 0.10	36.89	HII	Spi.
NGC5982	234.666	59.36	46.92	38.7	20830	51271	C	18.77	8.44 ± 0.04	<38.54	ALG	Ell.
NGC5985	234.903	59.33	46.83	39.2	786	46262	C+Y	50.78	7.71 ± 0.08	38.76	LINER	Spi.
NGC6015	237.855	62.31	44.12	17.5	20069	22751	C+Y	5.01	5.47 ± 0.35	37.19	HII	Spi.
NGC6140	245.242	65.39	39.85	18.6	-	-	-	Not obs.	5.69 ± 0.31	37.52	HII	Spi.
NGC6217	248.163	78.20	33.36	23.9	-	-	-	Not obs.	6.30 ± 0.25	39.25	HII	Spi.
NGC6207	250.766	36.83	40.68	17.4	-	-	-	Not obs.	6.78 ± 0.19	38.30	HII	Spi.
NGC6236	251.143	70.78	35.77	23.3	-	-	-	Not obs.	5.57 ± 0.82	37.93	HII	Spi.
NGC6340	257.605	72.30	33.36	22.0	-	-	-	Not obs.	7.56 ± 0.07	38.31	LINER	Len.
NGC6412	262.404	75.70	31.24	23.5	-	-	-	Not obs.	5.71 ± 0.31	37.59	HII	Spi.
NGC6503	267.360	70.14	30.64	6.1	19349	9942	-	6.45	5.56 ± 0.11	-	LINER	Spi.
NGC6482	267.954	23.07	22.91	52.3	19369	9935	-	72.15	8.90 ± 0.06	-	LINER	Ell.
NGC6643	274.943	74.57	28.17	25.5	3218	19350	-	3.28	6.84 ± 0.17	37.52	HII	Spi.
NGC6654	276.033	73.18	27.85	29.5	-	-	-	Not obs.	7.87 ± 0.08	-	ALG	Len.
NGC6689	278.708	70.52	26.83	12.2	872	13190	-	Undet	4.57 ± 0.74	37.17	LINER	Spi.
NGC6702	281.740	45.71	19.79	62.8	-	-	-	Not obs.	7.88 ± 0.05	-	ALG	Ell.
NGC6703	281.829	45.55	19.68	35.9	-	-	-	Not obs.	7.95 ± 0.04	38.46	LINER	Len.
NGC6946	308.714	60.16	11.67	5.5	7123	3478	-	Undet	5.90 ± 0.29	37.03	HII	Spi.
NGC6951	309.310	66.11	14.85	24.1	-	-	-	Not obs.	7.35 ± 0.12	38.69	LINER	Spi.

Continued on next page

Table 8 – *Continued from previous page*

Galaxy Name (1)	Right Asc. (2)	Dec. δ (3)	Gal. Lat. $\|b\|$ (4)	Dist (Mpc) (5)	Obs. ID. (6)	Exposure (secs) (7)	Sample Status (8)	Det. Sig. (9)	Mass $\log(M_\odot)$ (10)	$O_{[III]}$ log(Lum.) (11)	AGN Class (12)	Hubble Type (13)
NGC7080	322.509	26.72	−17.59	64.1	-	-	-	Not obs.	6.84 ± 0.17	-	HII	Spi.
NGC7217	331.969	31.36	−19.71	16.0	-	-	-	Not obs.	7.52 ± 0.09	38.31	LINER	Spi.
NGC7331	339.268	34.42	−20.72	14.3	1043	58290	-	26.87	8.02 ± 0.18	38.30	LINER	Spi.
NGC7332	339.352	23.80	−29.67	18.2	-	-	-	Not obs.	7.08 ± 0.18	-	ALG	Len.
NGC7457	345.250	30.14	−26.94	12.3	15046	14778	-	Undet	6.95 ± 0.30	-	ALG	Len.
NGC7640	350.527	40.85	−18.94	8.6	2198	29462	-	8.38	5.64 ± 0.82	36.83	HII	Spi.
NGC7741	355.978	26.08	−34.37	12.3	11786	28672	-	Undet	4.78 ± 0.53	37.90	HII	Spi.
NGC7798	359.857	20.75	−40.49	32.6	-	-	-	Not obs.	6.42 ± 0.21	38.65	HII	Spi.

Table 9: Table showing flux and luminosity measurements obtained from X-ray spectral fitting (see Section 3 for the sources that have been observed in the *Chandra* archive. The full table can be found in the online supplementary material. All fluxes in this table are calculated using the CFLUX command in XSpec. In the table we show (1) the galaxy name; (2) the detection significance if detected, else a "<" denotes a non detected source where the flux and luminosity measurements given in the 0.3–10 keV band are 3σ upper limits; (3) The logarithm of the flux in the 0.3–10.0 keV band; (4) The logarithm of the flux in the 0.3–2.0 keV band; (5) The logarithm of the flux in the 2.0–10.0 keV band; (6) The logarithm of the X-ray luminosity in the 0.3–10.0 keV band; (7) The logarithm of the X-ray luminosity in the 0.3–2.0 keV band; (8) The logarithm of the X-ray luminosity in the 2.0–10.0 keV band. All uncertainties are shown at the 1 σ level. All fluxes are measured in erg s^{-1} cm^{-2} and all luminosities are measured in erg s^{-1}.

Galaxy Name	Detection Signif.	log Flux 0.3–10 keV erg s^{-1} cm^{-2}	log Flux 0.3–2 keV erg s^{-1} cm^{-2}	log Flux 2–10 keV erg s^{-1} cm^{-2}	log Lum. 0.3–10 keV erg s^{-1}	log Lum. 0.3–2 keV erg s^{-1}	log Lum. 2–10 keV erg s^{-1}
(1)	(2)	(3)	(4)	(5)	(6)	(7)	(8)
IC 10	<	-13.92	-	-	36.38	-	-
NGC 205	<	-14.00	-	-	35.77	-	-
NGC 221	<	-14.24	-	-	35.53	-	-
NGC 224	146.78	-12.59±0.05	-12.77±0.10	-13.04±0.10	37.18±0.05	37.00±0.10	36.73±0.10
NGC 266	204.06	-12.81±0.06	-13.28±0.10	-12.99±0.10	40.86±0.06	40.39±0.10	40.68±0.10
NGC 278	11.87	-14.18±0.10	-14.29±0.11	-14.80±0.20	38.05±0.10	37.93±0.11	37.42±0.20
NGC 315	33.96	-11.86±0.03	-12.58±0.04	-11.95±0.04	41.86±0.03	41.13±0.04	41.77±0.04
NGC 404	89.63	-13.53±0.07	-13.71±0.16	-14.00±0.16	37.31±0.07	37.13±0.16	36.84±0.16
NGC 410	26.74	-12.21±0.06	-12.35±0.03	-12.77±0.28	41.57±0.06	41.43±0.03	41.00±0.28
NGC 507	58.35	-12.95±0.02	-12.98±0.02	-14.08±0.02	40.76±0.02	40.73±0.02	39.63±0.02
NGC 598	280.24	-13.51±0.12	-13.58±0.33	-14.32±0.33	36.26±0.12	36.18±0.33	35.44±0.33
IC 1727	<	-14.02	-	-	37.88	-	-
NGC 672	<	-13.39	-	-	38.43	-	-
NGC 697	<	-12.37	-	-	40.95	-	-
NGC 777	<	-12.95	-	-	40.77	-	-
NGC 890	<	-13.34	-	-	40.19	-	-
NGC 891	14.23	-13.13±0.04	-14.00±0.03	-13.19±0.04	38.91±0.04	38.04±0.03	38.85±0.04
NGC 925	6.76	-13.84±0.27	-14.29±0.41	-14.04±0.41	38.18±0.27	37.74±0.41	37.98±0.41
NGC 959	<	-14.04	-	-	38.04	-	-
IC 239	<	-14.37	-	-	38.15	-	-
NGC 1003	<	-14.06	-	-	38.08	-	-
NGC 1023	97.11	-13.07±0.08	-13.42±0.14	-13.33±0.14	39.05±0.08	38.70±0.14	38.79±0.14
NGC 1058	15.16	-13.65±0.20	-13.71±0.19	-14.53±0.19	38.35±0.20	38.29±0.19	37.47±0.19
NGC 1156	<	-14.00	-	-	37.69	-	-
NGC 1161	14.7	-12.88±0.06	-13.25±0.07	-13.11±0.08	40.02±0.06	39.66±0.07	39.79±0.08
NGC 1167	25.17	-13.25±0.21	-13.53±0.45	-13.59±0.45	40.45±0.21	40.18±0.45	40.12±0.45
NGC 1275	205.26	-11.40±0.02	-12.51±0.02	-11.43±0.02	42.37±0.02	41.26±0.02	42.34±0.02
IC 342	132.95	-12.61±0.05	-12.90±0.09	-12.91±0.09	38.43±0.05	38.13±0.09	38.12±0.09
NGC 1569	<	-14.87	-	-	35.62	-	-
NGC 1961	32.74	-13.10±0.15	-13.63±0.22	-13.25±0.22	40.43±0.15	39.90±0.22	40.27±0.22
NGC 2146	8.84	-12.17±0.29	-13.81±0.30	-12.18±0.30	40.38±0.29	38.74±0.30	40.37±0.30
NGC 2273	84.06	-12.08±0.16	-13.56±0.17	-12.10±0.17	40.90±0.16	39.43±0.17	40.89±0.17
UGC 3828	<	-12.13	-	-	41.29	-	-
NGC 2276	3.67	-13.77±0.14	-13.88±0.34	-14.43±0.34	39.44±0.14	39.33±0.34	38.78±0.34
NGC 2300	39.02	-12.93±0.10	-12.94±0.10	-14.41±0.19	40.14±0.10	40.12±0.10	38.65±0.19
NGC 2403	151.93	-12.75±0.05	-13.11±0.03	-12.99±0.08	38.58±0.05	38.21±0.03	38.34±0.08
NGC 2500	3.15	-13.66±0.22	-13.91±0.22	-13.99±0.22	38.43±0.22	38.18±0.22	38.10±0.22
NGC 2537	<	-12.40	-	-	39.58	-	-
NGC 2541	3.21	-14.03±0.67	-14.43±0.67	-14.25±0.67	38.10±0.67	37.70±0.67	37.87±0.67

Continued on next page

Table 9 – continued from previous page

Galaxy Name	Detection Signif.	log Flux 0.3–10 keV erg s^{-1} cm^{-2}	log Flux 0.3–2 keV erg s^{-1} cm^{-2}	log Flux 2–10 keV erg s^{-1} cm^{-2}	log Lum. 0.3–10 keV erg s^{-1}	log Lum. 0.3–2 keV erg s^{-1}	log Lum. 2–10 keV erg s^{-1}
(1)	(2)	(3)	(4)	(5)	(6)	(7)	(8)
NGC 2549	15.18	-13.11±0.29	-13.84±0.35	-13.19±0.35	39.52±0.29	38.78±0.35	39.43±0.35
NGC 2639	40.84	-12.28±0.22	-12.30±0.32	-13.61±0.32	41.05±0.22	41.03±0.32	39.72±0.32
NGC 2634	<	-13.43	-	-	39.61	-	-
NGC 2683	58.89	-12.20±0.04	-13.96±0.18	-12.21±0.04	39.39±0.04	37.63±0.18	39.38±0.04
NGC 2681	160.3	-13.11±0.06	-13.34±0.12	-13.49±0.12	39.22±0.06	38.98±0.12	38.84±0.12
NGC 2742	<	-14.52	-	-	38.25	-	-
NGC 2770	<	-14.68	-	-	38.34	-	-
NGC 2768	85.01	-13.00±0.12	-13.67±0.15	-13.10±0.15	39.83±0.12	39.16±0.15	39.73±0.15
NGC 2776	7.42	-14.14±0.20	-14.20±0.20	-15.02±0.20	39.11±0.20	39.05±0.20	38.23±0.20
NGC 2748	8.58	-14.42±0.20	-14.80±0.18	-14.66±0.25	38.41±0.20	38.03±0.18	38.18±0.25
NGC 2782	112.45	-12.43±0.02	-13.14±0.02	-12.53±0.02	40.79±0.02	40.08±0.02	40.69±0.02
NGC 2787	147.73	-12.87±0.11	-13.23±0.17	-13.11±0.17	39.44±0.11	39.08±0.17	39.20±0.17
NGC 2832	3.21	-12.22±0.08	-12.31±0.09	-12.95±0.18	41.78±0.08	41.69±0.09	41.06±0.18
NGC 2841	54.21	-13.04±0.05	-13.38±0.03	-13.30±0.10	39.20±0.05	38.86±0.03	38.94±0.10
NGC 2903	76.23	-12.99±0.02	-13.32±0.02	-13.27±0.04	38.68±0.02	38.36±0.02	38.40±0.04
NGC 2950	6.71	-13.55±0.30	-13.62±0.28	-14.38±0.28	39.26±0.30	39.19±0.28	38.44±0.28
NGC 2976	3.05	-14.23±0.40	-14.29±0.38	-15.11±0.38	36.49±0.40	36.43±0.38	35.61±0.38
NGC 2985	90.18	-12.97±0.14	-13.24±0.28	-13.30±0.28	39.81±0.14	39.54±0.28	39.48±0.28
NGC 3031	622.22	-11.16±0.01	-12.01±0.01	-11.22±0.01	39.21±0.01	38.36±0.01	39.15±0.01
NGC 3034	110.07	-12.26±0.01	-12.80±0.01	-12.41±0.02	39.25±0.01	38.71±0.01	39.10±0.02
NGC 3043	<	-14.53	-	-	38.74	-	-
NGC 3073	<	-14.23	-	-	38.42	-	-
NGC 3079	28.31	-12.60±0.14	-13.53±0.16	-12.65±0.16	40.10±0.14	39.17±0.16	40.05±0.16
NGC 3077	68.78	-13.09±0.03	-14.03±0.05	-13.15±0.04	37.63±0.03	36.69±0.05	37.58±0.04
NGC 3147	338.43	-11.24±0.07	-11.81±0.09	-11.38±0.09	42.06±0.07	41.49±0.09	41.92±0.09
NGC 3185	11.51	-12.80±0.24	-13.70±0.08	-12.85±0.33	39.93±0.24	39.03±0.08	39.89±0.33
NGC 3190	68.72	-12.52±0.06	-12.96±0.07	-12.71±0.10	40.26±0.06	39.81±0.07	40.07±0.10
NGC 3184	34.93	-13.49±0.21	-13.93±0.29	-13.69±0.29	38.47±0.21	38.03±0.29	38.27±0.29
NGC 3193	8.66	-13.23±0.23	-13.30±0.21	-14.04±0.21	39.58±0.23	39.51±0.21	38.76±0.21
NGC 3198	30.81	-13.48±0.24	-14.24±0.28	-13.57±0.28	38.66±0.24	37.91±0.28	38.58±0.28
NGC 3245	31.02	-13.05±0.17	-13.38±0.27	-13.32±0.27	39.72±0.17	39.39±0.27	39.45±0.27
IC 2574	<	-14.59	-	-	36.55	-	-
NGC 3310	159.06	-12.47±0.09	-13.21±0.11	-12.56±0.11	40.15±0.09	39.41±0.11	40.06±0.11
NGC 3319	30.77	-12.88±0.31	-13.39±0.47	-13.04±0.47	39.32±0.31	38.81±0.47	39.16±0.47
NGC 3344	42.61	-13.18±0.05	-13.50±0.07	-13.46±0.11	38.47±0.05	38.15±0.07	38.19±0.11
NGC 3359	<	-14.76	-	-	37.88	-	-
NGC 3395	13.8	-13.24±0.13	-13.39±0.05	-13.74±0.50	39.72±0.13	39.56±0.05	39.21±0.50
NGC 3414	195.7	-12.25±0.09	-12.79±0.13	-12.39±0.13	40.62±0.09	40.08±0.13	40.48±0.13
NGC 3430	<	-14.24	-	-	38.69	-	-
NGC 3432	<	-13.96	-	-	37.90	-	-
NGC 3448	28.32	-12.93±0.09	-13.81±0.08	-12.99±0.10	39.93±0.09	39.05±0.08	39.87±0.10
NGC 3486	<	-14.31	-	-	37.50	-	-
NGC 3516	1353.47	-10.72±0.02	-11.71±0.02	-10.77±0.02	42.53±0.02	41.55±0.02	42.49±0.02
NGC 3556	83.27	-13.09±0.12	-13.74±0.15	-13.19±0.15	39.29±0.12	38.63±0.15	39.18±0.15
NGC 3583	6.34	-13.40±0.24	-13.65±0.46	-13.76±0.46	39.74±0.24	39.50±0.46	39.38±0.46
NGC 3600	36.78	-12.80±0.21	-13.27±0.33	-12.98±0.33	39.32±0.21	38.85±0.33	39.14±0.33

Continued on next page

Table 9 – continued from previous page

Galaxy Name	Detection Signif.	log Flux 0.3–10 keV erg s^{-1} cm^{-2}	log Flux 0.3–2 keV erg s^{-1} cm^{-2}	log Flux 2–10 keV erg s^{-1} cm^{-2}	log Lum. 0.3–10 keV erg s^{-1}	log Lum. 0.3–2 keV erg s^{-1}	log Lum. 2–10 keV erg s^{-1}
(1)	(2)	(3)	(4)	(5)	(6)	(7)	(8)
NGC 3610	4.07	-13.44±0.22	-13.50±0.21	-14.32±0.21	39.57±0.22	39.51±0.21	38.69±0.21
NGC 3613	<	-14.50	-	-	38.61	-	-
NGC 3631	75.83	-13.29±0.11	-13.65±0.19	-13.54±0.19	39.46±0.11	39.09±0.19	39.21±0.19
NGC 3642	38.06	-12.77±0.28	-12.83±0.37	-13.64±0.37	40.19±0.28	40.12±0.37	39.32±0.37
NGC 3665	20.66	-13.12±0.32	-13.84±0.39	-13.21±0.39	39.98±0.32	39.26±0.39	39.89±0.39
NGC 3675	<	-13.90	-	-	38.39	-	-
NGC 3690	97.24	-12.29±0.06	-13.03±0.08	-12.38±0.08	41.00±0.06	40.26±0.08	40.91±0.08
UGC 6484	<	-14.77	-	-	38.33	-	-
NGC 3718	405.72	-11.28±0.09	-12.32±0.10	-11.32±0.10	41.26±0.09	40.22±0.10	41.22±0.10
NGC 3726	<	-14.33	-	-	38.21	-	-
NGC 3729	8.88	-12.73±0.09	-13.34±0.09	-12.85±0.09	39.81±0.09	39.20±0.09	39.69±0.09
NGC 3738	<	-14.49	-	-	36.85	-	-
NGC 3756	<	-14.35	-	-	38.47	-	-
NGC 3780	<	-14.35	-	-	38.87	-	-
NGC 3838	7.83	-13.57±0.29	-13.63±0.28	-14.45±0.28	39.29±0.29	39.23±0.28	38.41±0.28
NGC 3877	11.58	-13.38±0.47	-13.38±0.60	-15.42±0.59	39.16±0.47	39.16±0.60	37.12±0.59
NGC 3884	186.12	-11.91±0.09	-12.40±0.14	-12.08±0.14	42.09±0.09	41.60±0.14	41.92±0.14
NGC 3893	<	-14.35	-	-	38.19	-	-
NGC 3898	52.8	-13.37±0.08	-13.55±0.17	-13.83±0.17	39.39±0.08	39.21±0.17	38.93±0.17
NGC 3917	<	-14.19	-	-	38.35	-	-
NGC 3938	11.6	-14.36±0.50	-14.42±0.48	-15.24±0.48	38.18±0.50	38.12±0.48	37.30±0.48
NGC 3945	162.23	-12.61±0.08	-12.84±0.16	-12.99±0.16	40.18±0.08	39.94±0.16	39.80±0.16
NGC 3949	<	-13.48	-	-	39.05	-	-
NGC 3953	7.27	-13.62±0.31	-13.68±0.30	-14.50±0.30	38.92±0.31	38.85±0.30	38.04±0.30
NGC 3963	19.01	-13.05±0.14	-13.65±0.13	-13.18±0.21	40.29±0.14	39.69±0.13	40.16±0.21
NGC 3982	27.6	-13.31±0.08	-13.34±0.10	-14.47±0.22	39.23±0.08	39.19±0.10	38.07±0.22
NGC 3992	3.41	-13.56±0.27	-14.14±0.36	-13.70±0.35	38.98±0.27	38.40±0.36	38.84±0.35
NGC 3998	1817.56	-10.79±0.02	-11.34±0.02	-10.93±0.02	41.96±0.02	41.41±0.02	41.82±0.02
NGC 4013	84.77	-13.71±0.46	-14.78±0.49	-13.74±0.49	38.83±0.46	37.76±0.49	38.80±0.49
NGC 4026	10.82	-13.63±0.23	-13.87±0.39	-14.00±0.39	38.91±0.23	38.67±0.39	38.54±0.39
NGC 4036	54.81	-12.48±0.06	-12.95±0.14	-12.65±0.08	40.38±0.06	39.91±0.14	40.21±0.08
NGC 4041	5.86	-13.38±0.24	-13.61±0.44	-13.76±0.44	39.41±0.24	39.18±0.44	39.03±0.44
NGC 4051	1158.28	-10.72±0.01	-11.29±0.01	-10.86±0.01	41.81±0.01	41.25±0.01	41.68±0.01
NGC 4062	<	-14.05	-	-	38.00	-	-
NGC 4088	12.55	-13.20±0.41	-14.13±0.46	-13.25±0.46	39.34±0.41	38.41±0.46	39.29±0.46
NGC 4096	3.55	-13.85±0.29	-14.32±0.29	-14.03±0.29	38.12±0.29	37.65±0.29	37.93±0.29
NGC 4100	<	-14.53	-	-	38.01	-	-
NGC 4102	264.99	-11.71±0.03	-12.70±0.02	-11.76±0.03	40.83±0.03	39.84±0.02	40.78±0.03
NGC 4111	62.38	-12.52±0.02	-12.78±0.02	-12.86±0.02	40.02±0.02	39.76±0.02	39.68±0.02
NGC 4125	39.39	-13.33±0.02	-13.51±0.02	-13.79±0.02	39.52±0.02	39.33±0.02	39.06±0.02
NGC 4136	5.9	-14.29±0.23	-14.82±0.23	-14.45±0.24	37.76±0.23	37.24±0.23	37.60±0.24
NGC 4138	416.37	-11.33±0.07	-13.36±0.07	-11.33±0.07	41.21±0.07	39.18±0.07	41.20±0.07
NGC 4143	71.08	-12.29±0.18	-12.65±0.27	-12.55±0.27	40.25±0.18	39.89±0.27	39.99±0.27
NGC 4144	<	-13.66	-	-	37.65	-	-
NGC 4151	2440.54	-10.30±0.01	-12.00±0.01	-10.31±0.01	42.39±0.01	40.70±0.01	42.39±0.01
NGC 4150	<	-14.27	-	-	37.78	-	-

Continued on next page

Table 9 – continued from previous page

Galaxy Name	Detection Signif.	log Flux 0.3–10 keV erg s^{-1} cm^{-2}	log Flux 0.3–2 keV erg s^{-1} cm^{-2}	log Flux 2–10 keV erg s^{-1} cm^{-2}	log Lum. 0.3–10 keV erg s^{-1}	log Lum. 0.3–2 keV erg s^{-1}	log Lum. 2–10 keV erg s^{-1}
(1)	(2)	(3)	(4)	(5)	(6)	(7)	(8)
NGC 4157	22.85	-13.12±0.28	-14.54±0.29	-13.14±0.29	39.42±0.28	38.00±0.29	39.40±0.29
NGC 4183	<	-14.02	-	-	38.52	-	-
NGC 4203	985.94	-11.59±0.03	-12.18±0.03	-11.72±0.03	40.46±0.03	39.87±0.03	40.33±0.03
NGC 4214	<	-15.87	-	-	35.30	-	-
NGC 4217	23.74	-13.74±0.09	-14.35±0.07	-13.97±0.32	38.80±0.09	38.44±0.32	38.57±0.32
NGC 4220	7.48	-13.34±0.17	-14.39±0.17	-13.38±0.20	39.20±0.17	38.15±0.17	39.16±0.20
NGC 4236	<	-12.79	-	-	37.97	-	-
NGC 4244	<	-15.15	-	-	35.91	-	-
NGC 4242	<	-14.52	-	-	37.31	-	-
NGC 4245	<	-14.05	-	-	38.00	-	-
NGC 4251	<	-12.81	-	-	39.24	-	-
NGC 4258	405.77	-11.06±0.01	-13.78±0.01	-11.06±0.01	40.68±0.01	37.96±0.01	40.68±0.01
NGC 4274	<	-11.91	-	-	40.14	-	-
NGC 4278	575.27	-12.31±0.02	-12.55±0.04	-12.69±0.04	39.74±0.02	39.50±0.04	39.37±0.04
NGC 4291	16.24	-13.36±0.05	-13.73±0.04	-13.60±0.07	39.66±0.05	39.28±0.04	39.42±0.07
NGC 4314	6.5	-13.69±0.22	-13.83±0.46	-14.23±0.46	38.37±0.22	38.22±0.46	37.82±0.46
NGC 4346	5.47	-13.39±0.23	-13.47±0.22	-14.14±0.22	39.15±0.23	39.06±0.22	38.40±0.22
NGC 4395	653.73	-11.28±0.05	-13.10±0.05	-11.29±0.05	39.91±0.05	38.09±0.05	39.90±0.05
NGC 4414	10.63	-13.39±0.31	-13.75±0.53	-13.64±0.53	38.66±0.31	38.30±0.53	38.41±0.53
NGC 4449	22.96	-14.19±0.30	-14.27±0.63	-14.96±0.63	36.85±0.30	36.77±0.63	36.07±0.63
NGC 4448	<	-13.57	-	-	38.48	-	-
NGC 4460	<	-13.77	-	-	38.13	-	-
NGC 4485	377.8	-15.27±0.49	-15.46±0.51	-15.74±0.51	36.74±0.49	36.56±0.51	36.28±0.51
NGC 4490	319.79	-12.14±0.08	-13.02±0.09	-12.21±0.09	39.72±0.08	38.85±0.09	39.66±0.09
NGC 4494	123.47	-12.77±0.09	-13.17±0.14	-13.00±0.14	39.28±0.09	38.89±0.14	39.05±0.14
NGC 4559	21.08	-13.03±0.29	-13.97±0.32	-13.08±0.32	39.03±0.29	38.08±0.32	38.97±0.32
NGC 4565	402.44	-12.33±0.05	-12.97±0.07	-12.44±0.07	39.72±0.05	39.08±0.07	39.61±0.07
NGC 4589	21.29	-13.32±0.16	-13.51±0.37	-13.78±0.38	39.71±0.16	39.52±0.37	39.25±0.38
NGC 4605	3.05	-13.64±0.23	-14.00±0.23	-13.89±0.23	37.64±0.23	37.28±0.23	37.40±0.23
NGC 4618	<	-12.68	-	-	39.12	-	-
NGC 4648	7.65	-13.99±0.31	-14.09±0.30	-14.68±0.30	38.97±0.31	38.86±0.30	38.28±0.30
NGC 4631	<	-12.91	-	-	38.85	-	-
NGC 4750	59.93	-12.50±0.17	-12.94±0.26	-12.70±0.26	40.41±0.17	39.98±0.26	40.21±0.26
NGC 4725	62.2	-13.13±0.09	-13.17±0.25	-14.19±0.25	39.14±0.09	39.10±0.25	38.07±0.25
NGC 4736	241.51	-11.85±0.03	-12.33±0.04	-12.02±0.04	39.50±0.03	39.01±0.04	39.32±0.04
NGC 4800	8.3	-13.62±0.31	-13.90±0.31	-13.95±0.31	38.82±0.31	38.55±0.31	38.49±0.31
NGC 4826	34.25	-13.22±0.02	-13.27±0.03	-14.22±0.07	38.08±0.02	38.04±0.04	37.08±0.07
NGC 4914	<	-14.08	-	-	39.58	-	-
NGC 5005	74.58	-13.59±0.27	-13.73±0.27	-14.16±0.27	39.15±0.27	39.01±0.27	38.58±0.27
NGC 5033	1143.3	-13.98±0.42	-14.12±0.41	-14.55±0.41	38.64±0.42	38.50±0.41	38.08±0.41
NGC 5055	58	-12.34±0.11	-12.45±0.23	-13.02±0.23	39.45±0.11	39.35±0.23	38.77±0.23
NGC 5204	<	-15.26	-	-	36.18	-	-
NGC 5194	165.74	-12.46±0.01	-12.64±0.01	-12.93±0.02	39.39±0.01	39.21±0.01	38.92±0.02
NGC 5195	45.28	-12.35±0.14	-12.36±0.18	-13.95±0.18	39.67±0.14	39.66±0.18	38.07±0.18
NGC 5273	46.83	-11.78±0.04	-13.00±0.04	-11.81±0.04	40.96±0.04	39.74±0.04	40.93±0.04
NGC 5297	<	-14.01	-	-	39.23	-	-

Continued on next page

Table 9 – continued from previous page

Galaxy Name	Detection Signif.	log Flux 0.3–10 keV erg s^{-1} cm^{-2}	log Flux 0.3–2 keV erg s^{-1} cm^{-2}	log Flux 2–10 keV erg s^{-1} cm^{-2}	log Lum. 0.3–10 keV erg s^{-1}	log Lum. 0.3–2 keV erg s^{-1}	log Lum. 2–10 keV erg s^{-1}
(1)	(2)	(3)	(4)	(5)	(6)	(7)	(8)
NGC 5308	4.97	-11.67±0.23	-13.15±0.24	-11.68±0.24	41.43±0.23	39.95±0.24	41.42±0.24
NGC 5322	21.35	-13.11±0.06	-13.19±0.04	-13.90±0.26	39.97±0.06	39.89±0.04	39.18±0.26
NGC 5354	20.07	-13.01±0.21	-13.03±0.36	-14.30±0.36	40.10±0.21	40.08±0.36	38.81±0.36
NGC 5353	20.07	-13.79±0.38	-13.85±0.37	-14.67±0.37	39.44±0.38	39.38±0.37	38.56±0.37
NGC 5371	3.95	-13.12±0.11	-13.22±0.23	-13.78±0.23	40.12±0.11	40.01±0.23	39.45±0.23
NGC 5377	6.22	-13.47±0.23	-14.27±0.27	-13.55±0.27	39.59±0.23	38.79±0.27	39.51±0.27
NGC 5383	<	-13.03	-	-	40.20	-	-
NGC 5395	29.73	-13.25±0.21	-13.36±0.39	-13.91±0.39	40.17±0.21	40.06±0.39	39.50±0.39
NGC 5448	13.2	-13.74±0.36	-13.81±0.35	-14.62±0.35	39.36±0.36	39.30±0.35	38.48±0.35
NGC 5457	97.3	-11.82±1.12	-11.84±0.39	-13.26±0.39	39.72±1.12	39.71±0.39	38.28±0.39
NGC 5473	3.37	-13.48±0.27	-14.51±0.32	-13.53±0.32	39.63±0.27	38.61±0.32	39.59±0.32
NGC 5474	88.09	-13.05±0.23	-13.12±0.36	-13.94±0.36	38.58±0.23	38.52±0.36	37.70±0.36
NGC 5485	7.28	-13.24±0.08	-13.62±0.13	-13.48±0.13	39.87±0.08	39.49±0.13	39.63±0.13
NGC 5548	1886	-10.52±0.01	-11.33±0.01	-10.59±0.01	43.21±0.01	42.40±0.01	43.14±0.01
NGC 5557	<	-12.29	-	-	41.05	-	-
NGC 5585	<	-12.01	-	-	39.76	-	-
NGC 5631	8.37	-13.43±0.26	-13.49±0.25	-14.31±0.25	39.68±0.26	39.61±0.25	38.80±0.25
NGC 5660	<	-14.01	-	-	39.21	-	-
NGC 5678	<	-12.01	-	-	41.17	-	-
NGC 5676	7.55	-13.44±0.27	-13.50±0.26	-14.30±0.26	39.72±0.27	39.65±0.26	38.85±0.26
NGC 5866	9.67	-12.87±0.02	-13.16±0.02	-13.19±0.02	39.57±0.02	39.28±0.02	39.26±0.02
NGC 5879	28.58	-14.01±0.40	-14.07±0.38	-14.89±0.39	38.52±0.40	38.45±0.38	37.64±0.39
NGC 5905	20.45	-13.46±0.21	-14.05±0.27	-13.60±0.27	39.91±0.21	39.32±0.27	39.78±0.27
NGC 5907	9.74	-12.83±0.12	-14.18±0.13	-12.85±0.13	39.59±0.12	38.24±0.13	39.57±0.13
NGC 5982	18.77	-13.71±0.35	-14.77±0.39	-13.75±0.39	39.55±0.35	38.48±0.39	39.51±0.39
NGC 5985	50.78	-11.74±0.03	-12.57±0.04	-11.81±0.04	41.52±0.03	40.70±0.04	41.45±0.04
NGC 6015	5.01	-13.07±0.20	-13.16±0.30	-13.80±0.30	39.50±0.20	39.41±0.30	38.77±0.30
NGC 6503	6.45	-13.53±0.25	-13.97±0.30	-13.93±0.29	38.12±0.25	37.68±0.30	37.72±0.29
NGC 6482	72.15	-12.66±0.18	-13.22±0.27	-12.81±0.27	40.85±0.18	40.30±0.27	40.71±0.27
NGC 6643	3.28	-12.63±0.08	-12.83±0.18	-13.05±0.18	40.27±0.08	40.06±0.18	39.84±0.18
NGC 6689	<	-13.96	-	-	38.29	-	-
NGC 6946	<	-12.38	-	-	39.18	-	-
NGC 7331	26.87	-12.60±0.08	-13.25±0.01	-12.72±0.10	39.78±0.08	39.14±0.10	39.67±0.10
NGC 7457	<	-13.91	-	-	38.34	-	-
NGC 7640	8.38	-12.36±0.26	<-15.26	-12.36±0.2	39.59±0.26	<36.68	39.59±0.26
NGC 7741	<	-13.86	-	-	38.39	-	-

Table 10: The basic parameters from the *Chandra* X-ray spectral fits, including those where the source was undetected. In this table, we only report the most basic parameters, e.g., the photon index and some of the neutral absorbers, but the table is continued in the additional tables in this appendix (see Table 11, 12). We show the (1) Galaxy name; (2) detection significance if detected, else a dash is used; (3) the X-ray spectral fit model used (see below for list of spectral models); (4) the Galactic absorption e.g., the PHABS parameter, obtained from Kalberla et al. (2005) in unit of 10^{20} cm^{-2}; (5) the additional absorption column density in cm^{-2} found in the ztbabs component, if any, divided by 10^{22}; (6) and (7) the ZPOWERLW model photon index and normalisation respectively; (8) the reduced χ-squared value (number), or where the source is faint and Poissonian statistical treatment is required of the data, the C-statistic divided by the number of degrees of freedom e.g., the cstat parameter reported by XSpec, denoted with a superscript letter 'c' The spectral models used are defined as follows: α : undetected; β : PHABS × ZTBABS × ZPOWERLW; γ : PHABS × ZTBABS(APEC + ZPOWERLW); δ : PHABS × ZTBABS × ZXIPCF × ZPOWERLW; ζ : PHABS × ZXIPCF × ZTBABS(APEC + ZPOWERLW); ω : PHABS × ZXIPCF × ZXIPCF × ZTBABS(APEC + GABS × ZPOWERLW); κ : PHABS × ZTBABS(ZGAUSS + ZPOWERLW); ι : PHABS × ZXIPCF × ZTBABS(ZGAUSS + ZPOWERLW); ϵ : PHABS × ZTBABS × ZPCFABS × ZPOWERLW; η : PHABS × ZXIPCF × ZTBABS(APEC + ZGAUSS + ZPOWERLW); θ : PHABS × ZPCFABS × ZTBABS(ZGAUSS + ZPOWERLW); μ : PHABS × ZXIPCF × ZXIPCF × ZTBABS × ZPOWERLW; π : PHABS × ZPCFABS × ZTBABS(APEC + ZPOWERLW); τ : PHABS(ZTBABS × CABS × CUTOFFPL + PEXRAV + CONST × CUTOFFPL + APEC + ZGAUSS); ρ : PHABS × ZTBABS(APEC + LAOR + ZGAUSS + ZPOWERLW);

Name	Det. Sig.	mod.	PHABS N_H	ZTBABS N_H	ZPOWERLW Phot.I.	ZPOWERLW norm.	cstat/ χ^2
(1)	(2)	(3)	(4)	(5)	(6)	(7)	(8)
IC10	-	α	50.6	-	-	-	-
NGC205	-	α	5.83	-	-	-	-
NGC221	-	α	18.3	-	-	-	-
NGC224	146.78	β	16.9	<0.04	$2.82^{+0.14}_{-0.13}$	$9.96^{+0.95}_{-0.84}\times10^{-5}$	0.87
NGC266	204.06	β	5.68	$0.23^{+0.10}_{-0.06}$	$1.91^{+0.14}_{-0.14}$	$3.05^{+0.51}_{-0.17}\times10^{-5}$	0.69
NGC278	11.87	β	12.9	<0.15	$2.25^{+1.22}_{-0.98}$	$2.30^{+1.34}_{-1.08}\times10^{-6}$	10.13/9^c
NGC315	33.96	ζ	5.90	$0.08^{+0.07}_{-0.06}$	$1.49^{+0.06}_{-0.08}$	$1.84^{+0.15}_{-0.32}\times10^{-4}$	1.06
NGC404	89.63	γ	5.71	$0.44^{+0.24}_{-0.29}$	$1.88^{+0.25}_{-0.23}$	$4.89^{+1.29}_{-1.02}\times10^{-6}$	15.57/20^c
NGC410	26.74	γ	5.11	$0.06^{+0.07}_{-0.06}$	<2.18	$1.95^{+2.11}_{-1.01}\times10^{-5}$	0.79
NGC507	58.35	γ	5.25	$0.07^{+0.07}_{-0.06}$	>2.77	$<3.71\times10^{-6}$	1.02
NGC598	280.24	δ	18.6	$0.03^{+0.02}_{-0.02}$	$1.33^{+0.04}_{-0.05}$	$5.13^{+7.28}_{-0.56}\times10^{-2}$	0.89
IC1727	-	α	8.5	-	-	-	-
NGC672	-	α	8.6	-	-	-	-
NGC697	-	α	6.4	-	-	-	-
NGC777	-	α	4.6	-	-	-	-
NGC890	-	α	6.2	-	-	-	-
NGC891	14.23	ϵ	7.4	$0.19^{+0.02}_{-0.02}$	$2.90^{+0.08}_{-0.07}$	$2.04^{+0.97}_{-0.90}\times10^{-4}$	1.05
NGC925	6.76	β	7.4	<0.44	>1.42	$9.70^{+9.84}_{-4.06}\times10^{-6}$	6.37/6^c
NGC959	-	α	5.4	-	-	-	-
IC239	-	α	6.1	-	-	-	-
NGC1003	-	α	7.2	-	-	-	-
NGC1023	97.11	β	5.6	<0.04	$1.96^{+0.14}_{-0.09}$	$1.55^{+0.19}_{-0.08}\times10^{-5}$	0.81
NGC1058	15.16	β	6.6	<0.43	$1.41^{+0.95}_{-0.49}$	$3.18^{+4.87}_{-1.29}\times10^{-6}$	13.44/18^c
NGC1156	-	α	11.7	-	-	-	-
NGC1161	14.7	ϵ	14.8	0.001 †	$3.45^{+0.19}_{-0.17}$	$9.71^{+1.19}_{-1.19}\times10^{-4}$	0.70
NGC1167	25.17	β	9.7	<0.16	$3.18^{+0.93}_{-0.48}$	$2.05^{+1.34}_{-0.38}\times10^{-5}$	0.77
NGC1275	205.26	ω	13.5	$0.15^{+0.02}_{-0.02}$	$1.96^{+0.22}_{-0.30}$	$7.65^{+4.54}_{-1.22}\times10^{-2}$	1.06
IC342	132.95	γ	36.2	$0.16^{+0.10}_{-0.13}$	$2.44^{+0.24}_{-0.22}$	$7.83^{+1.84}_{-1.52}\times10^{-5}$	0.98
NGC1569	-	α	22.4	-	-	-	-
NGC1961	32.74	β	8.0	$<6.49\times10^{-15}$	$1.47^{+0.29}_{-0.26}$	$9.09^{+1.81}_{-1.88}\times10^{-6}$	1.60
NGC2146	8.84	β	6.9	$5.20^{+1.07}_{-0.83}$	$2.29^{+0.45}_{-0.49}$	$2.09^{+0.38}_{-0.34}\times10^{-4}$	0.89
NGC2273	84.06	ι	5.8	<0.16	<2.75	$2.43^{+5.06}_{-1.22}\times10^{-4}$	0.88
UGC3828	-	α	5.0	-	-	-	-
NGC2276	3.67	β	6.0	$0.29^{+0.11}_{-0.10}$	$3.55^{+0.31}_{-0.29}$	$7.89^{+1.12}_{-1.13}\times10^{-6}$	1.46
NGC2300	39.02	β	5.8	<0.24	>3.90	$2.72^{+1.83}_{-0.42}\times10^{-5}$	1.06

Continued on next page

Table 10 – continued from previous page

Name	Det. Sig.	mod.	PHABS N_H	ZTBABS N_H	ZPOWERLW Phot.I.	ZPOWERLW norm.	cstat/ χ^2
(1)	(2)	(3)	(4)	(5)	(6)	(7)	(8)
NGC2403	151.93	β	11.5	$0.23^{+0.10}_{-0.09}$	$2.60^{+0.30}_{-0.27}$	$8.31^{+2.39}_{-1.78}\times10^{-5}$	40.00/34[c]
NGC2500	3.15	β	4.5	<0.54	>1.89	$2.30^{+3.79}_{-1.06}\times10^{-5}$	7.01/6[c]
NGC2537	-	α	4.7	-	-	-	-
NGC2541	3.21	β	5.7	<0.77	>1.41	$7.85^{+15.89}_{-4.89}\times10^{-6}$	0.74
NGC2549	15.18	δ	4.5	<0.51	-	-	-
NGC2639	40.84	γ	2.7	$1.40^{+0.22}_{-0.14}$	$2.22^{+0.59}_{-0.70}$	$6.55^{+5.56}_{-2.15}\times10^{-5}$	0.92
NGC2634	-	α	1.8	-	-	-	-
NGC2683	58.89	δ	3.5	<0.27	$1.02^{+0.53}_{-0.40}$	$1.58^{+3.11}_{-0.17}\times10^{-4}$	0.97
NGC2681	160.3	γ	2.3	<0.04	$1.50^{+0.18}_{-0.15}$	$5.55^{+1.00}_{-0.60}\times10^{-6}$	1.12
NGC2742	-	α	3.9	-	-	-	-
NGC2770	-	α	1.7	-	-	-	-
NGC2768	85.01	β	4.2	$0.26^{+0.08}_{-0.12}$	$1.75^{+0.19}_{-0.17}$	$1.40^{+0.08}_{-0.26}\times10^{-5}$	1.10
NGC2776	7.42	β	1.3	<1.88	<3.27	$3.26^{+25.08}_{-1.32}\times10^{-6}$	28.64/21[c]
NGC2748	8.58	β	1.9	<0.13	$2.00^{+0.46}_{-0.37}$	$7.41^{+3.42}_{-2.02}\times10^{-6}$	28.29/26[c]
NGC2782	112.45	η	1.4	$1.71^{+0.03}_{-0.11}$	$1.35^{+0.25}_{-0.20}$	$3.06^{+0.20}_{-0.20}\times10^{-5}$	1.24
NGC2787	147.73	β	4.8	$0.12^{+0.07}_{-0.07}$	$2.33^{+0.23}_{-0.21}$	$3.17^{+0.59}_{-0.49}\times10^{-5}$	34.95/30[c]
NGC2832	3.21	γ	1.2	$7.56^{+10.36}_{-6.17}\times10^{-2}$	$2.78^{+0.67}_{-0.60}$	$9.07^{+6.41}_{-4.19}\times10^{-5}$	0.79
NGC2841	54.21	γ	2.3	$0.71^{+0.19}_{-0.19}$	$1.68^{+0.31}_{-0.31}$	$1.09^{+0.42}_{-0.24}\times10^{-5}$	16.41/21[c]
NGC2903	76.23	γ	3.9	$0.22^{+0.04}_{-0.04}$	$2.19^{+0.11}_{-0.11}$	$2.75^{+0.30}_{-0.28}\times10^{-5}$	0.97
NGC2950	6.71	β	1.5	$0.89^{+0.33}_{-0.26}$	>3.32	$6.66^{+3.39}_{-1.68}\times10^{-5}$	1.44
NGC2976	3.05	β	4.9	$0.66^{+0.28}_{-0.24}$	>1.20	$1.26^{+0.90}_{-0.64}\times10^{-5}$	55.17/40[c]
NGC2985	90.18	β	2.2	<0.17	$2.26^{+0.44}_{-0.20}$	$2.38^{+0.99}_{-0.29}\times10^{-5}$	5.47/9[c]
NGC3031	622.22	ϵ	10.2	<2.22×10^{-15}	$1.24^{+0.02}_{-0.02}$	$3.00^{+0.65}_{-0.50}\times10^{-3}$	1.34
NGC3034	110.07	η	6.5	<0.16	$1.90^{+0.18}_{-0.18}$	$1.24^{+0.37}_{-0.30}\times10^{-4}$	1.00
NGC3043	-	α	1.3	-	-	-	-
NGC3073	-	α	0.9	-	-	-	-
NGC3079	28.31	κ	0.9	$1.03^{+0.41}_{-0.17}$	$1.96^{+0.41}_{-0.20}$	$4.23^{+2.53}_{-0.59}\times10^{-5}$	1.23
NGC3077	68.78	β	6.4	$0.91^{+0.51}_{-0.36}$	$1.39^{+0.30}_{-0.26}$	$1.16^{+0.63}_{-0.36}\times10^{-5}$	30.18/20[c]
NGC3147	338.43	β	2.0	$2.54^{+2.02}_{-1.93}\times10^{-2}$	$1.44^{+0.08}_{-0.09}$	$6.09^{+0.18}_{-0.18}\times10^{-4}$	1.17
NGC3185	11.51	δ	1.9	<0.13	$2.71^{+0.34}_{-0.35}$	<1.25×10^{-2}	0.73
NGC3190	68.72	δ	1.8	<0.23	$3.71^{+0.38}_{-0.37}$	$8.51^{+7.29}_{-5.28}\times10^{-3}$	0.58
NGC3184	34.93	β	1.7	$0.19^{+0.16}_{-0.12}$	$2.17^{+0.52}_{-0.45}$	$6.72^{+2.90}_{-1.74}\times10^{-6}$	3.69/6[c]
NGC3193	8.66	β	1.9	<0.07	$2.14^{+0.48}_{-0.30}$	$1.42^{+0.44}_{-0.20}\times10^{-5}$	19.52/13[c]
NGC3198	30.81	β	1.6	$0.63^{+0.44}_{-0.24}$	$2.07^{+0.54}_{-0.45}$	$5.96^{+4.56}_{-1.72}\times10^{-6}$	4.40/6[c]
NGC3245	31.02	β	1.8	<0.08	$1.96^{+0.29}_{-0.26}$	$1.57^{+0.31}_{-0.18}\times10^{-5}$	1.58/4[c]
IC2574	-	α	5.9	-	-	-	-
NGC3310	159.06	β	1.5	$8.34^{+7.31}_{-6.56}\times10^{-2}$	$1.17^{+0.13}_{-0.13}$	$2.57^{+0.41}_{-0.35}\times10^{-5}$	119.25/122[c]
NGC3319	30.77	β	1.3	<0.31	$1.95^{+0.60}_{-0.29}$	$1.45^{+1.26}_{-0.30}\times10^{-5}$	15.69/10[c]
NGC3344	42.61	β	3.7	<0.09	$2.00^{+0.34}_{-0.22}$	$1.15^{+0.35}_{-0.16}\times10^{-5}$	53.72/48[c]
NGC3359	-	α	0.9	-	-	-	-
NGC3395	13.8	β	2.2	$9.68^{+14.48}_{-9.10}\times10^{-2}$	$2.48^{+1.00}_{-0.60}$	$1.97^{+0.12}_{-0.57}\times10^{-5}$	52.94/39[c]
NGC3414	195.7	β	1.5	$0.24^{+0.04}_{-0.04}$	$1.87^{+0.15}_{-0.15}$	$9.72^{+0.40}_{-0.40}\times10^{-5}$	0.55
NGC3430	-	α	1.8	-	-	-	-
NGC3432	-	α	1.8	-	-	-	-
NGC3448	28.32	β	0.9	$2.08^{+0.92}_{-0.83}$	$2.67^{+0.74}_{-0.67}$	$1.35^{+2.34}_{-0.82}\times10^{-4}$	20.18/24[c]
NGC3486	-	α	1.8	-	-	-	-
NGC3516	1353.47	δ	3.1	<0.10	$2.50^{+0.57}_{-0.37}$	$1.43^{+2.11}_{-0.78}\times10^{-3}$	1.21

Continued on next page

Table 10 – continued from previous page

	Det.		PHABS	ZTBABS	ZPOWERLW		cstat/
Name	Sig.	mod.	$N_{\rm H}$	$N_{\rm H}$	Phot.I.	norm.	χ^2
(1)	(2)	(3)	(4)	(5)	(6)	(7)	(8)
NGC3556	83.27	β	1.2	$0.52^{+0.14}_{-0.07}$	$1.91^{+0.22}_{-0.20}$	$1.54^{+0.39}_{-0.13}\times10^{-5}$	19.24/20$^{\rm c}$
NGC3583	6.34	β	1.4	$<7.79\times10^{-2}$	$2.12^{+0.67}_{-0.56}$	$1.03^{+0.39}_{-0.29}\times10^{-5}$	9.99/7$^{\rm c}$
NGC3600	36.78	β	1.4	$<8.53\times10^{-2}$	$1.64^{+0.35}_{-0.32}$	$2.01^{+0.55}_{-0.43}\times10^{-5}$	15.74/13$^{\rm c}$
NGC3610	4.07	β	0.6	<0.26	$2.31^{+1.07}_{-0.72}$	$1.57^{+1.24}_{-0.63}\times10^{-5}$	31.63/33$^{\rm c}$
NGC3613	-	α	0.7	-	-	-	-
NGC3631	75.83	β	1.0	$0.13^{+0.08}_{-0.08}$	$2.45^{+0.26}_{-0.23}$	$1.26^{+0.25}_{-0.20}\times10^{-5}$	1.02
NGC3642	38.06	β	0.7	<0.17	$2.81^{+0.89}_{-0.32}$	$3.63^{+0.26}_{-0.72}\times10^{-5}$	16.56/19$^{\rm c}$
NGC3665	20.66	β	1.8	$<2.57\times10^{-2}$	$2.15^{+0.21}_{-0.20}$	$2.48^{+0.29}_{-0.26}\times10^{-5}$	42.83/37$^{\rm c}$
NGC3675	-	α	2.8	-	-	-	-
NGC3690	97.24	κ	0.8	$0.43^{+0.09}_{-0.08}$	$1.66^{+0.11}_{-0.11}$	$6.84^{+0.93}_{-0.76}\times10^{-5}$	1.07
UGC6484	-	α	1.1	-	-	-	-
NGC3718	405.72	β	0.9	$1.28^{+0.13}_{-0.12}$	$1.67^{+0.11}_{-0.11}$	$7.72^{+0.12}_{-0.10}\times10^{-4}$	0.87
NGC3726	-	α	1.6	-	-	-	-
NGC3729	8.88	θ	0.9	$1.00\times10^{-3}\dagger$	$3.42^{+0.65}_{-0.39}$	$2.14^{+0.54}_{-0.46}\times10^{-4}$	25.47/24$^{\rm c}$
NGC3738	-	α	1.0	-	-	-	-
NGC3756	-	α	0.8	-	-	-	-
NGC3780	-	α	1.1	-	-	-	-
NGC3838	7.83	β	0.7	$0.63^{+1.14}_{-0.58}$	$3.18^{+1.77}_{-1.15}$	$1.56^{+4.92}_{-1.54}\times10^{-5}$	18.62/15$^{\rm c}$
NGC3877	11.58	β	2.5	$0.16^{+0.21}_{-0.13}$	$3.08^{+1.52}_{-0.90}$	$7.51^{+7.00}_{-2.89}\times10^{-6}$	18.40/25$^{\rm c}$
NGC3884	186.12	β	1.9	$<7.34\times10^{-2}$	$1.62^{+0.16}_{-0.15}$	$1.64^{+0.27}_{-0.22}\times10^{-4}$	0.85
NGC3893	-	α	2.4	-	-	-	-
NGC3898	52.8	β	0.8	$<2.13\times10^{-2}$	$2.31^{+0.15}_{-0.14}$	$8.48^{+0.63}_{-0.54}\times10^{-6}$	22.29/20$^{\rm c}$
NGC3917	-	α	1.5	-	-	-	-
NGC3938	11.6	β	1.8	<0.66	$1.75^{+0.94}_{-0.45}$	$1.80^{+2.58}_{-0.57}\times10^{-6}$	29.26/28$^{\rm c}$
NGC3945	162.23	β	2.0	$0.14^{+0.07}_{-0.07}$	$2.62^{+0.23}_{-0.21}$	$6.86^{+1.22}_{-1.02}\times10^{-5}$	1.07
NGC3949	-	α	2.2	-	-	-	-
NGC3953	7.27	β	2.1	<0.24	$1.39^{+0.62}_{-0.50}$	$5.98^{+2.53}_{-1.95}\times10^{-6}$	40.48/52$^{\rm c}$
NGC3963	19.01	β	1.7	<0.12	$1.17^{+0.56}_{-0.49}$	$7.10^{+3.47}_{-2.69}\times10^{-6}$	12.46/9$^{\rm c}$
NGC3982	27.6	β	1.0	$0.20^{+0.21}_{-0.14}$	$4.83^{+1.64}_{-1.13}$	$2.36^{+2.04}_{-0.89}\times10^{-5}$	35.52/28$^{\rm c}$
NGC3992	3.41	β	2.0	$3.48^{+1.70}_{-1.53}$	>1.17	$1.63^{+1.73}_{-0.71}\times10^{-4}$	28.05/23$^{\rm c}$
NGC3998	1817.56	β	1.0	$<1.26\times10^{-2}$	$1.77^{+0.08}_{-0.06}$	$1.33^{+0.05}_{-0.05}\times10^{-4}$	1.05
NGC4013	84.77	β	1.4	<0.20	$3.00^{+1.61}_{-0.74}$	$2.74^{+2.29}_{-0.72}\times10^{-6}$	97.84/95$^{\rm c}$
NGC4026	10.82	β	2.1	<0.10	$1.41^{+0.60}_{-0.33}$	$4.34^{+2.05}_{-0.87}\times10^{-6}$	38.37/32$^{\rm c}$
NGC4036	54.81	ζ	1.9	<0.12	$2.76^{+0.30}_{-0.32}$	$1.16^{+1.71}_{-0.80}\times10^{-3}$	0.68
NGC4041	5.86	β	1.8	<0.25	$3.36^{+1.24}_{-0.74}$	$3.31^{+2.76}_{-1.20}\times10^{-5}$	1.28
NGC4051	1158.28	μ	1.2	$<9.57\times10^{-3}$	$2.26^{+0.10}_{-0.08}$	$0.70^{+0.25}_{-0.20}$	1.06
NGC4062	-	α	1.8	-	-	-	-
NGC4088	12.55	β	1.6	<0.13	$1.07^{+0.28}_{-0.26}$	$3.74^{+1.08}_{-0.84}\times10^{-6}$	30.13/18$^{\rm c}$
NGC4096	3.55	β	2.0	<0.97	$1.80\dagger$	$2.72^{+3.31}_{-1.48}\times10^{-6}$	14.93/11$^{\rm c}$
NGC4100	-	α	2.2	-	-	-	-
NGC4102	264.99	ζ	1.6	$0.59^{+0.10}_{-0.10}$	$2.13^{+0.26}_{-0.30}$	$6.65^{+4.53}_{-2.68}\times10^{-3}$	0.92
NGC4111	62.38	π	1.4	$3.69^{+2.19}_{-2.32}\times10^{-2}$	$2.25^{+0.13}_{-0.17}$	$1.77^{+0.49}_{-0.26}\times10^{-4}$	0.82
NGC4125	39.39	ζ	1.8	$<9.57\times10^{-3}$	$1.80^{+0.28}_{-0.33}$	$5.17^{+2.20}_{-1.67}\times10^{-6}$	1.09
NGC4136	5.9	β	1.7	$0.23^{+0.51}_{-0.27}$	$1.80\dagger$	$1.06^{+0.73}_{-0.50}\times10^{-6}$	15.48/12$^{\rm c}$
NGC4138	416.37	β	1.1	$9.48^{+0.93}_{-0.82}$	$1.34^{+0.17}_{-0.18}$	$4.57^{+1.04}_{-1.22}\times10^{-4}$	0.98
NGC4143	71.08	β	1.2	$<6.65\times10^{-2}$	$1.56^{+0.31}_{-0.26}$	$7.16^{+1.25}_{-0.75}\times10^{-5}$	1.29
NGC4144	-	α	2.1	-	-	-	-

Continued on next page

Table 10 – continued from previous page

Name	Det. Sig.	mod.	PHABS N_H	ZTBABS N_H	ZPOWERLW Phot.I.	ZPOWERLW norm.	cstat/ χ^2
(1)	(2)	(3)	(4)	(5)	(6)	(7)	(8)
NGC4151	2440.54	τ	2.1	$8.73^{+5.75}_{-5.64}\times10^{-3}$	$1.84^{+0.08}_{-0.08}$	$0.5^{+0.01}_{-0.06}$	1.18
NGC4150	-	α	1.4	-	-	-	-
NGC4157	22.85	β	2.1	<0.12	$1.02^{+0.26}_{-0.18}$	$3.30^{+1.04}_{-0.58}\times10^{-6}$	71.29/45[c]
NGC4183	-	α	1.2	-	-	-	-
NGC4203	985.94	μ	1.1	$0.10^{+0.03}_{-0.01}$	$2.34^{+0.14}_{-0.13}$	$4.35^{+1.82}_{-1.93}\times10^{-2}$	0.84
NGC4214	-	α	4.0	-	-	-	-
NGC4217	23.74	ϵ	1.9	$1.08^{+95.9}_{-0.45}\times10^{-3}$	$2.80^{+0.33}_{-0.44}$	$2.92^{+1.10}_{-1.43}\times10^{-5}$	46.00/53[c]
NGC4220	7.48	β	1.6	<2.51	<2.46	$4.15^{+24.30}_{-1.86}\times10^{-6}$	21.41/34[c]
NGC4236	-	α	5.5	-	-	-	-
NGC4244	-	α	5.0	-	-	-	-
NGC4242	-	α	1.5	-	-	-	-
NGC4245	-	α	1.9	-	-	-	-
NGC4251	-	α	1.9	-	-	-	-
NGC4258	405.77	δ	4.2	$5.97^{+0.18}_{-0.20}$	$1.22^{+0.20}_{-0.23}$	$1.04^{+47.01}_{-0.02}\times10^{-2}$	1.15
NGC4274	-	α	2.2	-	-	-	-
NGC4278	575.27	β	2.0	$<1.50\times10^{-2}$	$2.24^{+0.05}_{-0.04}$	$1.01^{+0.04}_{-0.03}\times10^{-4}$	1.40
NGC4291	16.24	γ	3.0	$0.49^{+0.30}_{-0.33}$	<1.57	$5.96^{+3.03}_{-1.73}\times10^{-5}$	11.29/9[c]
NGC4314	6.5	β	2.3	$0.31^{+0.13}_{-0.10}$	$4.73^{+0.95}_{-0.77}$	$5.96^{+3.03}_{-1.73}\times10^{-5}$	1.20
NGC4346	5.47	β	1.2	<0.17	$1.94^{+0.73}_{-0.49}$	$7.30^{+3.44}_{-2.18}\times10^{-6}$	54.81/40[c]
NGC4395	653.73	δ	4.3	$0.21^{+0.04}_{-0.04}$	$1.19^{+0.24}_{-0.23}$	$4.54^{+2.63}_{-1.75}\times10^{-4}$	1.06
NGC4414	10.63	β	1.6	$<3.56\times10^{-2}$	$1.90^{+0.26}_{-0.23}$	$1.97^{+0.32}_{-0.26}\times10^{-5}$	28.77/24[c]
NGC4449	22.96	β	4.1	$5.90^{+0.04}_{-0.04}\times10^{-2}$	$2.64^{+0.25}_{-0.22}$	$4.08^{+0.64}_{-0.52}\times10^{-5}$	1.16
NGC4448	-	α	1.8	-	-	-	-
NGC4460	-	α	1.5	-	-	-	-
NGC4485	377.8	β	3.9	$1.13^{+0.11}_{-0.10}$	$2.56^{+0.11}_{-0.11}$	$2.36^{+0.34}_{-0.28}\times10^{-4}$	0.88
NGC4490	319.79	β	3.8	$1.21^{+0.11}_{-0.10}$	$2.39^{+0.11}_{-0.10}$	$2.31^{+0.32}_{-0.27}\times10^{-4}$	1.06
NGC4494	123.47	β	1.4	$0.12^{+0.06}_{-0.06}$	$2.13^{+0.18}_{-0.17}$	$3.25^{+0.49}_{-0.43}\times10^{-5}$	1.20
NGC4559	21.08	β	1.4	<0.20	$1.21^{+0.63}_{-0.41}$	$5.59^{+4.17}_{-1.66}\times10^{-6}$	0.94
NGC4565	402.44	β	1.1	$0.34^{+0.03}_{-0.02}$	$1.91^{+0.07}_{-0.07}$	$8.09^{+0.58}_{-0.30}\times10^{-5}$	0.97
NGC4589	21.29	β	2.2	<0.35	$2.49^{+1.24}_{-0.51}$	$1.15^{+1.26}_{-0.30}\times10^{-5}$	1.14
NGC4605	3.05	β	1.6	<0.10	1.80†	$6.35^{+2.08}_{-2.08}\times10^{-6}$	19.70/21[c]
NGC4618	-	α	2.5	-	-	-	-
NGC4648	7.65	β	1.9	<0.29	$2.00^{+1.61}_{-0.63}$	$3.47^{+3.47}_{-1.06}\times10^{-6}$	20.80/30[c]
NGC4631	-	α	3.4	-	-	-	-
NGC4750	59.93	β	1.6	<0.18	$1.88^{+0.47}_{-0.38}$	$5.37^{+2.44}_{-1.48}\times10^{-5}$	0.75
NGC4725	62.2	β	0.8	<0.049	$3.38^{+0.34}_{-0.24}$	$1.32^{+0.17}_{-0.11}\times10^{-5}$	0.99
NGC4736	241.51	β	1.9	<0.10	$1.91^{+0.34}_{-0.16}$	$7.81^{+2.13}_{-0.70}\times10^{-6}$	0.94
NGC4800	8.3	β	1.3	<0.28	$2.05^{+0.75}_{-0.62}$	$6.26^{+3.64}_{-2.36}\times10^{-6}$	15.97/17[c]
NGC4826	34.25	γ	3.0	<0.14	1.80†	$1.29^{+0.99}_{-0.92}\times10^{-6}$	21.01/14[c]
NGC4914	-	α	1.2	-	-	-	-
NGC5005	74.58	γ	1.2	$6.66^{+0.05}_{-0.05}\times10^{-2}$	$1.90^{+0.48}_{-0.43}$	$4.01^{+0.68}_{-0.68}\times10^{-5}$	0.86
NGC5033	1143.3	δ	1.1	$<1.27\times10^{-2}$	$1.39^{+0.03}_{-0.02}$	$6.60^{+4.71}_{-0.63}\times10^{-3}$	1.14
NGC5055	58	β	3.7	$<6.29\times10^{-2}$	$1.60^{+0.17}_{-0.16}$	$1.80^{+0.30}_{-0.25}\times10^{-5}$	25.31/25[c]
NGC5204	-	α	2.7	-	-	-	-
NGC5194	165.74	τ	3.3	$66.01^{+34.79}_{-22.53}$	$3.5^{+0.27}_{-0.24}$	$2.04^{+0.26}_{-0.23}\times10^{-5}$	1.94
NGC5195	45.28	β	3.2	$<1.68\times10^{-2}$	$1.48^{+0.10}_{-0.10}$	$1.01^{+0.08}_{-0.08}\times10^{-5}$	68.71/44[c]
NGC5273	46.83	δ	0.8	$<7.56\times10^{-2}$	$1.66^{+0.51}_{-0.27}$	$6.87^{+11.68}_{-4.23}\times10^{-4}$	0.80

Continued on next page

Table 10 – continued from previous page

Name	Det. Sig.	mod.	PHABS N_H	ZTBABS N_H	ZPOWERLW Phot.I.	ZPOWERLW norm.	cstat/ χ^2
(1)	(2)	(3)	(4)	(5)	(6)	(7)	(8)
NGC5297	-	α	1.3	-	-	-	-
NGC5308	4.97	β	1.7	<1.78	$2.06^{+0.79}_{-0.76}$	$6.36^{+3.82}_{-3.23}\times10^{-5}$	0.79
NGC5322	21.35	β	1.4	$0.13^{+0.11}_{-0.08}$	$3.46^{+0.79}_{-0.56}$	$3.65^{+1.64}_{-0.93}\times10^{-5}$	1.06
NGC5354	20.07	β	1.0	$<5.90\times10^{-2}$	$1.86^{+0.29}_{-0.15}$	$1.12^{+0.25}_{-0.10}\times10^{-5}$	89.38/71[c]
NGC5353	20.07	γ	1.0	$1.58^{+0.21}_{-0.18}$	$3.63^{+1.25}_{-1.35}$	$3.80^{+0.73}_{-0.59}\times10^{-5}$	1.10
NGC5371	3.95	β	0.9	$0.46^{+0.09}_{-0.07}$	>3.83	$4.77^{+1.34}_{-1.17}\times10^{-5}$	0.62
NGC5377	6.22	β	1.7	<4.27	$1.52^{+3.02}_{-0.47}$	$5.87^{+305.53}_{-1.99}\times10^{-6}$	0.77
NGC5383	-	α	1.0	-	-	-	-
NGC5395	29.73	β	1.1	$<7.90\times10^{-2}$	$1.49^{+0.38}_{-0.20}$	$9.73^{+3.13}_{-1.20}\times10^{-6}$	32.59/30[c]
NGC5448	13.2	β	1.4	<0.28	$2.81^{+1.60}_{-0.49}$	$1.73^{+2.35}_{-0.39}\times10^{-5}$	0.63
NGC5457	97.3	β	8.6	$6.69^{+6.92}_{-6.41}\times10^{-2}$	$2.12^{+0.18}_{-0.16}$	$1.30^{+0.21}_{-0.18}\times10^{-6}$	29.92/31[c]
NGC5473	3.37	β	1.21	$1.31^{+1.85}_{-1.02}$	1.80†	$9.59^{+11.02}_{-5.39}\times10^{-6}$	2.72/6[c]
NGC5474	88.09	β	1.9	<0.15	$1.88^{+0.79}_{-0.43}$	$2.59^{+1.14}_{-0.48}\times10^{-6}$	69.36/53[c]
NGC5485	7.28	β	1.1	<0.25	$1.98^{+0.82}_{-0.66}$	$6.48^{+4.02}_{-2.69}\times10^{-6}$	1.00
NGC5548	1886	λ	1.6	$9.78^{+1.23}_{-2.50}\times10^{-2}$	$1.95^{+0.04}_{-0.12}$	$0.73^{+0.11}_{-0.22}$	1.14
NGC5557	-	α	0.9	-	-	-	-
NGC5585	-	α	2.7	-	-	-	-
NGC5631	8.37	β	1.4	<0.22	$3.47^{+0.75}_{-0.45}$	$1.32^{+0.74}_{-0.29}\times10^{-5}$	9.49/18[c]
NGC5660	-	α	1.8	-	-	-	-
NGC5678	-	α	1.1	-	-	-	-
NGC5676	7.55	β	2.6	<0.86	$1.87^{+1.55}_{-0.39}$	$6.62^{+20.72}_{-1.85}\times10^{-6}$	19.33/18[c]
NGC5866	9.67	ϵ	1.3	$0.26^{+0.04}_{-0.02}$	$4.22^{+0.25}_{-0.15}$	$1.20^{+0.14}_{-0.18}\times10^{-3}$	1.36
NGC5879	28.58	δ	1.6	<0.27	$3.23^{+0.97}_{-0.79}$	$<4.47\times10^{-3}$	1.23
NGC5905	20.45	γ	1.3	<0.17	$2.49^{+0.88}_{-0.66}$	$2.71^{+1.87}_{-1.18}\times10^{-6}$	7.48/6[c]
NGC5907	9.74	β	2.0	<0.25	$0.89^{+0.48}_{-0.31}$	$2.43^{+1.67}_{-0.67}\times10^{-6}$	50.94/38[c]
NGC5982	18.77	β	1.5	$<8.03\times10^{-2}$	$2.52^{+0.43}_{-0.39}$	$1.56^{+0.36}_{-0.29}\times10^{-5}$	15.55/8[c]
NGC5985	50.78	β	1.6	$1.01^{+0.77}_{-0.69}$	$2.27^{+0.68}_{-0.63}$	$6.82^{+8.31}_{-3.65}\times10^{-5}$	0.67
NGC6015	5.01	β	1.3	<0.45	>2.69	$1.07^{+1.64}_{-0.35}\times10^{-5}$	44.41/42[c]
NGC6503	6.45	β	4.8	<0.50	$2.28^{+1.55}_{-1.02}$	$3.44^{+6.43}_{-1.93}\times10^{-6}$	12.30/16[c]
NGC6482	72.15	γ	8.2	$0.23^{+0.08}_{-0.07}$	$3.19^{+0.96}_{-0.61}$	$2.19^{+1.12}_{-0.92}\times10^{-5}$	0.90
NGC6643	3.28	β	5.1	$0.59^{+0.47}_{-0.42}$	$2.01^{+2.06}_{-0.98}$	$3.93^{+2.08}_{-1.65}\times10^{-6}$	17.19/14[c]
NGC6689	-	α	5.3	-	-	-	-
NGC6946	-	α	22.0	-	-	-	-
NGC7331	26.87	β	7.0	<0.13	$1.67^{+0.43}_{-0.24}$	$7.46^{+2.75}_{-1.15}\times10^{-6}$	1.04
NGC7457	-	α	4.4	-	-	-	-
NGC7640	8.38	β	10.5	$108.92^{+78.23}_{-56.70}$	$3.26^{+1.11}_{-2.51}$	$>5.55\times10^{-3}$	8.04/13[c]
NGC7741	-	α	4.9	-	-	-	-

Table 11: Additional spectral parameters for more complex spectral fits, including additional APEC, ZGAUSS and GABS models. This table is only relevant for spectra fit with spectral models ζ, γ, ω, δ, ι, η, κ, θ and π=. Note that where the †symbol is used, this denotes the parameter was frozen before fitting. The errors shown in this table are all at the 1σ level.

		APEC		ZGAUSS			GABS		
Name	mod.	kT	norm.	LineE	sigma	norm.	LineE	sigma	Strength
(1)	(2)	(3)	(4)	(5)	(6)	(7)	(8)	(9)	(10)
NGC315	ζ	$0.54^{+0.02}_{-0.04}$	$2.62^{+0.54}_{-0.61}\times10^{-4}$	-	-	-	-	-	-
NGC404	γ	$0.24^{+0.07}_{-0.05}$	$5.17^{+16.96}_{-4.06}\times10^{-5}$	-	-	-	-	-	-
NGC410	γ	$0.78^{+0.04}_{-0.05}$	$2.07^{+0.41}_{-0.39}\times10^{-4}$	-	-	-	-	-	-
NGC507	γ	$0.91^{+0.04}_{-0.05}$	$5.89^{+0.77}_{-0.64}\times10^{-5}$	-	-	-	-	-	-
NGC1275	ω	$0.79^{+0.04}_{-0.04}$	$1.42^{+0.46}_{-0.20}\times10^{-2}$	-	-	-	$6.64^{+0.06}_{-0.07}$	$0.69^{+0.04}_{-0.04}$	1 †
IC342*	γ	$0.82^{+0.17}_{-0.07}$	$6.75^{+2.77}_{-1.81}\times10^{-5}$	-	-	-	-	-	-
NGC2273	ι	-	-	$6.41^{+0.02}_{-0.02}$	$9.54^{+2.78}_{-2.96}\times10^{-2}$	$5.56^{+1.22}_{-1.46}\times10^{-5}$	-	-	-
NGC2549	δ	$1.80^{+0.73}_{-0.42}$	$<7.72\times10^{-2}$	-	-	-	-	-	-
NGC2639	γ	$0.11^{+0.01}_{-0.02}$	$0.48^{+3.11}_{-0.29}$	-	-	-	-	-	-
NGC2681	γ	$0.79^{+0.02}_{-0.03}$	$1.11^{+0.12}_{-0.09}\times10^{-5}$	-			-	-	-
NGC2782	η	$0.11^{+0.01}_{-0.01}$	$0.55^{+0.03}_{-0.03}$	$6.48^{+0.05}_{-0.07}$	$0.23^{+0.11}_{-0.07}$	$8.16^{+1.68}_{-1.73}\times10^{-6}$	-	-	-
NGC2832	γ	$1.21^{+0.09}_{-0.13}$	$2.27^{+0.47}_{-0.43}\times10^{-4}$	-	-	-	-	-	-
NGC2841	γ	$0.24^{+0.05}_{-0.05}$	$3.83^{+8.82}_{-2.38}\times10^{-4}$	-	-	-	-	-	-
NGC2903	γ	$0.68^{+0.05}_{-0.08}$	$9.54^{+2.69}_{-2.15}\times10^{-6}$	-	-	-	-	-	-
NGC3034	η	$0.83^{+0.02}_{-0.02}$	$1.31^{+0.26}_{-0.24}\times10^{-3}$	$6.69^{+0.03}_{-0.02}$	0.01 †	$2.24^{+0.56}_{-0.58}\times10^{-6}$	-	-	-
NGC3079	κ	-	-	$6.44^{+0.05}_{-0.05}$	$0.18^{+0.07}_{-0.05}$	$8.37^{+1.81}_{-1.73}\times10^{-6}$	-	-	-
NGC3690*	κ	-	-	$6.41^{+0.03}_{-0.03}$	$7.83^{+3.61}_{-6.70}\times10^{-2}$	$4.98^{+1.08}_{-1.12}\times10^{-6}$	-	-	-
NGC3729	θ	-	-	$6.42^{+0.09}_{-0.08}$	$0.14^{+0.11}_{-0.08}$	$1.30^{+0.48}_{-0.41}\times10^{-5}$	-	-	-
NGC4036	ζ	$0.74^{+0.07}_{-0.08}$	$8.67^{+17.45}_{-5.39}\times10^{-4}$	-	-	-	-	-	-
NGC4102	ζ	$0.79^{+0.04}_{-0.04}$	$2.95^{+1.54}_{-0.97}\times10^{-2}$	-	-	-	-	-	-
NGC4111*	π	$0.66^{+0.06}_{-0.02}$	$1.56^{+0.08}_{-0.08}\times10^{-3}$	-	-	-	-	-	-
NGC4125	ζ	$0.85^{+0.04}_{-0.08}$	$2.23^{+2.48}_{-1.06}\times10^{-5}$	-	-	-	-	-	-
NGC4151	τ	$0.15^{+0.01}_{-0.01}$	$1.12^{+0.02}_{-0.02}$	$6.41^{+0.01}_{-0.01}$	$6.74^{+1.11}_{-1.07}\times10^{-2}$	$1.45^{+0.11}_{-0.10}\times10^{-3}$	$6.69^{+0.02}_{-0.02}$	$0.92^{+0.01}_{-0.01}$	$1.46^{+0.02}_{-0.02}$
NGC4291	γ	$0.27^{+0.13}_{-0.07}$	$5.59^{+22.09}_{-3.76}\times10^{-5}$	-	-	-	-	-	-
NGC4826	γ	$0.61^{+0.05}_{-0.05}$	$3.00^{+0.89}_{-0.61}\times10^{-5}$	-	-	-	-	-	-
NGC5005	γ	$1.00^{+0.06}_{-0.07}$	$5.14^{+0.89}_{-0.89}\times10^{-5}$	-	-	-	-	-	-
NGC5194	τ	$0.74^{+0.01}_{-0.01}$	$8.47^{+0.58}_{-0.51}\times10^{-5}$	$6.41^{+0.01}_{-0.01}$	<0.05	$4.52^{+0.47}_{-0.46}\times10^{-6}$	-	-	-
NGC5353	γ	$9.09^{+0.23}_{-0.40}\times10^{-2}$	$0.47^{+0.85}_{-0.40}$	-	-	-	-	-	-
NGC5905	γ	$0.68^{+0.04}_{-0.12}$	$4.45^{+3.56}_{-1.29}\times10^{-6}$	-	-	-	-	-	-
NGC6482	γ	$0.83^{+0.05}_{-0.04}$	$1.29^{+0.26}_{-0.19}\times10^{-4}$	-	-	-	-	-	-

Table 12: Additional spectral parameters for more complex spectral fits, including additional zpcfabs and zxipcf models, as well as the second apec model for NGC 4151. This table is only relevant for spectra fit with spectral models ζ, ϵ, ω, δ, ι, η, θ, μ, τ, π and λ. Note that where the †symbol is used, this denotes the parameter was frozen before fitting. The errors shown in this table are all at the 1σ level.

		zpcfabs		zxipcf			zxipcf (2)			apec (2)	
Name	mod.	$N_{\rm H}$	CvrFract.	$N_{\rm H}$	logxi	CvrFract.	$N_{\rm H}$	logxi	CvrFract. kT	norm.	
(1)	(2)	(3)	(4)	(5)	(6)	(7)	(8)	(9)	(10)	(11)	(12)
NGC315	ζ	-	-	$0.39^{+0.03}_{-0.04}$	<-1.59	$0.84^{+0.05}_{-0.07}$	-	-	-	-	-
NGC598	δ	-	-	$177.28^{+0.81}_{-0.89}$	$0.26^{+0.03}_{-0.59}$	$0.99^{+0.01}_{-0.01}$	-	-	-	-	-
NGC891	ϵ	$9.34^{+1.01}_{-0.86}$	$0.95^{+0.01}_{-0.04}$	-	-	-	-	-	-	-	-
NGC1161	ϵ	$20.63^{+6.48}_{-4.40}$	$0.97^{+0.02}_{-0.04}$	-	-	-	-	-	-	-	-
NGC1275	ω	-	-	$1.79^{+0.13}_{-0.13}$	-3 †	$0.79^{+0.04}_{-0.03}$	$61.86^{+0.95}_{-0.55}$	$-0.55^{+0.06}_{-0.11}$	$0.99^{+0.01}_{-0.01}$	-	-
NGC2273	ι	-	-	$15.69^{+5.74}_{-8.36}$	0.01 †	$0.90^{+0.02}_{-0.10}$	-	-	-	-	-
NGC2549	δ	-	-	$65.95^{+333.194}_{-32.77}$	<1.70	>0.84	-	-	-	-	-
NGC2683	δ	-	-	$46.16^{+6.30}_{-6.64}$	$-2.00^{+0.05}_{-0.02}$	1 †	-	-	-	-	-
NGC2782	η	-	-	$0.88^{+0.50}_{-0.33}$	$-2.73^{+0.13}_{-0.22}$	1 †	-	-	-	-	-
NGC3031	ϵ	$137.63^{+16.70}_{-14.98}$	$0.84^{+0.03}_{-0.03}$	-	-	-	-	-	-	-	-
NGC3034	η	-	-	$1.85^{+0.21}_{-0.40}$	$-0.67^{+0.25}_{-0.45}$	$0.98^{+0.01}_{-0.01}$	-	-	-	-	-
NGC3185	δ	-	-	$50.16^{+85.33}_{-30.27}$	<2.09	$0.99^{+0.01}_{-0.02}$	-	-	-	-	-
NGC3190	δ	-	-	$22.11^{+34.35}_{-10.68}$	<0.54	$0.99^{+0.01}_{-0.01}$	-	-	-	-	-
NGC3516	δ	-	-	$15.12^{+2.41}_{-3.07}$	$1.09^{+0.08}_{-0.63}$	$0.94^{+0.03}_{-0.04}$	-	-	-	-	-
NGC3729	θ	$13.94^{+9.03}_{-4.35}$	$0.96^{+0.01}_{-0.01}$	-	-	-	-	-	-	-	-
NGC4036	ζ	-	-	$34.56^{+13.21}_{-23.99}$	<1.93	$0.99^{+0.01}_{-0.02}$	-	-	-	-	-
NGC4051	μ	-	-	$7.93^{+3.33}_{-1.01}$	$1.48^{+0.50}_{-0.20}$	$0.70^{+4.66}_{-8.54}$	$162.74^{+4.66}_{-8.54}$	$-0.29^{+0.57}_{-0.25}$	$0.99^{+0.01}_{-0.01}$	-	-
NGC4102	ζ	-	-	$22.80^{+2.36}_{-0.45}$	<-1.83	$0.99^{+0.01}_{-0.01}$	-	-	-	-	-
NGC4111	π	$16.40^{+3.34}_{-2.20}$	$0.96^{+0.03}_{-0.09}$	-	-	-	-	-	-	-	-
NGC4125	ζ	-	-	$8.21^{+4.53}_{-5.23}$	$2.52^{+0.28}_{-0.29}$	>0.74	-	-	-	-	-
NGC4151	τ	-	-	$4.04^{+0.03}_{-0.03}$	$-1.05^{+0.01}_{-0.01}$	$0.98^{+0.01}_{-0.01}$	$58.64^{+0.13}_{-0.13}$	$-0.55^{+0.01}_{-0.02}$	$0.98^{+0.01}_{-0.01}$	$0.82^{+0.01}_{-0.01}$	$0.21^{+0.01}_{-0.01}$
NGC4203	μ	-	-	$142.87^{+21.70}_{-8.39}$	$0.27^{+0.13}_{-0.77}$	$0.97^{+0.01}_{-0.01}$	$1.03^{+0.09}_{-0.08}$	>-1.63	$0.74^{+0.03}_{-0.04}$	-	-
NGC4217	ϵ	$5.73^{+3.02}_{-1.71}$	$0.94^{+0.03}_{-0.06}$	-	-	-	-	-	-	-	-
NGC4258	δ	-	-	$92.91^{+11.71}_{-10.18}$	$-0.55^{+0.06}_{-0.24}$	$0.92^{+0.01}_{-0.02}$	-	-	-	-	-
NGC4395	δ	-	-	$8.40^{+0.98}_{-2.45}$	$1.67^{+0.24}_{-0.22}$	$0.98^{+0.01}_{-0.01}$	-	-	-	-	-
NGC5033	δ	-	-	$64.86^{+17.97}_{-2.64}$	$-0.49^{+0.10}_{-0.14}$	$0.92^{+0.03}_{-0.01}$	-	-	-	-	-
NGC5273	δ	-	-	$12.84^{+9.14}_{-4.85}$	$1.15^{+0.75}_{-1.43}$	$0.95^{+0.03}_{-0.06}$	-	-	-	-	-
NGC5548	λ	-	-	$8.34^{+0.26}_{-0.66}$	$2.10^{+0.06}_{-0.04}$	$0.67^{+0.03}_{-0.05}$	$156.68^{+2.98}_{-3.59}$	$-0.54^{+0.03}_{-0.05}$	$0.99^{+0.01}_{-0.01}$	-	-
NGC5866	ϵ	$7.13^{+0.89}_{-0.75}$	$0.95^{+0.05}_{-0.04}$	-	-	-	-	-	-	-	-
NGC5879	δ	-	-	$17.98^{+3.10}_{-6.70}$	$0.80^{+0.34}_{-0.50}$	$0.99^{+0.01}_{-0.01}$	-	-	-	-	-

Table 13: Additional spectral parameters for NGC 5194. Note that where the †symbol is used, this denotes the parameter was frozen before fitting. The errors shown in this table are all at the 1σ level. The CABS parameter was set equal to the ZTBABS parameter in Table 10. In addition, we used a CUTOFFPL model instead of a powerlaw (see text). The PEXRAV model parameters were set to those of other parameters e.g. the photon index and normalisations, or frozen.

		CABS	CUTOFFPL			PEXRAV						
Name	mod.	$N_{\rm H}$	Phot.I.	HighECut (keV)	norm.	Phot.I.	foldE(keV)	relrefl	abund	Fe abund	cosIncl	norm.
(1)	(2)	(3)	(4)	(5)	(6)	(7)	(8)	(9)	(10)	(11)	(12)	
NGC5194	τ	$6601.11^{+3479.39}_{-2252.91}$	1.8 †	300 †	$6.57^{2.91}_{4.32}\times10^{-5}$	1.8 †	300 †	-1 †	1.0 †	1.0 †	0.45 †	$6.57^{2.91}_{4.32}\times10^{-5}$

We plot all of the 150 detected sources in the following images. In all plots, the source is labelled at the top of the image. The *top panel* in each plot shows the number of photons cm^{-2} s^{-1} keV^{-1} plotted against the energy in keV across the whole 0.3–10.0 keV band. The *bottom panel* in each plot shows the model subtracted from the data, divided by the error. The fit parameters to make these plots are shown in this Online Supplementary Material Tables.

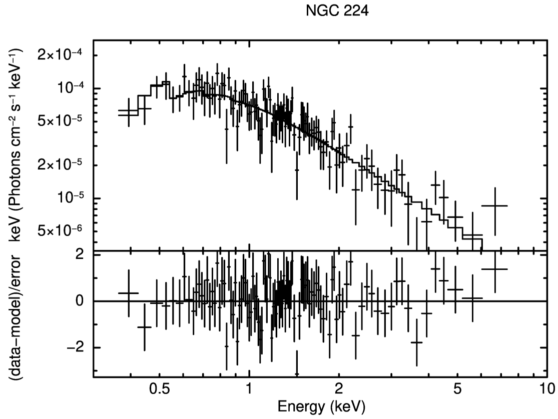

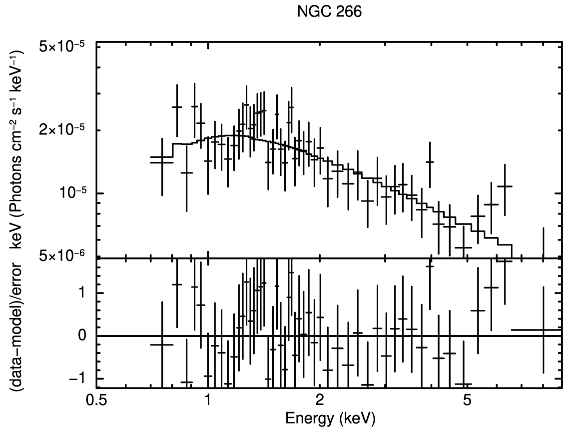

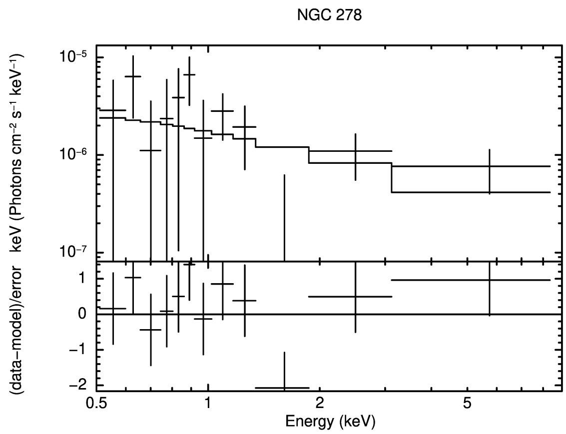

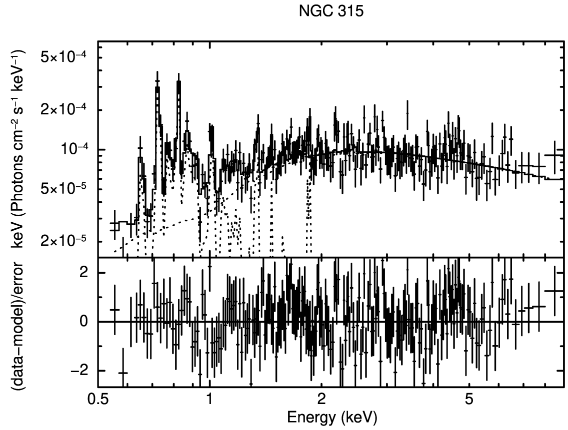

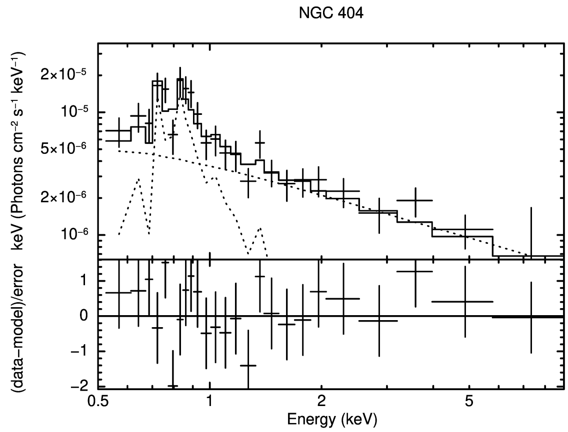

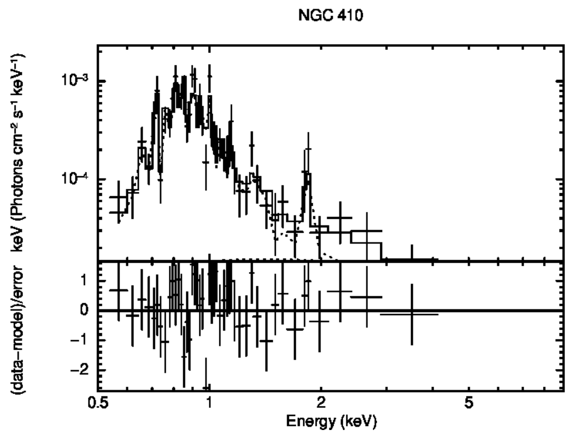

7.1 X-ray Spectra

We plot all of the 150 detected sources in the following images. In all plots, the source is labelled at the top of the image. The *top panel* in each plot shows the number of photons cm^{-2} s^{-1} keV^{-1} plotted against the energy in keV across the whole 0.3–10.0 keV band. The *bottom panel* in each plot shows the model subtracted from the data, divided by the error. The fit parameters to make these plots are shown in this Appendix.

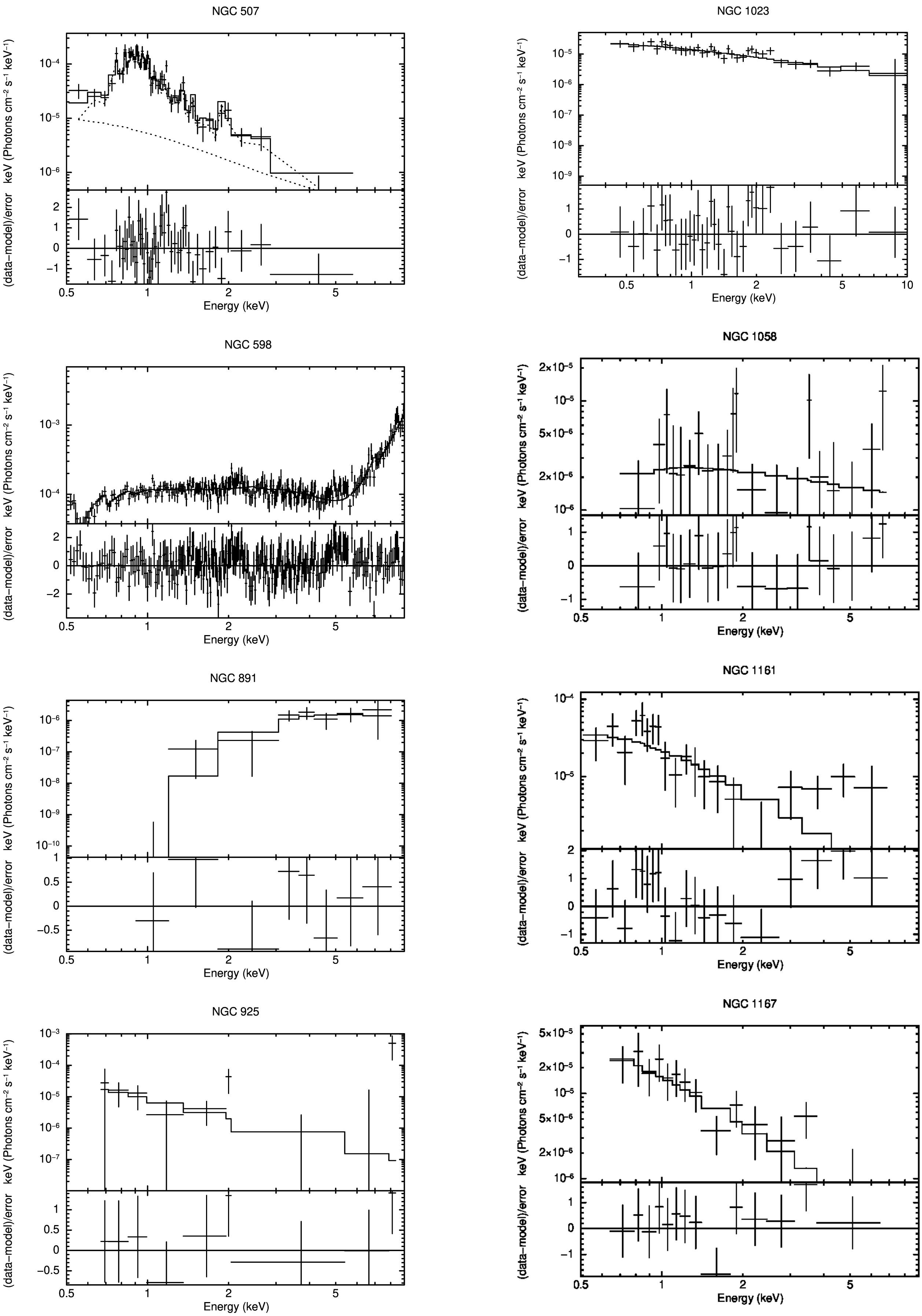
NGC 507
NGC 1023
NGC 598
NGC 1058
NGC 891
NGC 1161
NGC 925
NGC 1167
keV (Photons cm^{-2} s^{-1} keV^{-1})
(data−model)/error
Energy (keV)

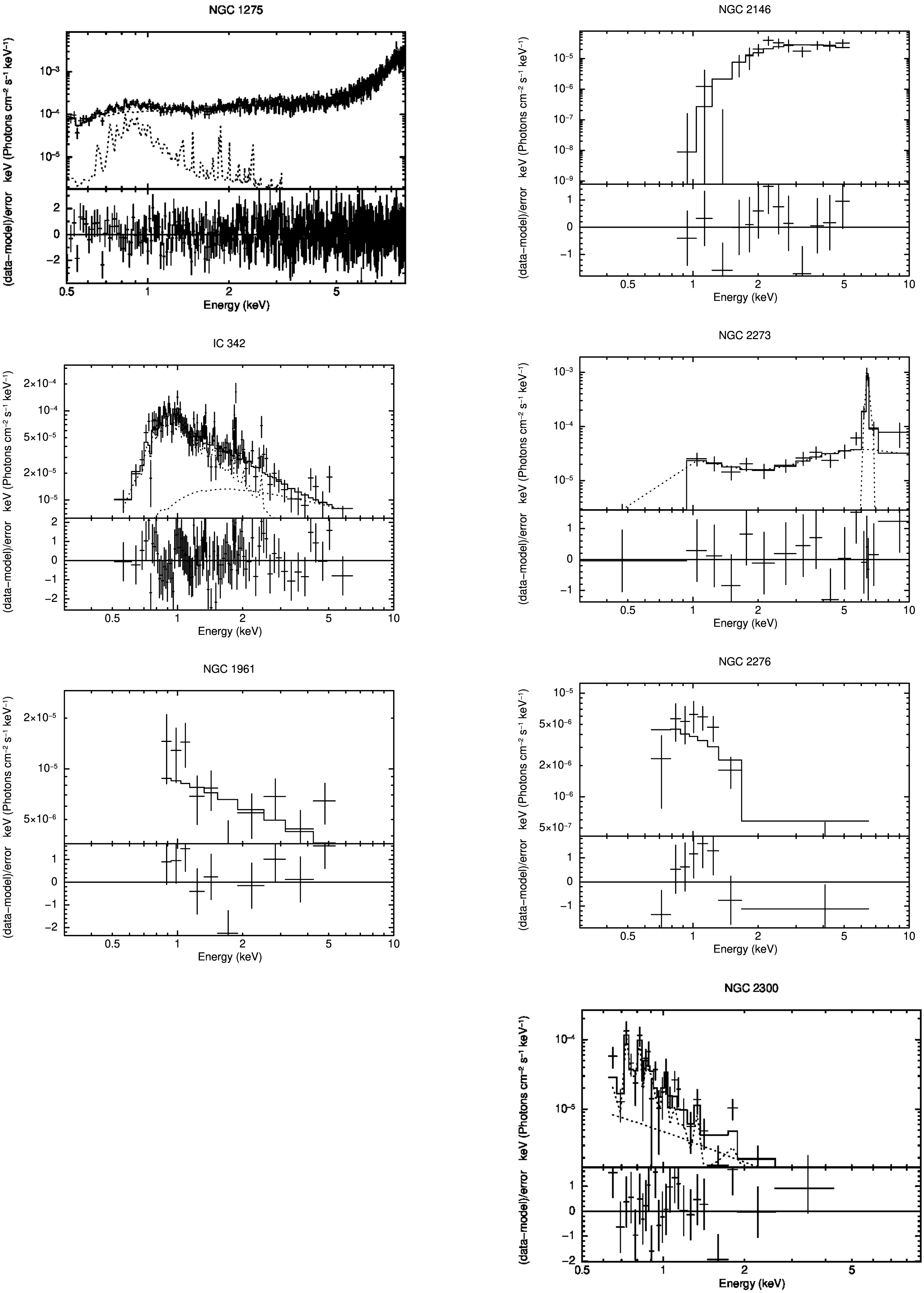
NGC 1275
IC 342
NGC 1961
NGC 2146
NGC 2273
NGC 2276
NGC 2300
keV (Photons cm⁻² s⁻¹ keV⁻¹)
(data−model)/error
Energy (keV)

NGC 2403

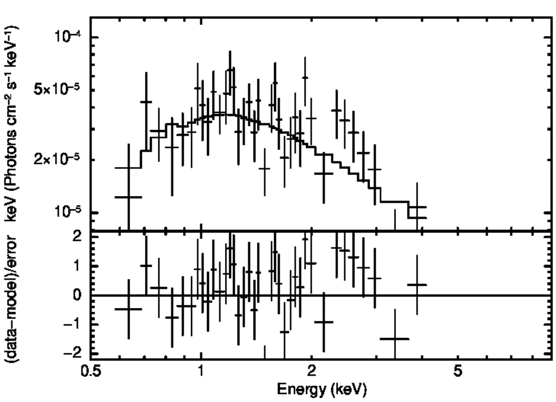

NGC 2639

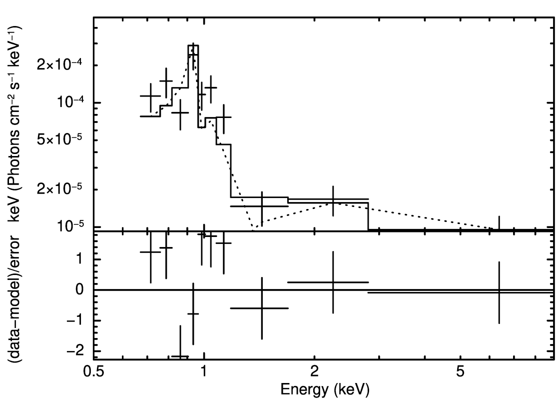

NGC 2500

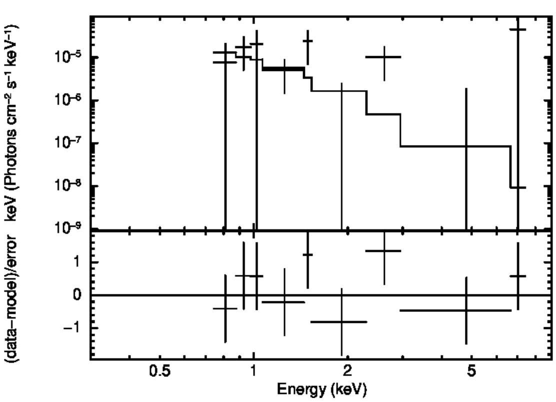

NGC 2683

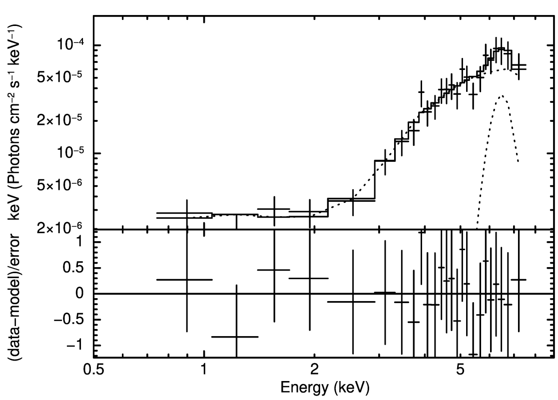

NGC 2541

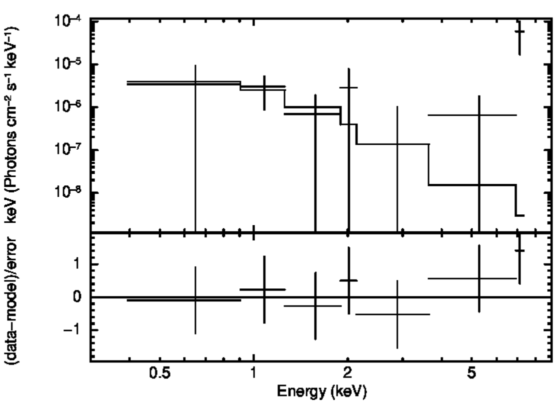

NGC 2681

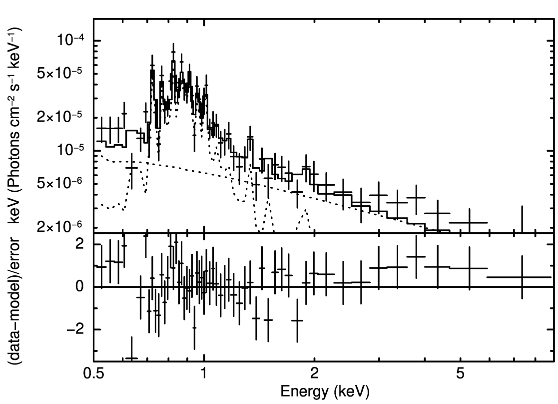

NGC 2549

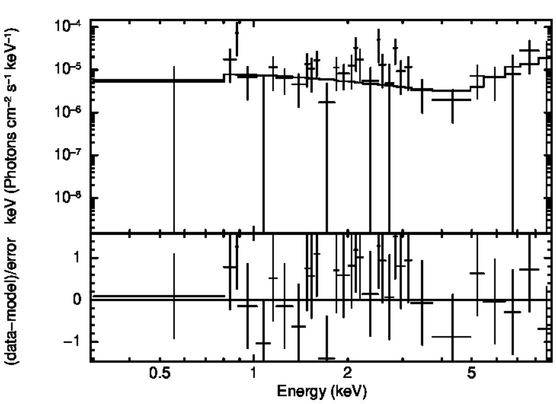

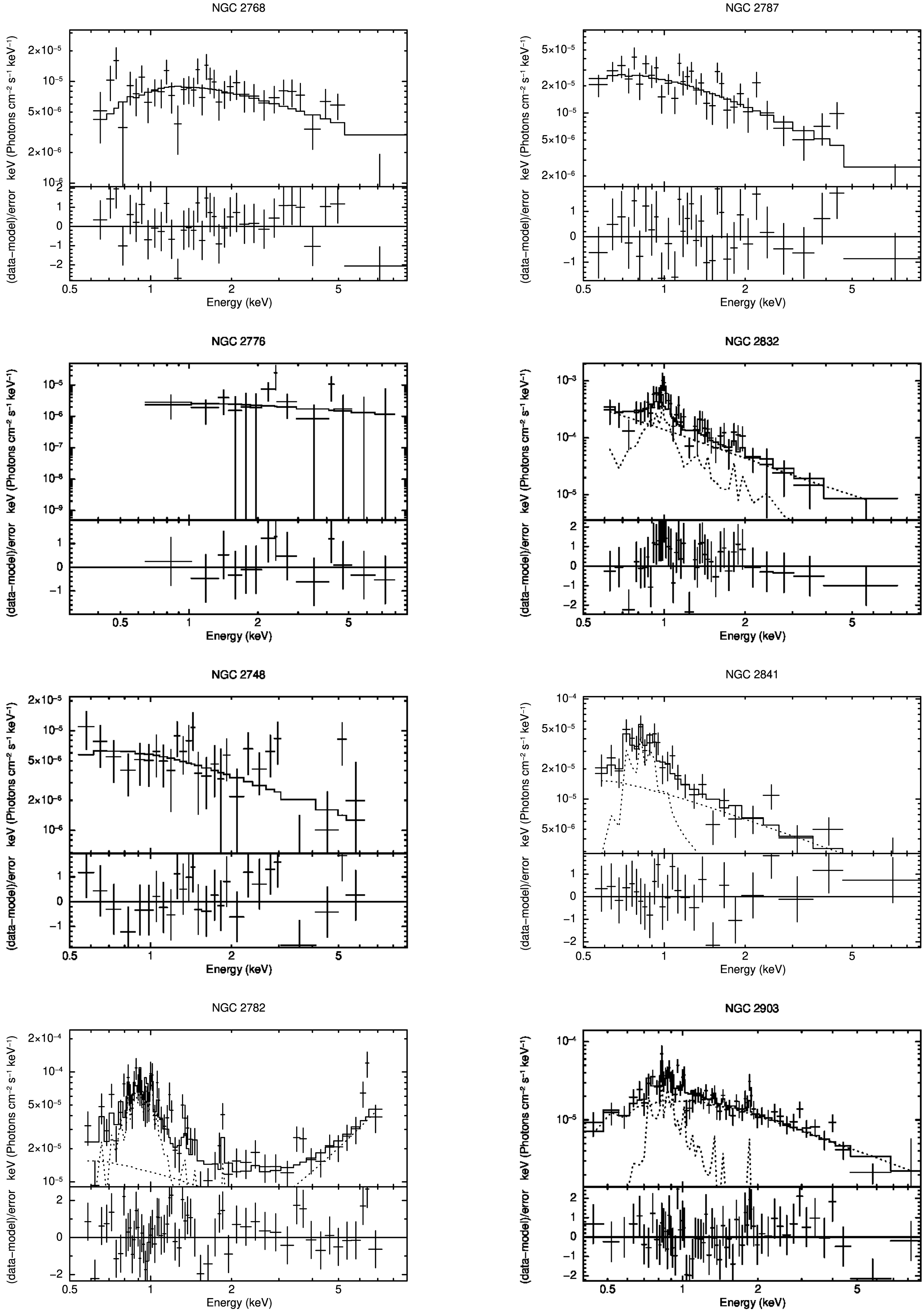
NGC 2768
NGC 2787
NGC 2776
NGC 2832
NGC 2748
NGC 2841
NGC 2782
NGC 2903
keV (Photons cm⁻² s⁻¹ keV⁻¹)
(data−model)/error
Energy (keV)

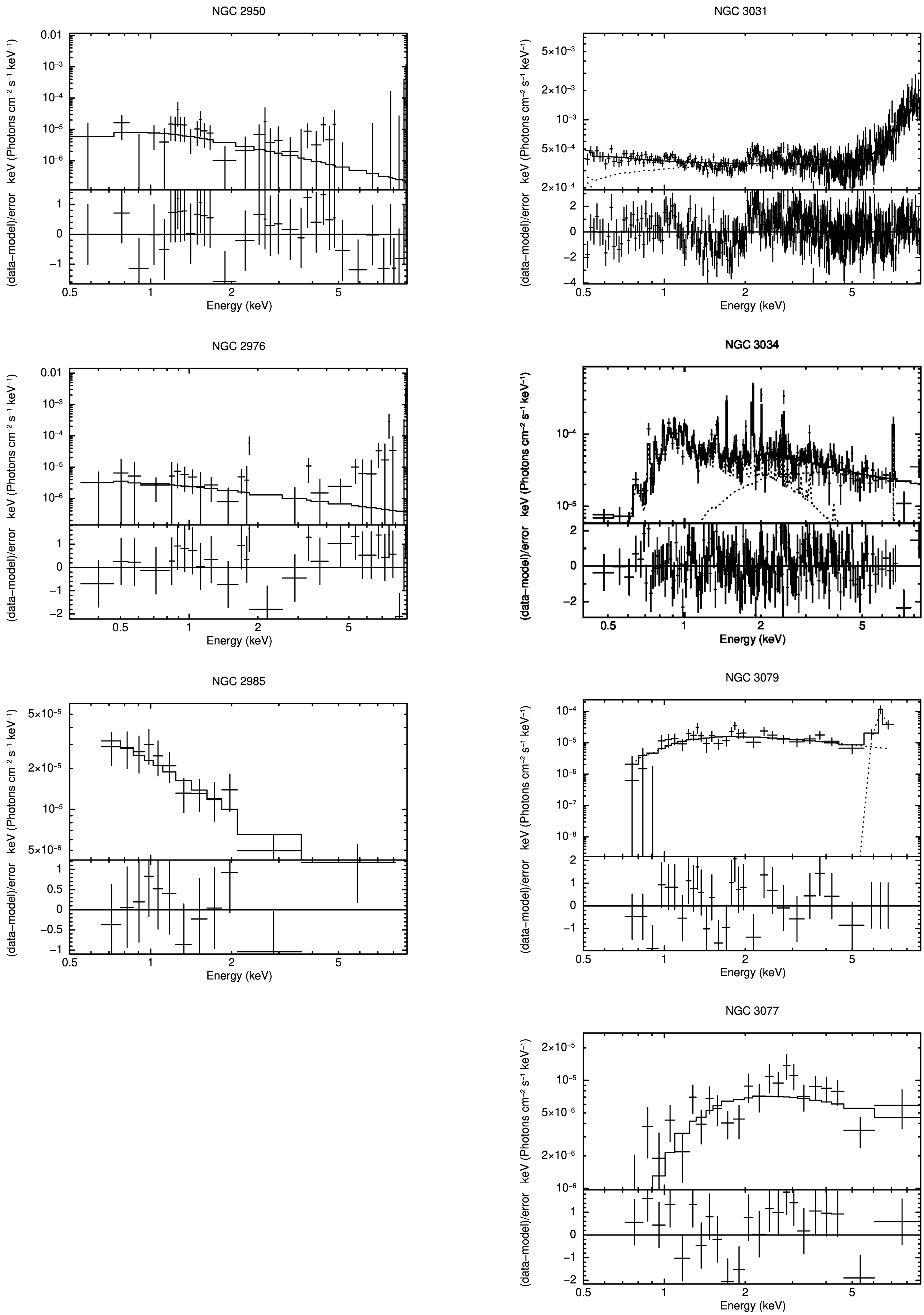
NGC 2950
NGC 3031
NGC 2976
NGC 3034
NGC 2985
NGC 3079
NGC 3077
keV (Photons cm⁻² s⁻¹ keV⁻¹)
(data−model)/error
Energy (keV)

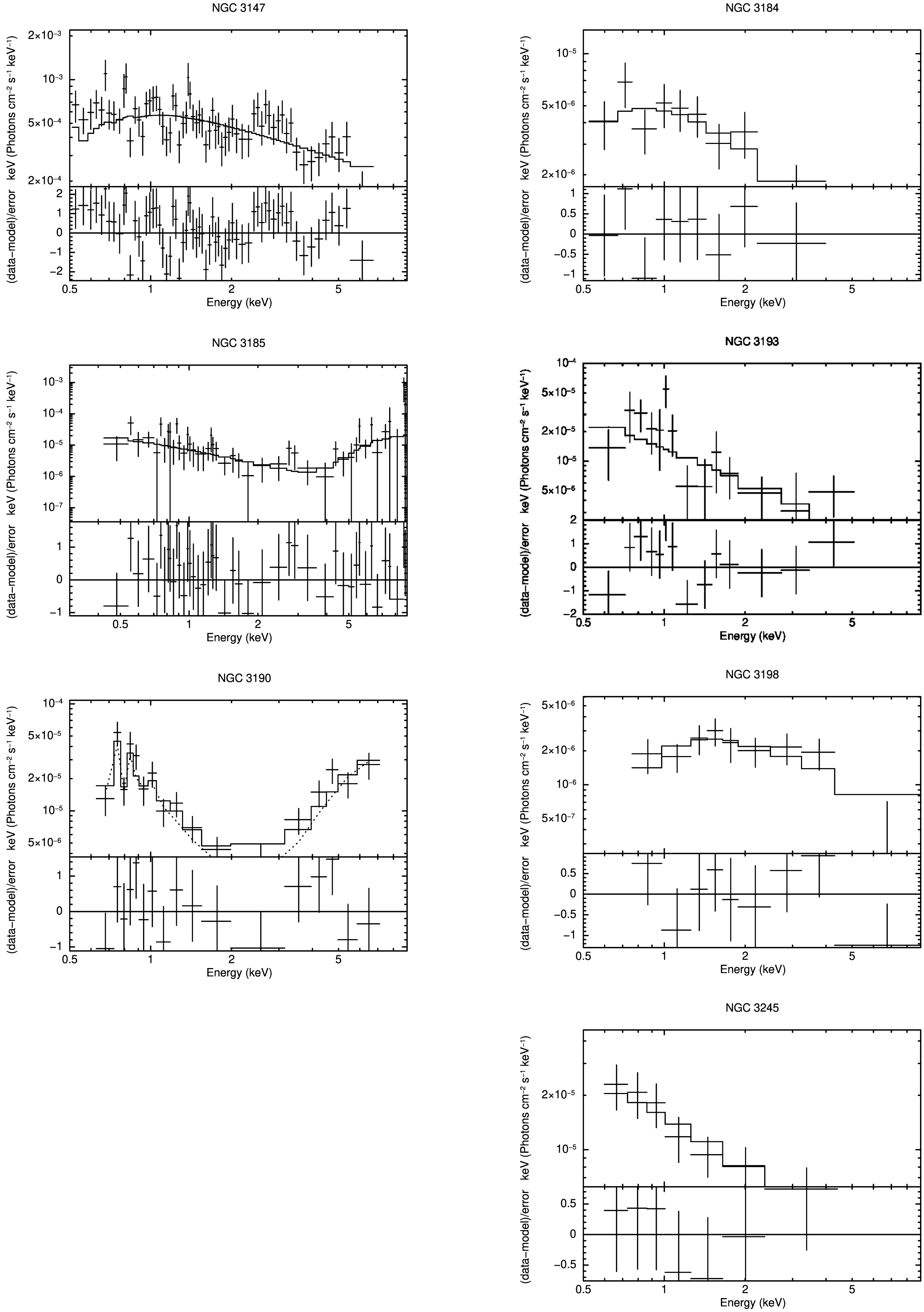
NGC 3147
NGC 3184
NGC 3185
NGC 3193
NGC 3190
NGC 3198
NGC 3245
keV (Photons cm⁻² s⁻¹ keV⁻¹)
(data−model)/error
Energy (keV)

NGC 3310

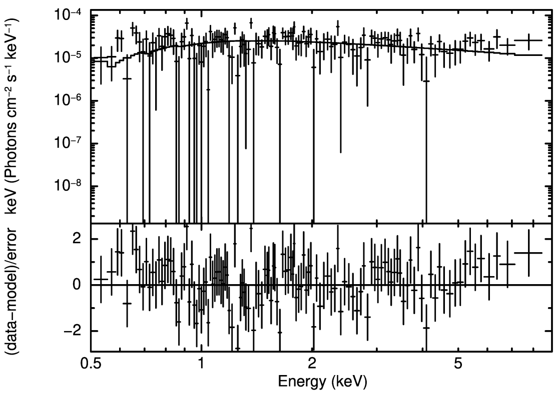

NGC 3414

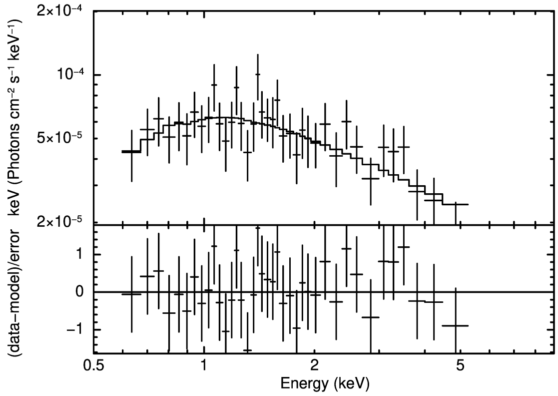

NGC 3319

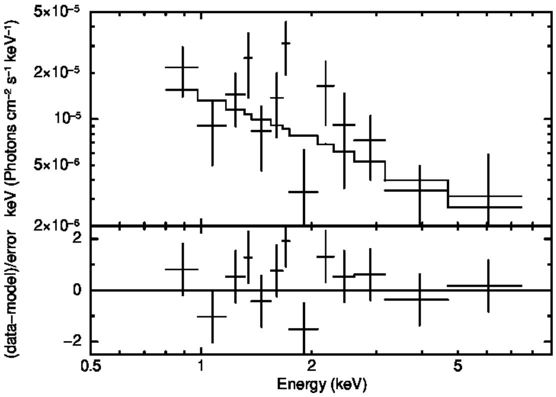

NGC 3448

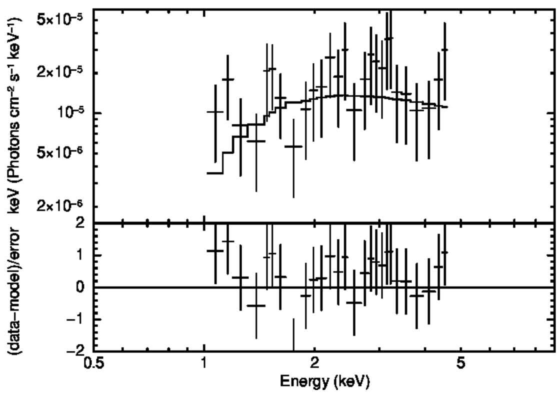

NGC 3344

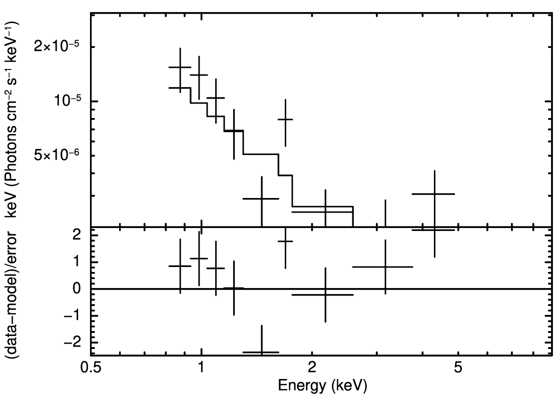

NGC 3516

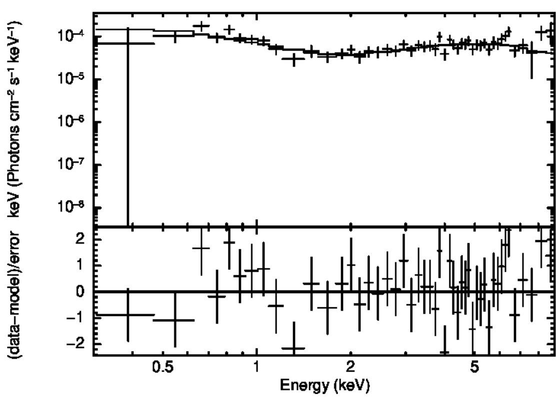

NGC 3395

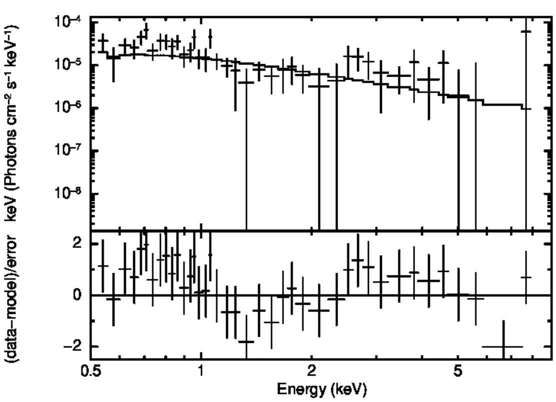

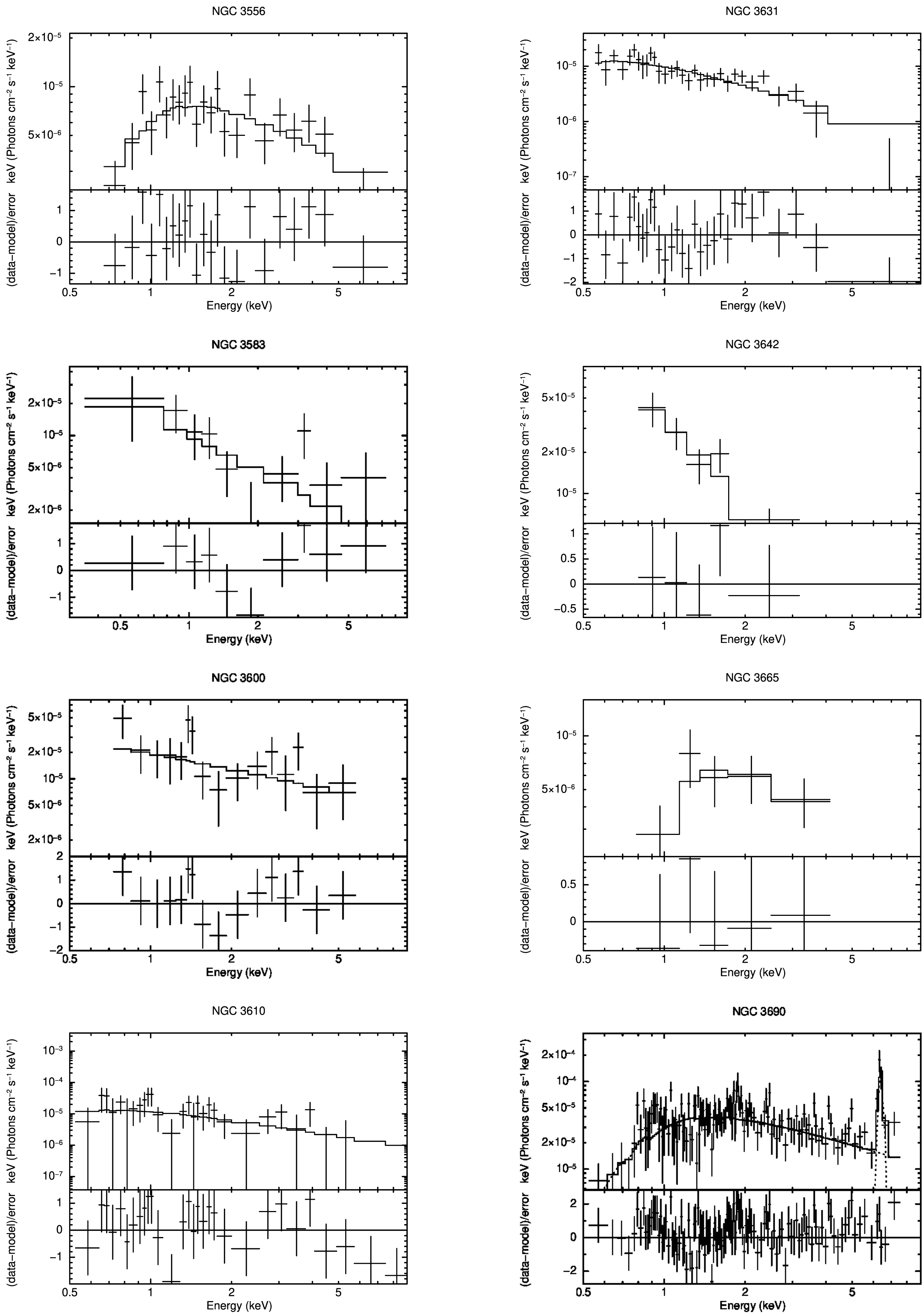
NGC 3556
NGC 3631
NGC 3583
NGC 3642
NGC 3600
NGC 3665
NGC 3610
NGC 3690
keV (Photons cm⁻² s⁻¹ keV⁻¹)
(data−model)/error
Energy (keV)

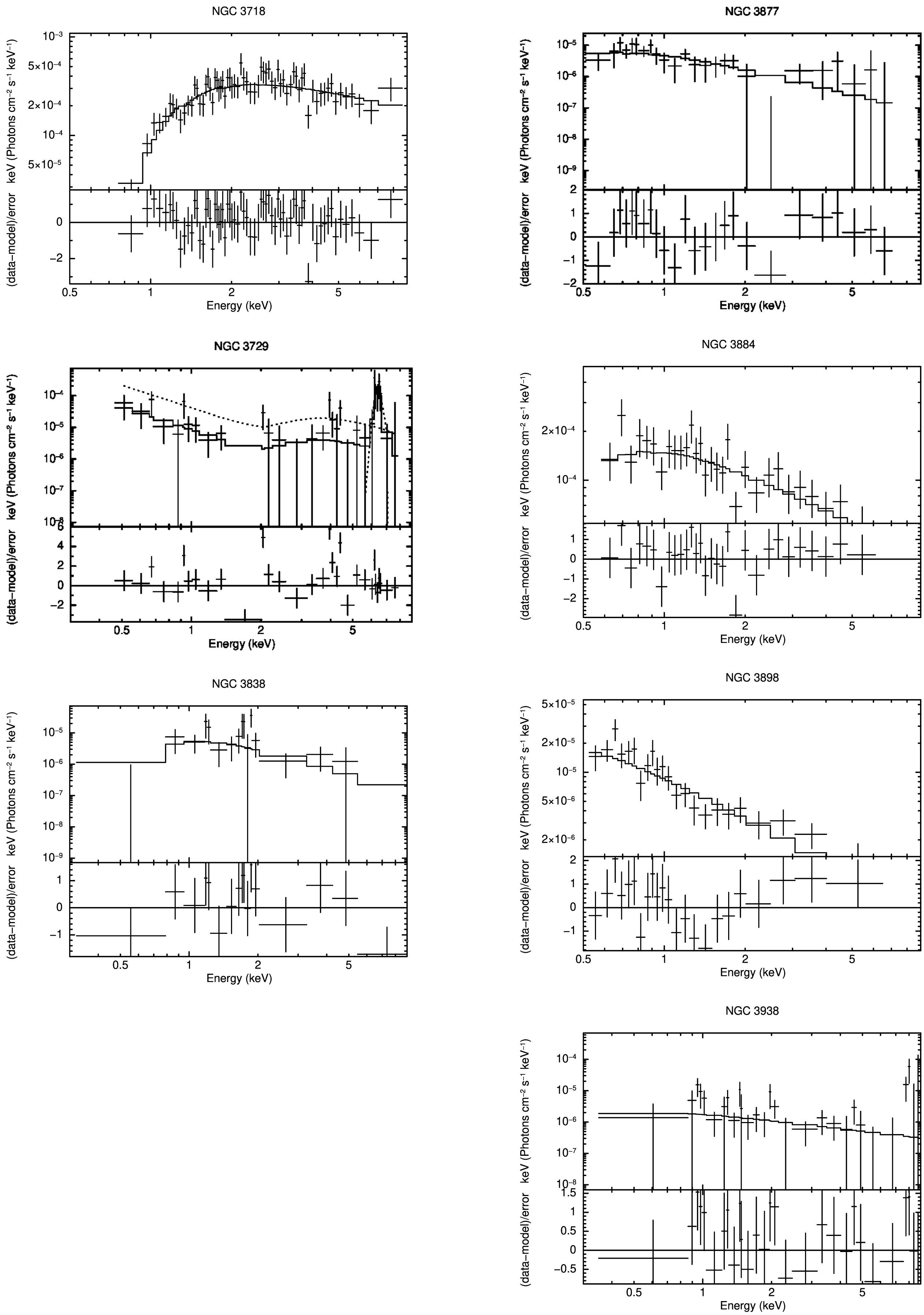
NGC 3718
NGC 3877
NGC 3729
NGC 3884
NGC 3838
NGC 3898
NGC 3938
keV (Photons cm⁻² s⁻¹ keV⁻¹)
(data−model)/error
Energy (keV)

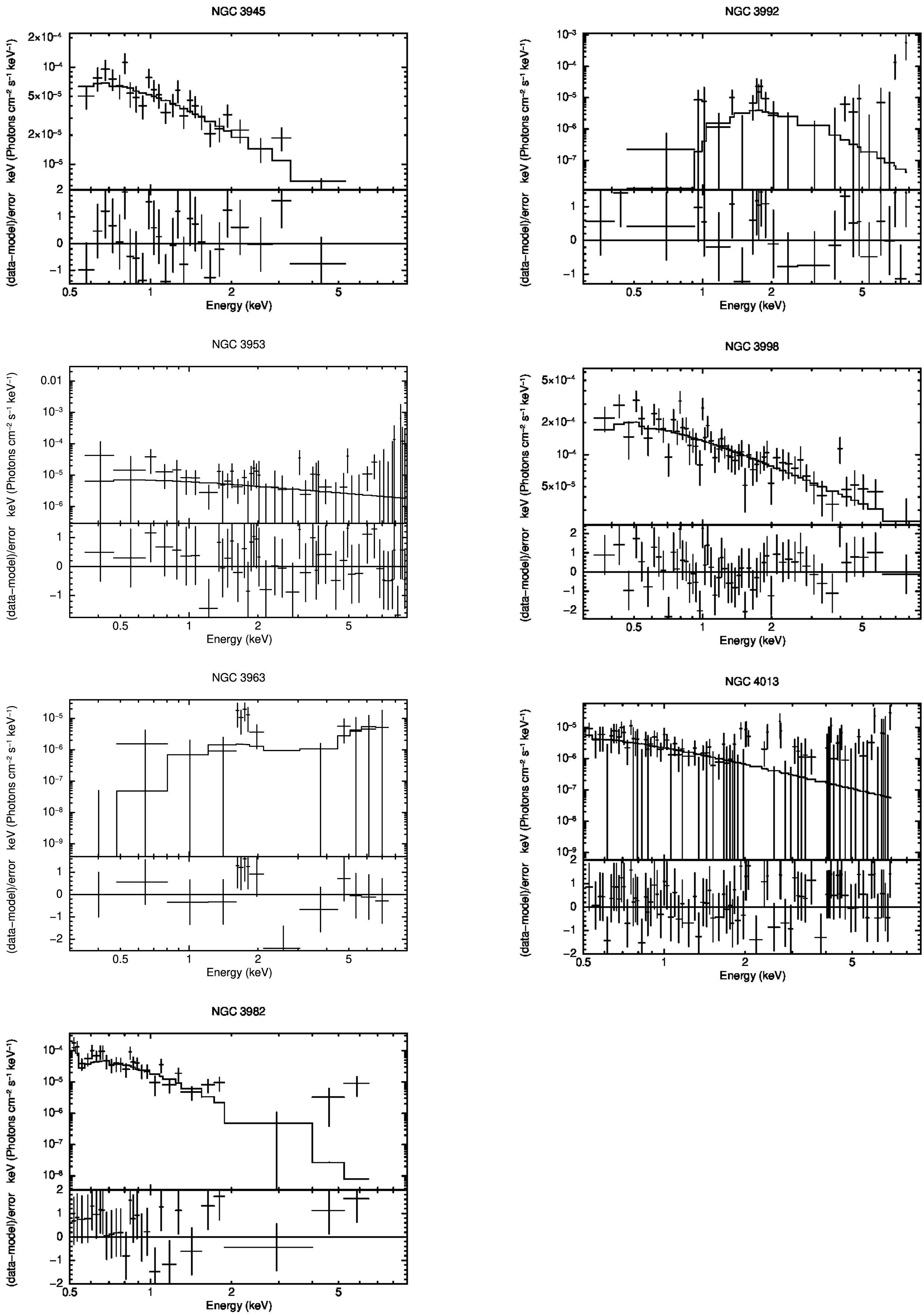
NGC 3945
NGC 3992
NGC 3953
NGC 3998
NGC 3963
NGC 4013
NGC 3982
keV (Photons cm^{-2} s^{-1} keV^{-1})
(data−model)/error
Energy (keV)

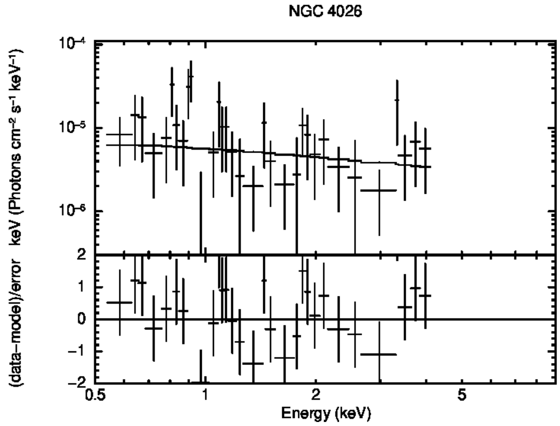
NGC 4026
keV (Photons cm⁻² s⁻¹ keV⁻¹)
(data−model)/error
Energy (keV)

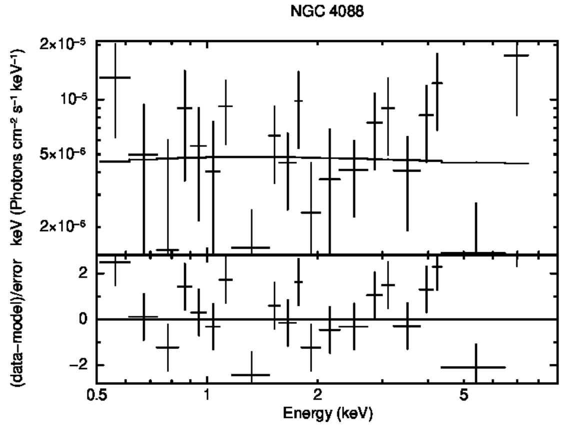
NGC 4088
keV (Photons cm⁻² s⁻¹ keV⁻¹)
(data−model)/error
Energy (keV)

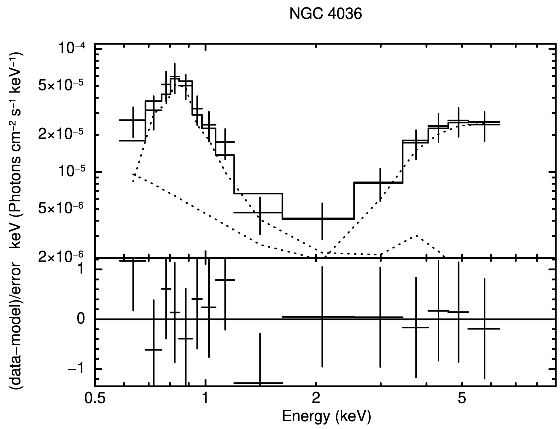
NGC 4036
keV (Photons cm⁻² s⁻¹ keV⁻¹)
(data−model)/error
Energy (keV)

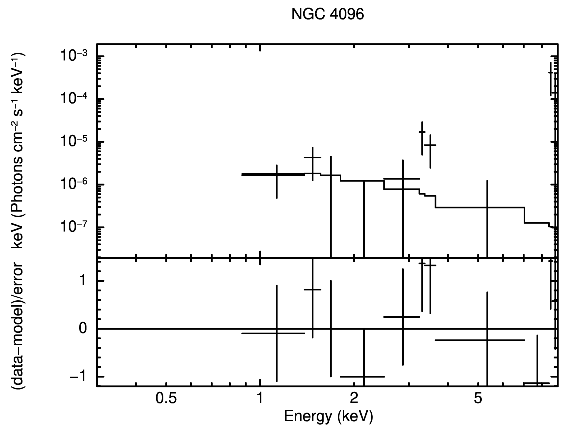
NGC 4096
keV (Photons cm⁻² s⁻¹ keV⁻¹)
(data−model)/error
Energy (keV)

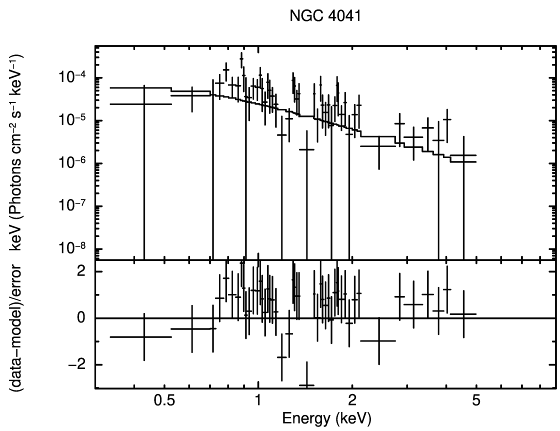
NGC 4041
keV (Photons cm⁻² s⁻¹ keV⁻¹)
(data−model)/error
Energy (keV)

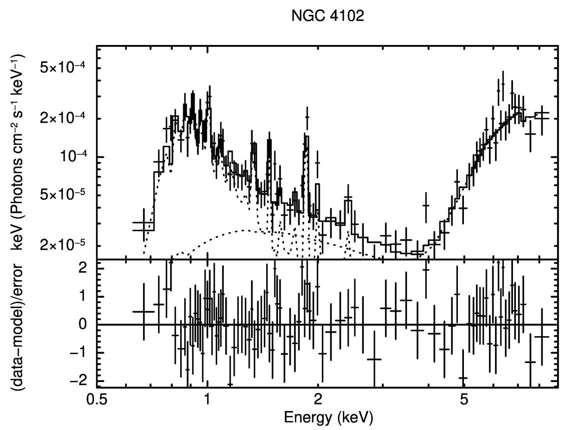
NGC 4102
keV (Photons cm⁻² s⁻¹ keV⁻¹)
(data−model)/error
Energy (keV)

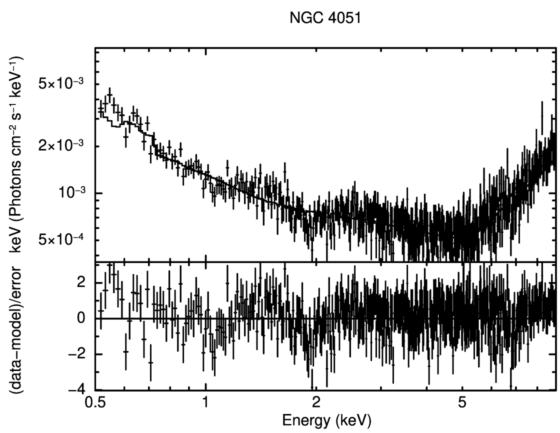
NGC 4051
keV (Photons cm⁻² s⁻¹ keV⁻¹)
(data−model)/error
Energy (keV)

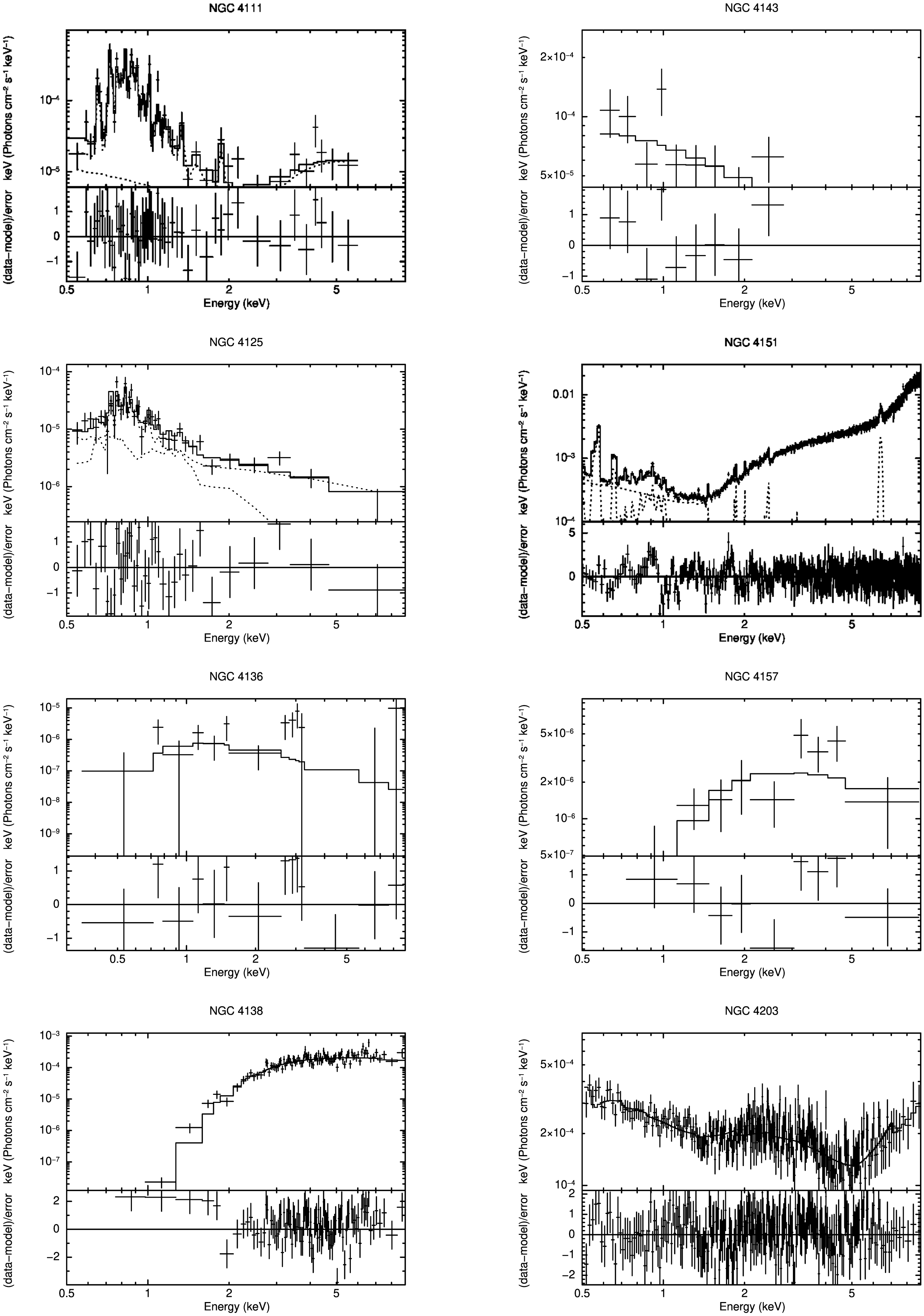
NGC 4111
NGC 4143
NGC 4125
NGC 4151
NGC 4136
NGC 4157
NGC 4138
NGC 4203
keV (Photons cm⁻² s⁻¹ keV⁻¹)
(data−model)/error
Energy (keV)

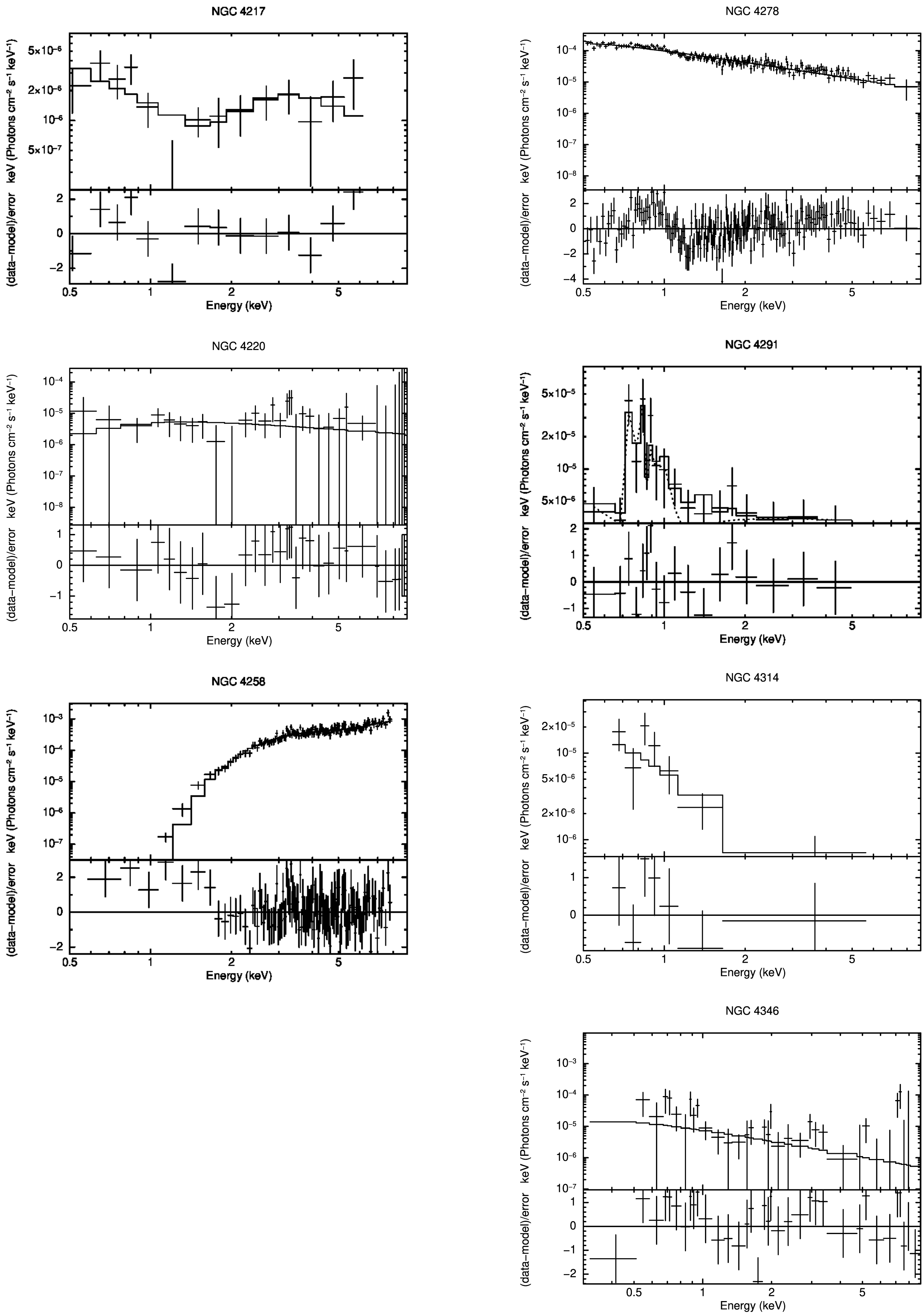
NGC 4217
NGC 4278
NGC 4220
NGC 4291
NGC 4258
NGC 4314
NGC 4346
keV (Photons cm^{-2} s^{-1} keV^{-1})
(data−model)/error
Energy (keV)

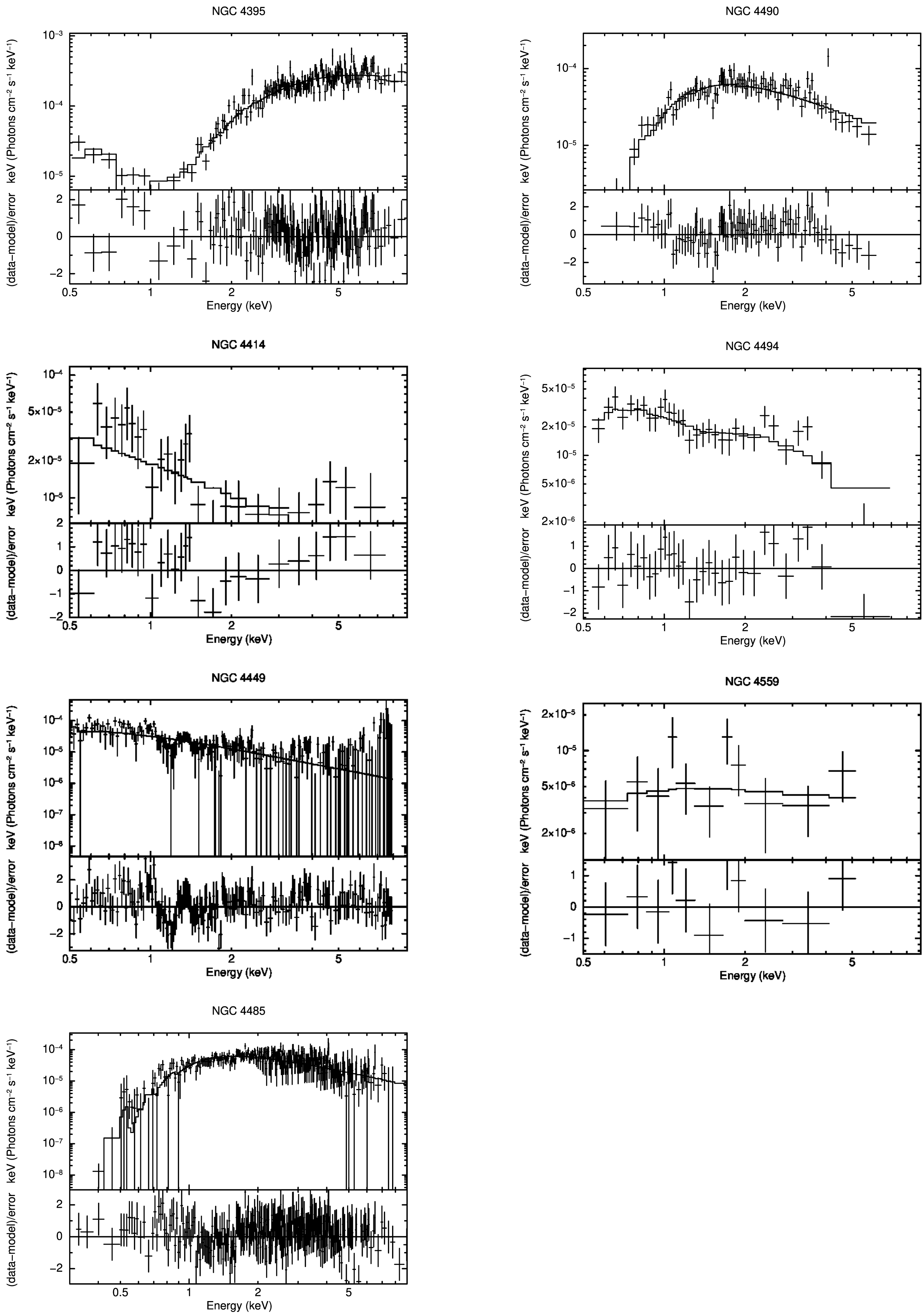
NGC 4395
NGC 4490
NGC 4414
NGC 4494
NGC 4449
NGC 4559
NGC 4485
keV (Photons cm⁻² s⁻¹ keV⁻¹)
(data−model)/error
Energy (keV)

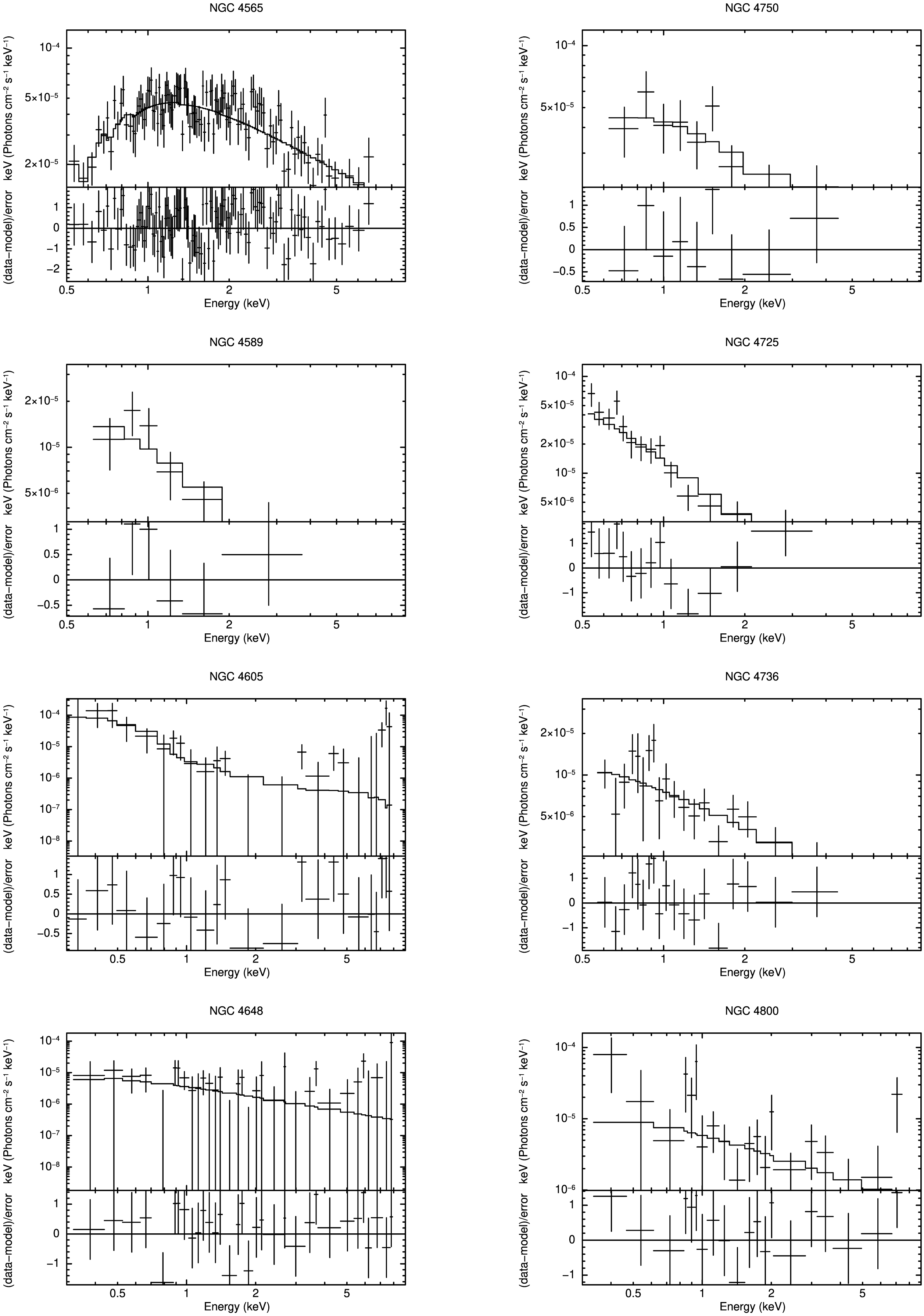
NGC 4565
NGC 4750
NGC 4589
NGC 4725
NGC 4605
NGC 4736
NGC 4648
NGC 4800
keV (Photons cm⁻² s⁻¹ keV⁻¹)
(data−model)/error
Energy (keV)

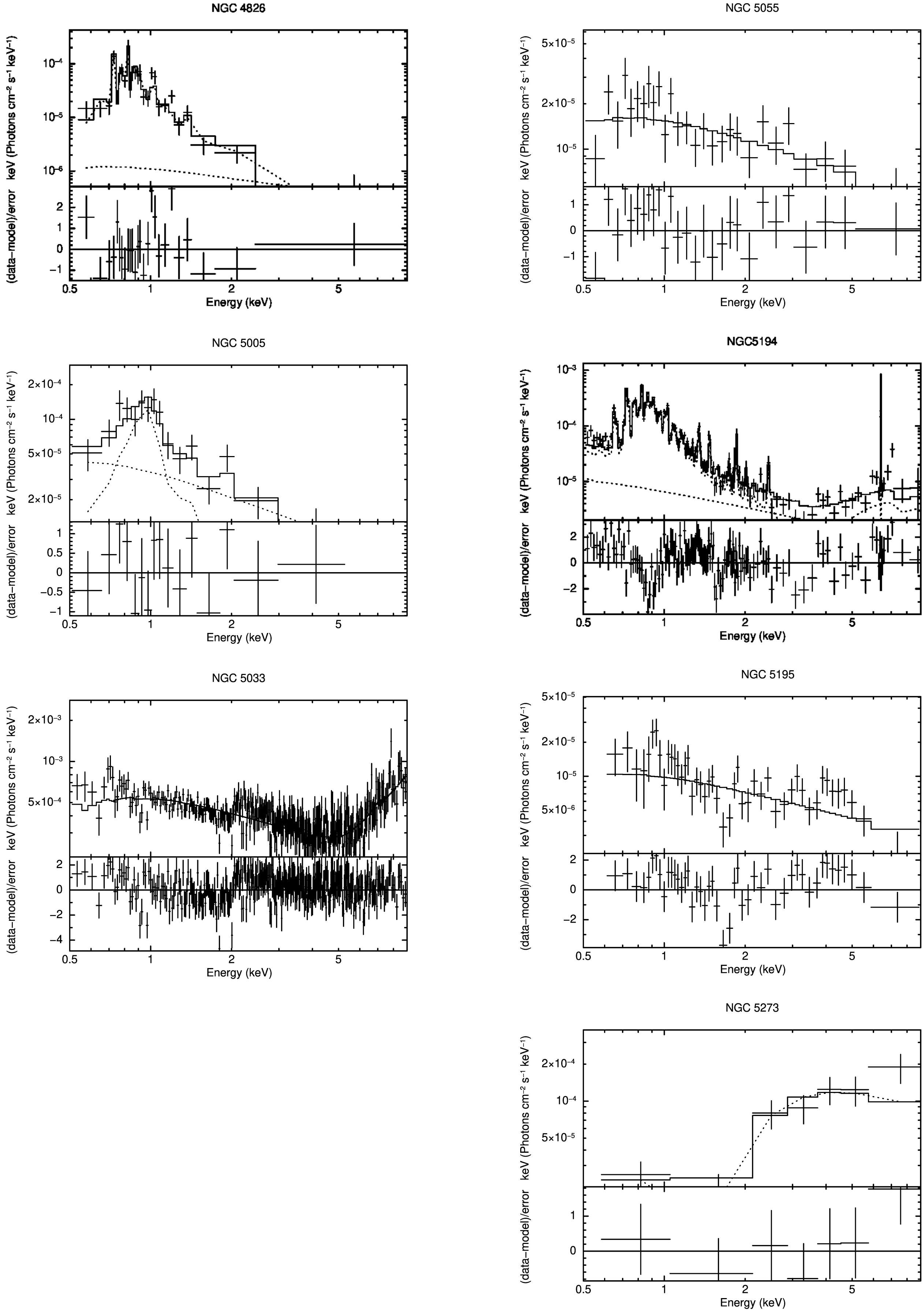
NGC 4826
NGC 5055
NGC 5005
NGC5194
NGC 5033
NGC 5195
NGC 5273
keV (Photons cm⁻² s⁻¹ keV⁻¹)
(data−model)/error
Energy (keV)

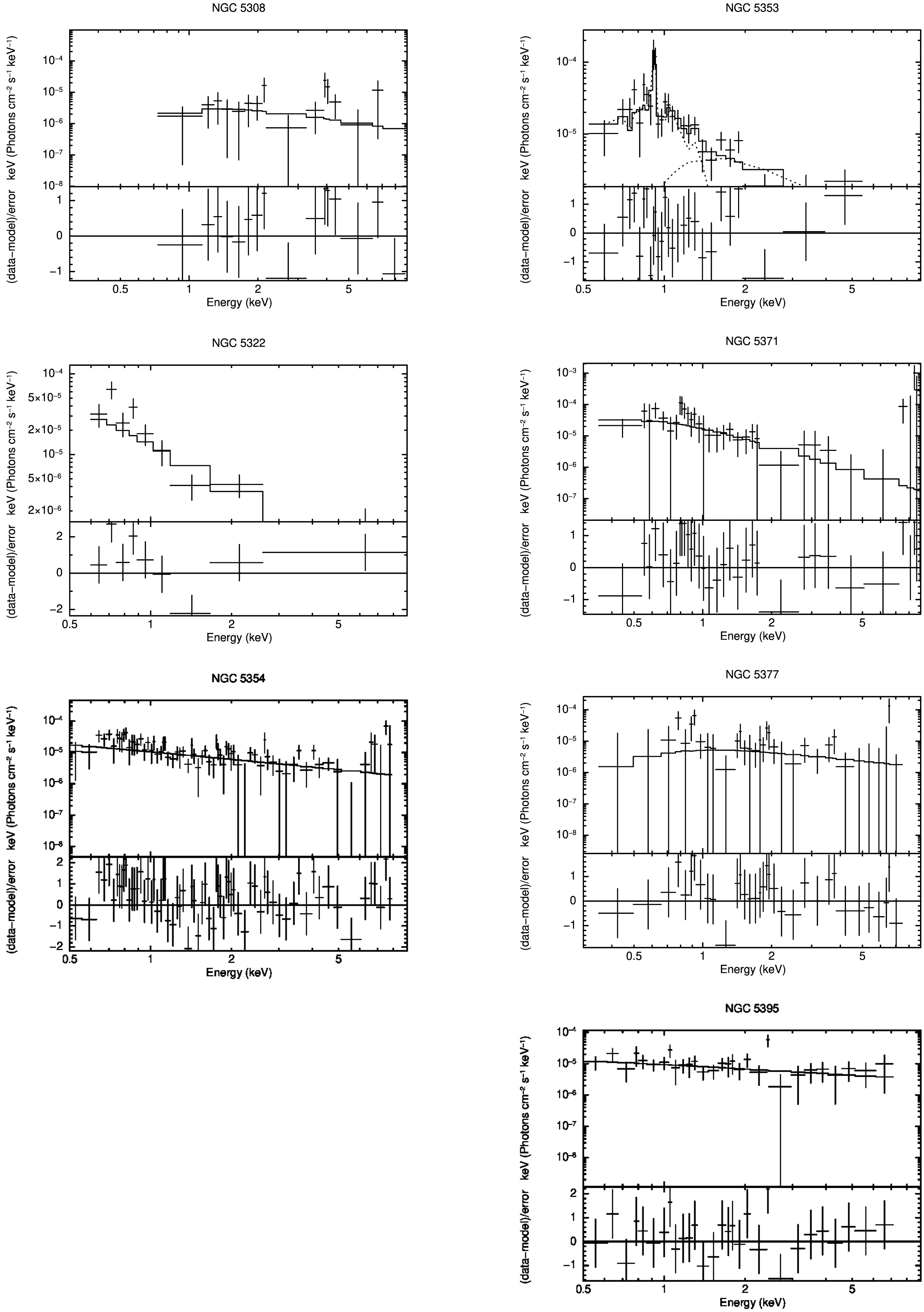
NGC 5308
NGC 5353
NGC 5322
NGC 5371
NGC 5354
NGC 5377
NGC 5395
keV (Photons cm⁻² s⁻¹ keV⁻¹)
(data−model)/error
Energy (keV)

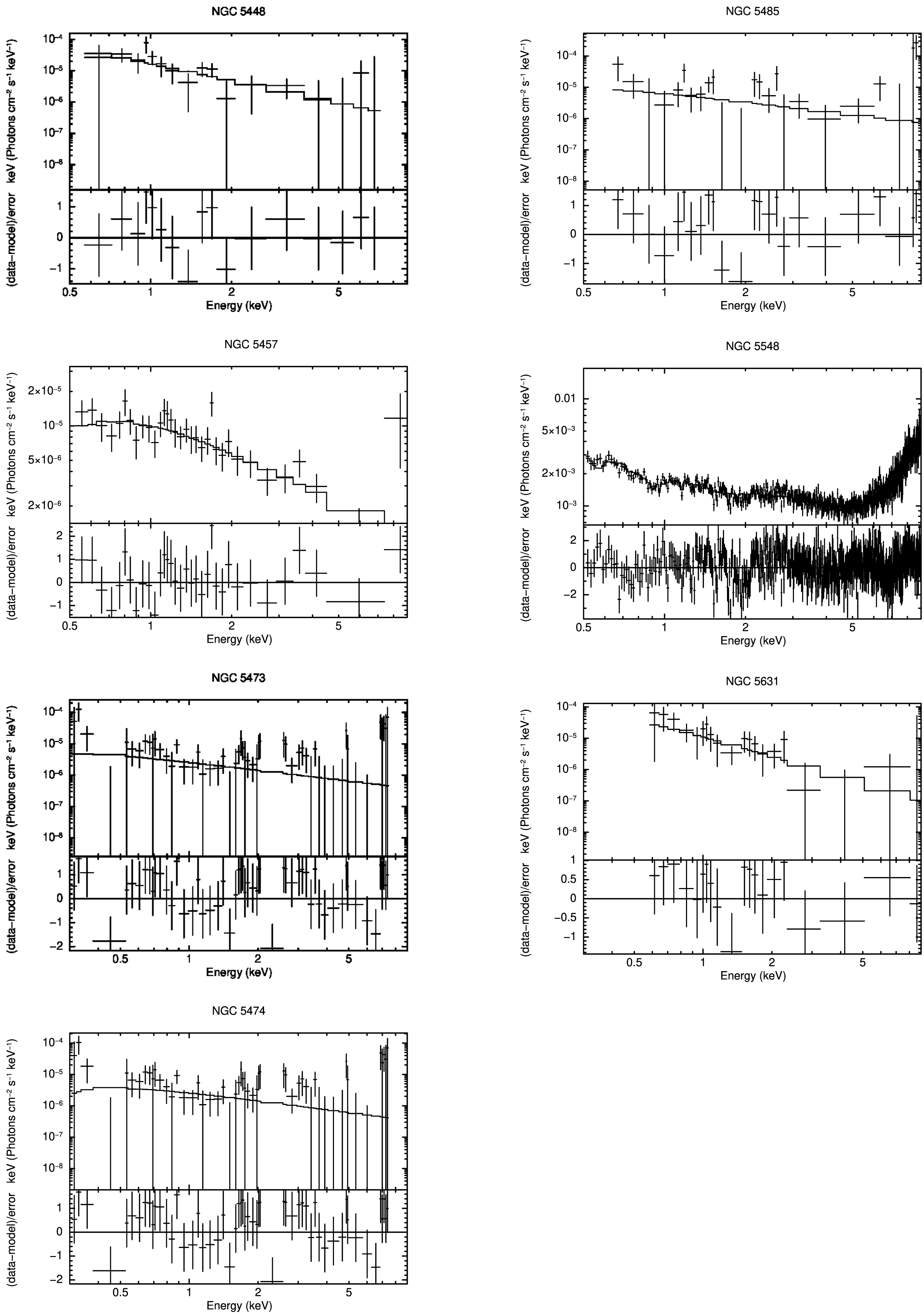
NGC 5448
NGC 5485
NGC 5457
NGC 5548
NGC 5473
NGC 5631
NGC 5474
keV (Photons cm⁻² s⁻¹ keV⁻¹)
(data−model)/error
Energy (keV)

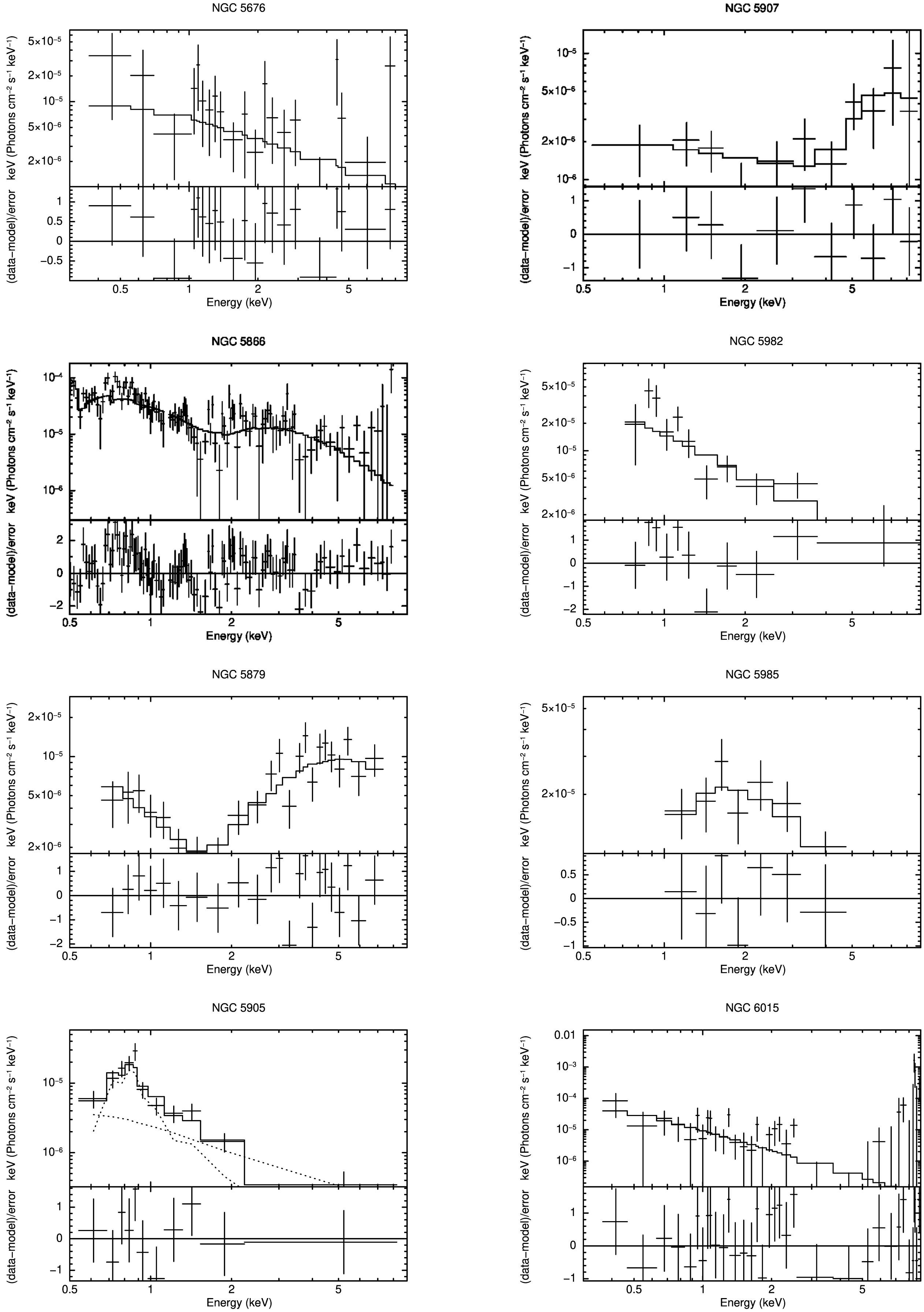
NGC 5676
NGC 5907
NGC 5866
NGC 5982
NGC 5879
NGC 5985
NGC 5905
NGC 6015
keV (Photons cm⁻² s⁻¹ keV⁻¹)
(data−model)/error
Energy (keV)

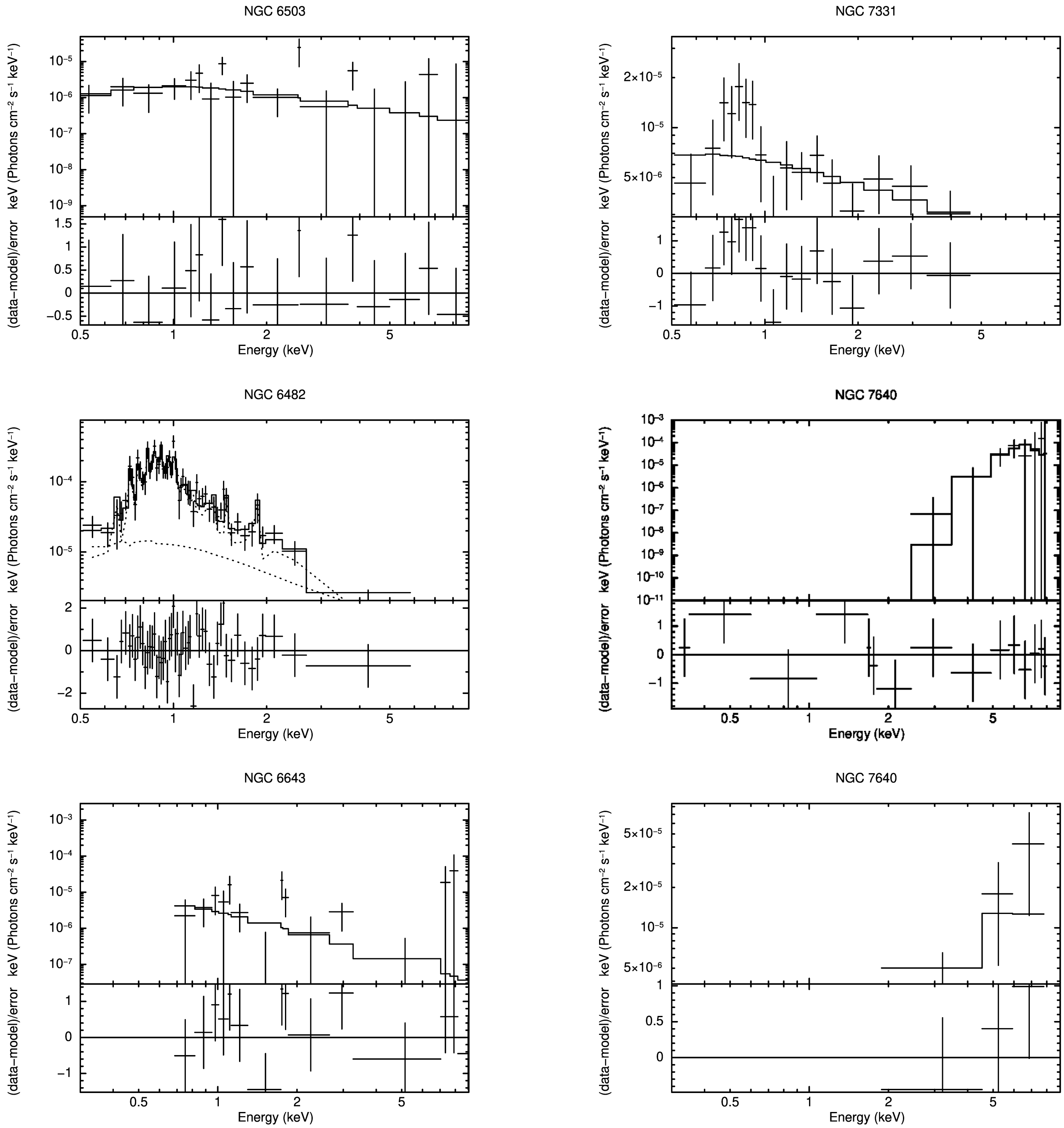

This paper has been typeset from a TEX/LATEX file prepared by the author.